Efficient Antennas for Terahertz and Optical Frequencies

by

Sangjo Choi

A dissertation submitted in partial fulfillment
of the requirements for the degree of
Doctor of Philosophy
(Electrical Engineering)
in the University of Michigan
2014

Doctoral Committee:

Professor Kamal Sarabandi, Chair
Professor Anthony Grbic
Professor Amir Mortazawi
Assistant Professor Thomas Schwarz

To God
To my father Siyoung Choi, and my mother Jaenam Jeon
To my fiancé Saebom Jung

ACKNOWLEDGEMENTS

First and foremost, I would like to deeply thank and dedicate all my success to God, my parents, sister, and fiancé. Without their love and care, I would not be able to accomplish my ph.D work.

I want to express my sincere gratitude and appreciation to my advisors Prof. Kamal Sarabandi for his continuous support, encouragement and guidance throughout my studies. I would like to extend my sincere gratitude to my other committee members, Prof. Amir Mortazawi, Prof. Anthony Grbic and Prof. Thomas Schwarz for devoting their time to review this thesis and advising me with valuable suggestions.

I would like to thank my colleagues and friends at the Radiation Laboratory and EECS for constructive and insightful discussions. I thank Dr. Adib Nashashibi, Dr. Leland Pierce, Dr. Juseop Lee, Dr. Jungsuek Oh, Dr. Young Jun Song, Dr. Victor Lee, Dr. Adel Elsherbini, Dr. DaHan Liao, Dr. Fikadu Dagefu, Dr. Meysam Moallem, Gurkan Gok, Jihun Choi, Michael Benson, Jiangfeng Wu, Abdulkadir Yucel, Hamid Nejatie, Kyunghoon Lee, Kyusang Lee, Seungku Lee, Taehee Jang, and Hyeongseok Kim.

Finally, I would like to thank Pastor. Sun Myung Lyu and my friends at Korean Presbyterian Church of Ann Arbor.

Sangjo
Winter, 2014,
Ann Arbor.

TABLE OF CONTENTS

LIST OF FIGURES

Chapter 1

Introduction

1.1 Background

The crowded wireless communication bands in the gigahertz (GHz) frequency range and the ever-increasing demand for more bandwidth has motivated the exploitation of the unexplored spectrum of electromagnetic waves such as the terahertz (THz) band. The higher bandwidth of the THz band has a potential to achieve an extremely high data rate, such as 1 terabit-per-second, for future wireless devices [1]. The THz band corresponds to the segment of the electromagnetic spectrum from 0.3 THz to 3 THz (corresponding to wavelengths in the range of 0.1 mm ~ 1 mm) in between the millimeter and far-infra (IR) waves [2]. Due to the lack of THz sources and detectors, the THz band has not been thoroughly explored for communications [3]. Until now, low bandwidth up- and down-converters as well as low gain amplifiers in the lower part of the THz band have limited the output power level and bandwidth of THz communication systems. THz sources are also hard to find. Current technology relies on mixing optical sources such as lasers to generate low to moderate power levels. Such sources suffer from large power consumption and are very bulky. Current receivers at THz frequencies rely on direct

detection, using Schottky diodes, bolometers, thermopiles, pyroelectrics, etc, which is not band selective and has a low dynamic range and sensitivity [4]. As mentioned earlier, THz radiation is absorbed by most materials, including the molecules in the atmosphere such as water vapor. For such systems, line of sight propagation is needed and even for such conditions, the range is rather limited due to the inherently high path loss. Since path-loss is relatively high and receivers are not sensitive, much effort has been placed on maximizing the available incident power to the detector. This is where nanoantennas can play a significant role.

Metals, in particular, gold, are commonly used to fabricate antennas in the THz frequency range. At THz frequencies, the lower conductivity of metal, compared to its DC conductivity, increases field penetration into the metal. This behavior of metal at THz frequencies degrades the radiation efficiency of metallic antennas [5]. In addition to the low conductivity of metal at THz frequencies, the effect of small geometric parameters of metallic antennas, specifically the width or radius of metallic traces smaller than 0.1 μm must be considered. A numerical analysis showed that small-scaled antennas, using sub-100 nm radii compared to millimeter-sized counterparts, have much lower radiation efficiency at 1 THz due to the high surface resistance of metallic traces [6]. Also, as a result of the fabrication and method of gold deposition needed for achieving thin layers with a small trace width of less than 100 nm, the conductivity values of gold are considerably lower than that of the bulk material. This lower conductivity is due to grain boundary scattering, surface scattering, and surface roughness [7, 8]. These factors can considerably reduce the theoretically predicted radiation efficiency of antennas at THz band and higher. To increase the radiation efficiency of THz antennas, the surface

impedance of the conductor should be reduced by increasing the current density across the small cross section of the antenna traces.

To control losses in small-scale antennas, materials other than metals should be considered. As a nanomaterial, Carbon Nanotubes (CNTs) have found numerous applications. The resistivity of a single CNT is lower than that of a strand of gold having the same diameter and this has been a motivating factor for utilizing CNTs in nanoantenna fabrication [9, 10]. Although a detailed discussion of CNT properties for use in antenna applications is covered in Chapter 2, a brief introduction of CNTs is given here. A CNT is a type of carbon-based cylindrical-shaped nanomaterial. The CNT's diameter ranges from 0.7 to 10.0 nm and its length can be from a few nanometers up to a few centimeters [10, 11]. As a good conductor, CNTs can support current densities as high as 10^9 A/cm^2, which is about 100 times higher than the current density that can be carried by ordinary metallic conductors [12, 13]. However the small cross section, which is on the order of a few nanometers squared, of the tube decreases the amount of current that can flow through a single CNT. Fortunately, it is possible to fabricate a large number of CNTs and lay them in parallel on a substrate to form what is known as Bundled CNTs (BCNTs). Once placed in parallel, the properties of the BCNTs, depending on the CNT density, are a scaled version of single CNT. BCNTs can in effect increase the cross section of a single CNT to enable higher current density and provide an alternative material for making nanoantennas for THz and optical frequencies. There are many factors that can affect the radiation efficiency of antennas made from BCNTs, including the number of CNTs in the BCNT, its anisotropic surface resistivity, and its wavelength scaling factor. The wavelength scaling factor refers to the inductive behavior of CNTs,

which in effect slows down the wave supported by CNTs. A careful study is needed to quantify the advantages of BCNTs over high conductivity metals such as gold as a function of frequency.

Despite the low radiation efficiency of metallic antennas at THz and optical frequencies, the field confinement and substantial field enhancement at the terminals of the metallic antennas at such high frequencies and its favorable effect to enhance the performance of the optical devices have been highlighted [14]. To understand the field enhancement and confinement, the electrical property of metals at THz and optical frequencies should be discussed first. Metals consists of atoms and free electrons and in the presence of the time-varying electromagnetic field, the electrons are not constricted by the restoring force from the atoms. The spectral dielectric property of metals is represented by the Drude model as shown in (1.1) [15].

$$\varepsilon = \varepsilon_0 \left(1 - \frac{\tau^2 \omega_p}{1+\tau^2\omega^2} - j\frac{\tau {\omega_p}^2}{\omega(1+\tau^2\omega^2)}\right) \tag{1.1}$$

where is ω_p is the plasma frequency, and τ is the scattering time. At ω_p, the metal shows zero real permittivity and τ is the average time between scattering events. Because the plasma frequencies of a typical metals such as gold and silver are higher than 2, 000 THz, the real permittivity of metals at optical frequencies such as visible or IR frequencies becomes negative. This negative permittivity of metal corresponds to the total reflection of the incident electromagnetic field from the surface of the metal. This special electrical property of metals at THz and optical frequencies leads to two interesting phenomena related to the field enhancement and confinement.

Firstly, field enhancement and confinement have been observed from the surface plasmons (SPs) which is an evanescent surface wave along the interface between metal

and a dielectric medium or vacuum. For a SP, the field magnitude decays exponentially with the distance from the interface inside the metal that support it [16]. A remarkable feature of SPs is that due to the decaying electric field with the distance of a nanoscale from the interface, the field is tightly confined near the interface and its magnitude is highly enhanced. In the case of gold interfaced with vacuum medium, the electric field magnitude in the gold medium reduces down to 1/e of its initial magnitude within 23 nm from the interface [17]. SPs have shown to provide interesting applications such as spectroscopy and sensors as well [18].

Secondly, the effect of field enhancement can also be observed with sub-wavelength metallic particles in a dielectric medium or vacuum when illuminated by an optical wave. Based on a well-known Rayleigh scattering which explains the scattering of electromagnetic waves by particles which are much smaller than a wavelength, the magnitude of the scattered field by the particles is inversely proportional to the sum of permittivity of the surrounding media and twice the permittivity of the particle [19]. At a specific band in the visible spectrum, for a certain level of negative permittivity of the metal the denominator can be made arbitrarily small and as a result the scattered field around the particle can be significantly larger than that of the incident field. This phenomenon has been demonstrated experimentally at near the visible region using fabricated nanometer-scale particles [20, 21, 22].

Field enhancement and confinement due to the interaction between the planar metal sheets and small metallic particles with optical waves are termed broadly as the plasmonic effect of the metal at optical frequency [17]. Furthermore, metallic structures

which are formed as a dipole, a bowtie antenna, a spiral antenna, and a Yagi-Uda antenna operating at optical frequencies have also been studied and fabricated [23, 24, 25, 26].

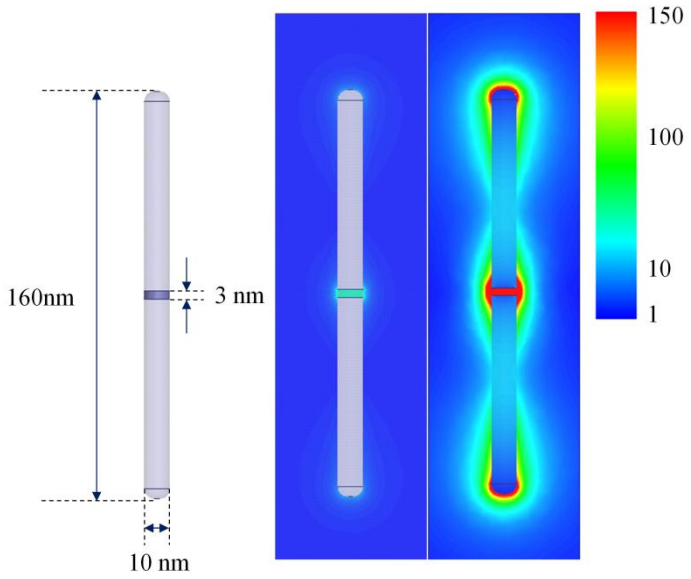

(a) (b) (c)

Figure 1.1: (a) 160 nm-length gold dipole antenna with diameter of 10 nm and the gap size of 3 nm filled by vacuum, (b) and (c) field magnitude (complex electric field) along a cut plane across the center of the antenna of the antenna consists of PEC (at f = 1,150 THz) and Drude model gold (at f = 278 THz).

Fig. 1.1 shows an example of a nanometer-scale antenna structure and the field distribution from the antenna modeled by perfect electric conductor (PEC) in (b) and gold Drude formula in (c). In the Drude formula for modeling gold, the plasma frequency is set 2,080 THz and the scattering time is set 18 fs. The Drude model using these parameters provides -54.92 of real permittivity and 1.78 of imaginary one at 278 THz. The electric field is calculated along a cut plane across the center of the antennas with the excitation of vertical polarized incident field with its field intensity of 1 V/m. The field distribution demonstrates that quite a significant field enhancement (509 V/m at 278 THz)

at the gap of the antenna structure modeled by Drude formula compared to its counterpart that consists of PEC (50 V/m at 1,150 THz). The gold antenna at its resonant frequency, shows almost 11 times higher field enhancement compared to the same antenna structure modeled by PEC. It is noted that both antennas are simulated at their resonant frequency for the same physical dimensions. As mentioned earlier, the plasmonic effects introduce substantial a downward shift in the resonant frequency.

As demonstrated in the above numerical simulations, the main reason for the high volume of research in metallic antennas at frequencies well above THz band is the significant field enhancement at the gap of the metallic antenna. The measured value of the field enhancement at the gap of the metallic antenna has been reported to within several thousands of magnitude [27, 28, 29, 30, 31]. Based on the significant field enhancement observed in metallic antennas, the possibility to improve the performance of traditional optical devices such as photovoltaics, optical detectors, sensors, and spectroscopy has been driving the research on metallic antennas at optical frequencies in the last decade [14, 32, 33, 34, 35, 36, 37].

Another favorable feature of metallic antennas in optical frequencies is their ability to focus the field in an area much smaller than the diffraction limit ($d = \lambda/2$) [14, 38, 39]. The focusing spot size of such antennas is limited by the fabrication limitation and can be smaller than tens of squared nanometers in area using the current fabrication technology [40] Another interesting phenomenon of the metallic antenna at optical frequencies is the antenna miniaturization effect as alluded to before. This phenomenon can be observed at the numerical simulation shown in Fig. 1.1. The gold antenna modeled by Drude formula shows 278 THz of its resonant frequency whereas the PEC antenna

shows 1,150 THz. This effect is due to the negative electrical permittivity of metals at optical frequencies which can be interpreted as the intrinsic inductance. This inductance of metals at frequencies above THz makes the metallic antennas look electrically larger than their physical sizes.

To maximize the performance of the previously mentioned optical devices by using the metallic antenna structure, the antenna must be designed for the maximum field enhancement at the terminals [14]. This is one of the focuses of this thesis. The application of efficient metallic antennas at near IR band for power harvesting and sensitive detector is considered. For this application, the antenna is loaded with a semiconductor p-n junction at its terminals for absorbing or detecting the incident optical signal. Then the goal of designing the geometry of the metallic antenna and the semiconductor load is to maximize the power transfer between the antenna and the semiconductor as the antenna's load. The fulfillment of this maximum power condition would determine the maximum level of improvement for such optical devices which can be expected from the field enhancement of the metallic antenna.

Before developing a method for designing the efficient metallic antennas, a desirable scope for the physical dimensions of the antenna structure and a specific operating band among optical spectrum of electromagnetic waves must be specified. Several researchers have fabricated metallic antennas of various sizes, ranging from a few nanometers to a few microns [30, 32, 41]. Electron-beam lithography (EBL), which is typically used for patterning very small metallic structures, can realize features with sizes down to the 2 ~ 4 nm range [40]. However, the patterning is circular as opposed to angular for nanometer scale resolution. The curvature of the edge provides a relatively

higher geometric uncertainty for smaller patterns (below 100nm) so the antenna performance may vary from batch to batch. Furthermore, the proper characterization of nanoantennas is expected to be difficult and, in addition, the wiring of the antenna for signal pick-up is also highly challenging. Thus, instead of using antennas with dimensions smaller than 100 nm, comparably larger antennas on the order of a few hundred nanometers, are used [42]. For this size range, an antenna can be realized with a dipole or bowtie topology while maintaining a well-defined shape. In addition, due to the size of the antenna and the inherent antenna miniaturization effect for metallic antenna at these high frequencies, IR, which has a micron-level wavelength, is chosen instead of visible light, which has a wavelength of less than 1 μm.

Furthermore, this IR range for the antenna design determines the bandgap of the semiconductor material for the purpose of absorbing or detecting IR waves. For the relatively low photon energy of IR, lower bandgap semiconductors, with respect to silicon, must be chosen. Also with this low bandgap semiconductor to absorb and detect IR signals, thermophotovoltaics (TPVs), which is a similar device as the photovoltaics but working at the IR band and IR detector are selected as the optical devices for demonstrating performance enhancement when nanoantennas are used. The details of the specifications for these devices are found in Chapters 2 and 3.

Based on the aforementioned selected size range of the antennas and the antenna load material, the impedance of the antenna and the low bandgap semiconductor load at IR band must be studied to achieve the impedance matching. For developing efficient IR devices such as TPVs or IR detectors, impedance matching between the antenna and the load is required for maximum power transfer from the incident radiation to the power

absorbed by the load. Before discussing the input impedance of the antennas operating at IR and optical frequencies, the type of current at the terminals of the metallic antennas operating at such high frequencies should be noted. Because these types of metallic antennas have a semiconductor load at their terminals instead of the 50 Ω transmission lines commonly used for microwave antenna, the antenna at optical frequencies has displacement current rather than conduction current at its terminals. Thus the input impedance of the antenna can be defined as the ratio between the driving voltage difference along the gap and the total flux of induced optical displacement current [31, 43]. Based on this concept of the input impedance of metallic antennas at optical frequencies, numerical simulations of these antennas have shown low resistance at the series resonance, which occurs in the optical frequency range, due to smaller radiation resistances [14]. On the other hand, the semiconductor load of the antenna generally exhibits a high resistance and high reactance at the desirable frequency because it has a high dielectric constant and a size on the order of nanometers [10, 44]. This discrepancy between the antenna impedance and its load impedance at the series resonance could decrease the field enhancement at the terminals and prevent the maximum power transfer from the incident radiation in free space to the antenna's load.

Thus the impedance mismatch problem shown in the metallic antennas at optical frequencies with a semiconductor p-n junction should be resolved to build efficient optical devices. Firstly, a method for matching the low resistance of the antenna with the high resistance of the semiconductor material needs to be found. Secondly, the high reactance of the load should be canceled out because high reactance significantly perturbs the resonant frequency of the metallic antenna. For these purposes, the design parameters

such as the antenna topology, the semiconductor load dimensions, and the impedance matching network structure to compensate the reactance of the semiconductor load can be optimized. One thing to note is that the resonant frequency for the impedance matching must be placed at the desired frequency where the semiconductor for the antenna load exhibits its maximum quantum efficiency. From the optimized antenna with the optimum semiconductor load, the field enhancement at the terminals of the optimized antenna is calculated to confirm that the antenna design fulfills the maximum power transfer at the desired frequency. Finally, the optimized antenna element can be integrated into an antenna array as a realistic optical device. The method to arrange the antenna and connect those antennas with wires is carefully investigated.

1.2 Thesis Outline

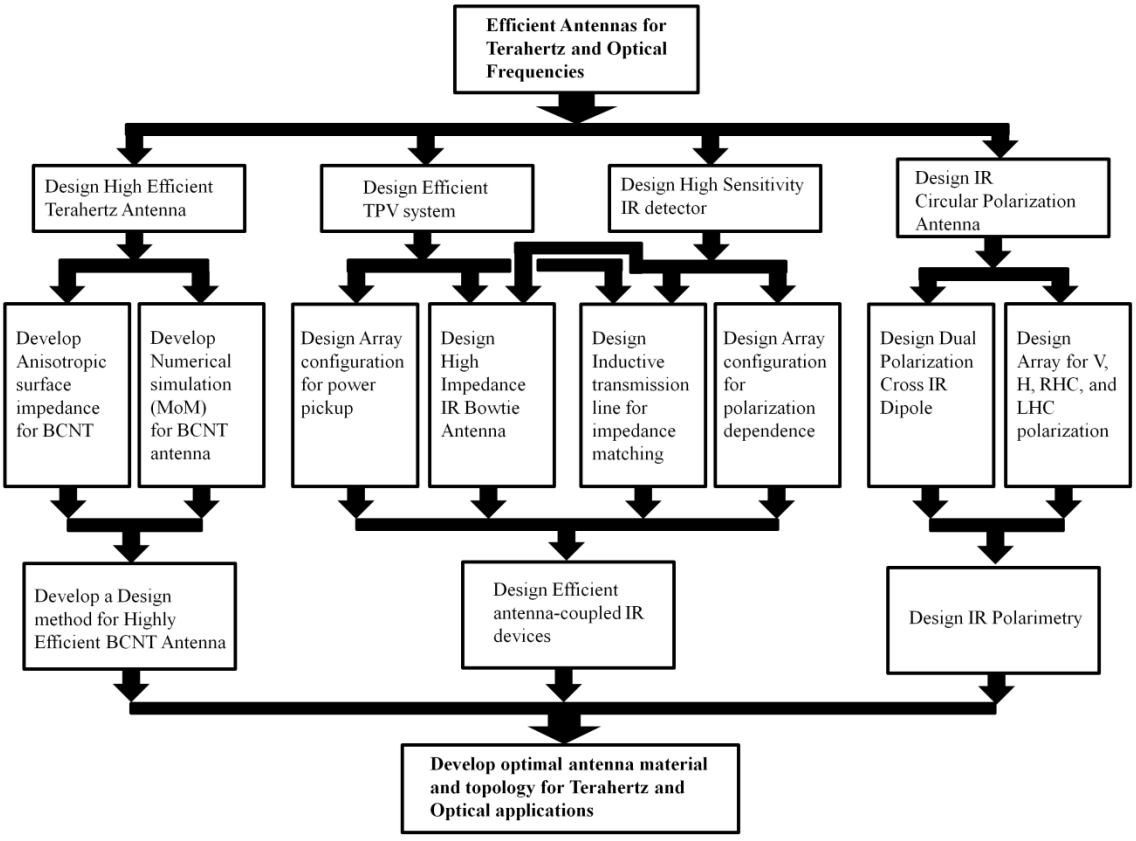

Figure 1.2: Dissertation Overview.

In this thesis, efficient antennas using a new nanomaterial designed for THz and optical frequencies are investigated to overcome the low efficiency of metallic antennas at THz and higher frequencies. In addition, efficient metallic plasmonic antennas used for enhancing the performance of thermophotovoltaics (TPVs) power transducers and uncooled IR detectors are discussed.

Chapter 2 addresses the low radiation efficiency problem of metallic antennas at THz frequencies by substituting them with a highly conductive nanomaterial, BCNTs. In this analysis, conventional half-wavelength strip antennas patterned in two dimensional (planar) antennas with lengths from 3 to 150 μm are considered. For these antenna structures, the material for the two dimensional sheet is chosen to be either gold or BCNT. A sheet of BCNT is modeled using a thin resistive sheet with an anisotropic surface resistivity tensor and for gold, the Drude model is used. The structure of the two types of antennas is analyzed using the Methods of Moments (MoM) and the calculated radiation efficiency and input impedance are compared. Based on the numerical analysis, the possibility of using BCNT as an efficient antenna radiator in THz frequencies is discussed. This analysis also provides fabrication criteria for the BCNT strip antenna to outperform the gold antenna in terms of radiation efficiency.

Chapter 3 discusses the gold antenna design parameters, in terms of the length and shape to maximizes near field enhancement at IR frequencies when analyzed through full wave numerical simulation. IR bands are considered because the longer wavelengths, with respect to the visible band, relax the patterning accuracy needed for antenna fabrication. A low bandgap semiconductor, indium gallium arsenide antimonide

(InGaAsSb), which has been used for traditional Thermophotovoltaics (TPVs) is chosen as the load to absorb the IR signal [45]. A nanometer-sized block of InGaAsSb is placed at the antenna's terminals to serve as the antenna load. Optimization on the topology of the antenna and the InGaAsSb block size is conducted at the desired frequency, where the maximum quantum efficiency of InGaAsSb is observed, for maximum power transfer. Finally, the optimized antenna, which operates at its high impedance mode in conjunction with an embedded matching network achieves the maximum power transfer, and the field enhancement factor at the InGaAsSb block is presented.

For creating an efficient TPV system, an array of gold antennas with the optimized topology is introduced. The infinite array of the antennas is compared with the traditional bulky TPV cell made from InGaAsSb in terms of the power absorption efficiency which is the percentage of the absorbed power to incident power. The improvement in the absorption efficiency of the array of the antennas for a TPV system is quantified. Also a novel method for designing metallic traces to connect the IR antennas in the array for a TPV system is discussed.

Chapter 4 analyzes the sensitivity of an optimized antenna combined with an InGaAsSb block to realize an IR detector. Detectivity, the normalized sensitivity to a 1-cm^2 area and 1-Hz of noise bandwidth, is determined for the sensitivity analysis. The sensitivity improvement of the optimized antenna in comparison to traditional bulky IR detectors is calculated [46]. A polarization-sensitive detector array and the optimized metallic traces connecting the antenna elements are presented.

Chapter 5 introduces the application of nanoantennas for use in IR polarimetry systems. In contrast to traditional bulky semiconductor IR detectors, the unique

properties of antenna-mounted IR detectors can be used for sensing the polarization of the wave. In addition to linear polarization, circularly polarized (CP) IR antennas have the potential to detect CP IR signals. By implementing vertical, horizontal (or 45°-tilted), right-handed and left-handed CP antennas in a single system, an IR polarimetry system can be realized. Also, the arrangement of the four different polarized antennas and the metallic lines for signal pickup is introduced as the final step for designing an IR polarimetry system. The CP antenna using a 90°-phase shift between the vertical and horizontal dipole is simulated and the test structure of the same antenna topology operating at 2.58 GHz is fabricated. The perfect CP signal from measurement is presented. The application of the CP antenna structure at the GHz frequency for a polarization-based direction finding system is also presented, and lastly, the application of the IR CP antennas for IR polarimetry is discussed.

Finally, Chapter 6 provides a summary of the studies presented in the thesis. The important accomplishments are outlined and suggested future work is introduced.

Chapter 2

Efficient Dipole Antenna using a Nanomaterial, Bundled Carbon Nanotubes

In this chapter, the performance of bundled carbon nanotubes (BCNTs) as a conducting material for the fabrication of antennas in the terahertz (THz) frequency range and above is evaluated. The performance is compared against gold film, which is usually used for antenna fabrication. The macroscopic behavior of BCNTs is modeled by an anisotropic resistive sheet model which is extracted from the discrete circuit model of a single wall carbon nanotube (SWNT). The surface impedance of BCNTs is controlled by the number density of BCNTs, which means the number of SWNTs per unit width of BCNTs. Numerical simulations using the method of moments (MoM) and the mixed potential integral equation (MPIE) are performed to quantify radiation efficiencies of resonant strip antennas composed of BCNTs and thin gold films. For accurate high frequency simulations of antennas constructed from a thin gold layer, the Drude-Smith model is used to calculate the conductivity of gold film [5]. Simulations are carried out from 1 THz to 50 THz for conventional half-wave strip antennas.

2.1 Introduction

Carbon nanotubes (CNTs) have certain unique electrical properties which are used for many applications in the field of nanotechnology, electronics, and optics. A single wall carbon nanotube (SWNT) has a cylindrical geometry with an extremely high aspect ratio. Although a SWNT has a rather high conductivity, its resistance per unit length is fairly high because of its very small radius (on the order of a few nanometers) [47]. These properties limit its direct utilization for RF applications, such as electrical interconnects and radiating elements. To circumvent this problem, bundled CNTs (BCNTs) are proposed to reduce the high intrinsic resistance of a SWNT [48, 49].

Some experimental work in analyzing the electrical properties of BCNTs has already been reported. Laboratory measurements up to 50 GHz have shown a relatively large kinetic inductance for the SWNT, which is scalable with the number of SWNTs within the bundle [48]. In the bundle structure, the scalability of a SWNT's resistance, which is predicted by the Luttinger liquid theory is verified in a measurement setup where a BCNT was fabricated to behave as a 50Ω transmission line up to 20 GHz [49]. Results of these experiments suggest that the equivalent circuit model of BCNTs, composed of N parallel SWNTs, can simply be obtained from the equivalent circuit of an individual SWNT whose components' value are divided by N.

Theoretical properties of SWNT as an antenna have also been studied. In [49, 50], the theoretical analysis of a SWNT as a dipole antenna predicts a slow propagation velocity within the tube, high input impedance, and very low radiation efficiency. Also in [6], the radiation efficiency of a dipole antenna with a nanometer radius was numerically simulated. However, no experimental measurement of the radiation efficiency has yet

been reported. The previous studies have shown that dipole antennas with radii smaller than hundreds of nanometer are not effective radiators in the microwave regime; hence, SWNT or nanowire is suggested for very high frequencies with nanometer-scale wavelength.

In this chapter, the performance of BCNTs as a material for fabrication of antennas at THz frequencies and above is investigated using a numerical technique developed for this purpose. The discrete equivalent circuit of a SWNT, proposed in [51], is used for electromagnetic modeling of BCNTs. Hence a series circuit model composed of the kinetic inductance (16 nH/μm) and the resistance (6.5 kΩ/μm) is utilized to represent a strand and then, parallel circuits of SWNTs are employed to obtain a macroscopic boundary condition for a planar BCNT structure. The premise for re-examining SWNTs as a material for antennas stems from the fact that the quality factor (Q) of the series resistor-inductor (RL) model of an individual SWNT is approximately 100 at THz frequencies ($f > 6.5$ THz). Such a high Q factor of a SWNT at THz frequencies is preserved in the bundle structure due to the parallel connection of SWNTs.

Also, the one dimensional electron transport in SWNT indicates that the concept of skin depth for this conductor is not applicable. Thus the material still shows relatively a high conductivity at very high frequencies, although the thickness of a single or multiple layers of a planar BCNT strip can be extremely small compared to the wavelength. On the other hand, the surface resistivity of conventional conductors is a function of skin depth and monotonically increases as frequency increases. Hence, at a certain high frequency in the THz regime, the radiation efficiency of BCNT antennas is expected to surpass the radiation efficiency of metallic antennas. To account for the high

frequency properties of metals (thin gold film in this chapter), the Drude-Smith model is used [5].

This chapter is organized in two parts; first, an anisotropic resistive sheet model to represent BCNTs electromagnetically is presented. Then, a numerical model based on the method of moments (MoM) for electromagnetic simulation of antennas which consist of BCNTs and gold film is developed. The radiation efficiencies of both types of antennas are computed and compared as a function of frequency and the density of BCNTs, the number of SWNTs per unit width. Finally, a cross over frequency point at which the BCNT antenna outperforms its metallic counterpart is identified.

2.2 Carbon Nanotubes

A salient feature of CNT molecules is their atomic arrangement. Carbon nanotubes consist of graphene sheets that are rolled across an axis vector to form a cylindrical geometry. The axis where the carbon hexagonal configuration of graphene sheet is rolled determines the conducting property of the CNT [52, 53]. Among the semiconducting and metallic CNTs, the metallic variety is highly conductive ($> 10^8$ A/cm^2) which allows for its use in the design of antenna radiators and interconnects [54]. Also, CNTs can be categorized as either single wall nanotubes (SWNTs) or multi wall nanotubes (MWNTs), based on the number of layers of graphene sheets that is rolled up to form the structure. The metallic SWNT and its bundle structure are considered in this chapter.

As a fundamental element of bundled CNTs (BCNTs), the SWNT is synthesized by the chemical vapor deposition (CVD). In recent years, significant attention has been

given to developing very long strands of CNTs. The synthesis methods have been developed to fabricate centimeter-long carbon nanotubes [12].

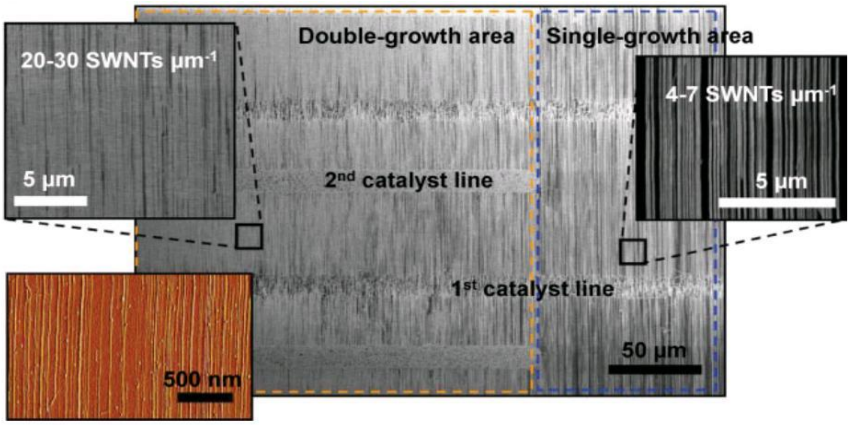

Figure 2.1: Densely aligned carbon nanotubes using repetitive CVD growths [55].

On the other hand, for the fabrication of bundles of CNTs, dielectrophoresis alignment of SWNT has been used [48]. Also, parallel arrays of SWNTs were densely grown along the patterned catalyst lines by using photolithography or polydimethylsiloxane (PDMS) on quartz wafers [56]. Both methods show that a BCNT density can be increased to approximately 10 CNTs/µm. Also a nanofabrication group has demonstrated that multiple growths of SWNTs using CVD method in a quartz substrate can realize the density up to 45 CNTs/µm as shown in Fig. 2.1 [55]. In a BCNT, although the electrons in each SWNT predominantly pass along the tube axis, there is also some movement in the transverse direction, which indicates that electrons can jump to adjacent SWNTs. Even though this microscopic electron transport occurs randomly, the reported experiments have shown that the overall current is axial and that the inductance of the BCNT is equal to the kinetic inductance of a SWNT divided by the number of SWNTs in the bundle [48]. This fact justifies the macroscopic equivalent circuit model of BCNTs,

which is simply represented by the circuit elements of parallel connected SWNTs in the bundle structure.

2.3 Resistive Sheet Model of Bundled Carbon Nanotube

To examine the electromagnetic properties of BCNTs arranged in a planar fashion, a macroscopic model is needed. Since the thickness of a layer of BCNTs is much smaller than the wavelength up to optical frequencies, such material can be modeled by a resistive sheet [57]. The continuity of a tangential electric field is maintained across such sheets which can support induced electric current flowing over them. If n̂ is the unit vector normal to the resistive sheet which is drawn to the upward (positive) side and denotes the discontinuity across the sheet, the boundary conditions are [58]:

$$\begin{aligned} \left[\hat{n}\times\overline{E}\right]_{-}^{+} &= 0, \\ \hat{n}\times\left(\hat{n}\times\overline{E}\right) &= -R\overline{J} \end{aligned} \tag{2.1}$$

where $\overline{J} = \left[n\times\overline{H}\right]_{-}^{+}$.

and R is the complex surface resistivity. Assuming that the scalability property of BCNTs is valid, a macroscopic surface resistivity for planar BCNT can be obtained. However, as SWNTs can predominantly support axial currents, the surface resistivity can no longer be assumed to be a scalar.

2.4 Resistivity of Bundled Carbon Nanotubes

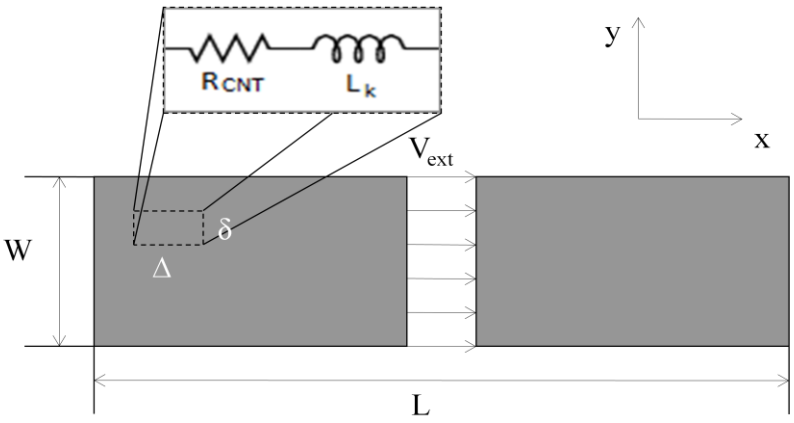

Figure 2.2: Geometry of a strip antenna made up of bundled Carbon Nanotubes.

Fig. 2.2 illustrates the proposed geometry of a strip dipole antenna constructed from strands of SWNTs. These strands form an extremely thin conducting layer (approximately ~10 nm) which is capable of supporting the electric current along the antenna axis [47]. In the bundle, it is assumed that each single nanotube, represented by the equivalent circuit model of the SWNT, is all connected in parallel. Also, it is assumed that the electrons move only along the axis of SWNT, so that only the electric field component parallel to the strands can excite the surface currents.

Following the boundary condition (2.1) and referring to Fig. 2.2, the tangential electric field is related to the surface current by:

$$E_x = R_x J_x \tag{2.2}$$

where R_x is the surface resistivity along the SWNT axis. Considering a small rectangular segment of the surface, the voltage across the length of the rectangle can be obtained from

$$v_x = E_x \Delta \tag{2.3}$$

Also, the current flowing through the width of the rectangle is given by

$$i_x = \delta J_x \tag{2.4}$$

The equivalent impedance of the rectangular segment can be obtained from the resistance (R_{CNT}) and the kinetic inductance (L_K) per the unit length of SWNT as well as the number density (N) of SWNTs in the bundle and is given by

$$Z = \frac{(R_{CNT} + j\omega L_K)\Delta}{N\delta} \tag{2.5}$$

where

$$R_{CNT} = 6.5 k\Omega / \mu m,$$
$$L_K = 16 nH / \mu m$$

Using (2.2) ~ (2.5), it can easily be shown that BCNT resistivity can be computed from

$$R_x = \frac{R_{CNT} + j\omega L_K}{N} \tag{2.6}$$

As shown, the surface impedance (complex resistivity) of the BCNTs can be modified by its number density. As will be discussed later, matching the antenna to transmission lines of reasonable characteristic impedance values require a large number of SWNTs in parallel. As mentioned before, the current can flow only in one direction and as a result, the equivalent resistivity of the BCNT is not isotropic. In this case, (2.1) can be replaced with

$$\hat{n}\times\left(\hat{n}\times\overline{E}\right)=-\overline{\overline{R}}\cdot\overline{J},$$
$$\overline{\overline{R}}=\begin{bmatrix} R_x & 0 \\ 0 & R_\infty \end{bmatrix} \tag{2.7}$$

where $R_\infty >> R_x$. This equation only models the BCNT sheet. Usually, BCNTs are fabricated on a substrate. To reduce or eliminate dielectric loss associated with the substrate, a thin membrane can be fabricated over silicon or quartz substrates over which the BCNT antenna can be deposited. Then, the substrate under the antenna can be removed [59]. In this case, the antenna will be supported by a thin membrane (~ 1 μm thick). This thin dielectric layer can also be modeled by an isotropic resistive sheet whose resistivity is given by [58]

$$R_m=\frac{-j\eta}{\kappa_0\tau\left(\varepsilon_r-1\right)} \tag{2.8}$$

where t, e_r, η, and k_0 are, respectively, the thickness, the relative dielectric constant of the membrane, the characteristic impedance, and the propagation constant of surrounding free space. This surface resistivity is capacitive and is placed in parallel with the resistivity of the BCNT surface. However, R_m is usually a large quantity, which can be ignored, since the membrane thickness is very low.

2.5 Method of Moment (MoM) Formulation

In order to compute the characteristics of the proposed strip dipole antenna constructed from the BCNTs, MoM formulation based on the mixed potential integral equation (MPIE) for an anisotropic resistive sheet is developed. Using the magnetic vector potential $\overline{A}$ and the electric scalar potential Φ ,

$$\bar{E}_{scat}(\bar{r}) = -j\omega \bar{A}(\bar{r}) - \nabla\Phi(\bar{r}) \tag{2.9}$$

where

$$\bar{A}(\bar{r}) = \int_s \bar{\bar{G}}(\bar{r},\bar{r}') \cdot J_s(\bar{r}')\, d\bar{r}' \tag{2.10}$$

$$\Phi(\bar{r}) = \frac{1}{-j\omega} \int_s g(\bar{r},\bar{r}') \nabla \cdot J_s(\bar{r}')\, d\bar{r}' \tag{2.11}$$

and $\bar{\bar{G}}(\bar{r},\bar{r}')$ and $g(\bar{r},\bar{r}')$ are, respectively, the dyadic and scalar Green's function of the free space. After discretizing the surface of the resistive sheet into triangular facets and expanding the unknown surface current, J_s is expressed as a summation of Rao-Wilton-Glisson (RWG) basis functions [59]. Then by testing (2.7) with the same basis function, the surface current density can be calculated. By plugging $E = E_{inc} + E_{scat}$ into (2.7) and using (2.9) ~ (2.11), the following matrix equation is formed.

$$ZI = V \tag{2.12}$$

where V is the excitation obtained from E_{inc}. In the strip dipole antenna geometry shown in Fig. 2.2, the impinging voltage along the gap between two BCNT sheets defines the incident field (E_{inc}) which is formulated using a delta-gap model. In the model, constant incident field only exists over the triangular facets of the rectangular-shaped feed which connects the two BCNT sheets [60].

2.6 Conductivity of Thin Gold Film

In the THz and optical regime, the Drude model provides the conductivity of a good conductor (copper or gold) as a function of frequency. Such frequency dependence of the optical conductivity is due to the fact that free electrons moving near atoms in a

good conductor are not subject to the Lorentz restoring force of the atoms, in the presence of the time-varying electric field.

2.6.1 Drude-Smith Model

The Drude-Smith model, optimized specifically for thin gold film, provides its THz conductivity and has been verified in an experimental setup [5]. A formulation of the complex conductivity of thin gold film at THz frequencies is given by

$$\sigma(\omega) = \frac{\varepsilon_0 \omega_p^2 \tau}{1 + j\omega\tau}\left(1 + \frac{v_i}{1 + j\omega\tau}\right) \tag{2.13}$$

where ω_p is the plasma frequency, τ is the scattering time, and v_i is the persistence of velocity. The plasma frequency ($\omega_p/2\pi$) of thin gold film is 2,080 THz and its scattering time is 18 fs [17]. Also, v_i represents the ratio of electron initial velocity to its velocity after the first collision to nearby atoms. However, the velocity persistence is only effective in the case of a film thinner than 20 nm. For antenna applications, the proposed thickness of a thin gold film can be chosen to be much higher than the transition thickness of 20 nm. Henceforth v_i is set to zero in the Drude formula for calculating conductivity of thin gold film. The general complex conductivity given by

$$\sigma(\omega) = \sigma_r + j\sigma_i \tag{2.14}$$

(2.14) can easily be converted to complex permittivity which is computed from:

$$\varepsilon_c(\omega) = \varepsilon_0\left(1 + \frac{\sigma_i}{\omega\varepsilon_0} - j\frac{\sigma_r}{\omega\varepsilon_0}\right) \tag{2.15}$$

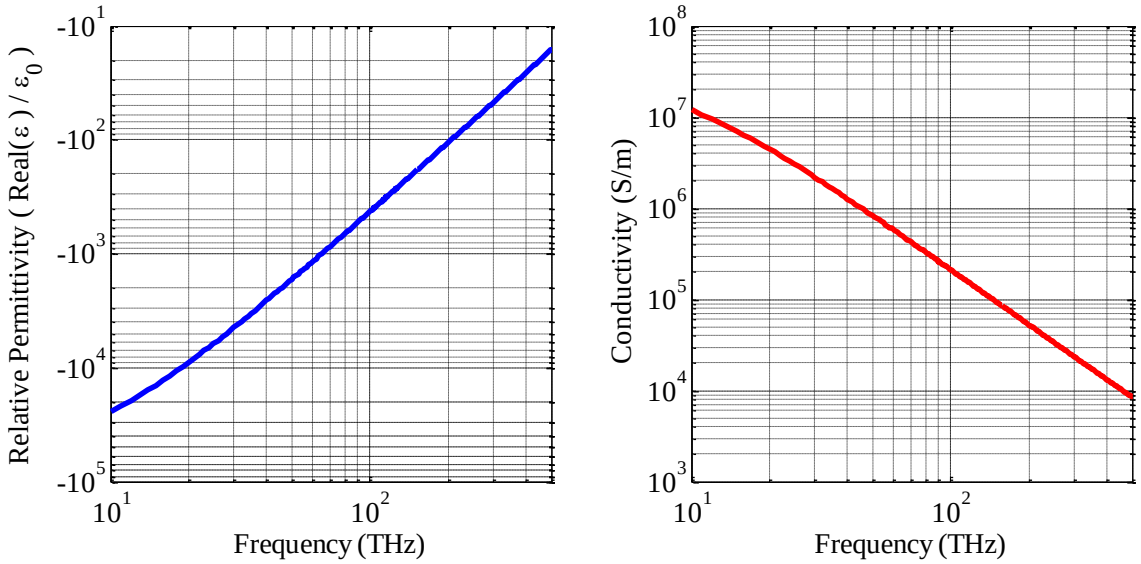

Figure 2.3: Relative permittivity and conductivity (real) of thin gold film as a function of frequency.

The real conductivity decreases in a Lorentzian line-shape as frequency increases. The imaginary conductivity has a minimum near 10 THz and its magnitude surpasses the magnitude of the real conductivity at higher frequencies. As shown in Fig. 2.3, the Drude model predicts lower conductivity and higher permittivity for thin gold films when compared to bulk gold at very low frequencies (bulk gold conductivity at DC is 4.1×10^7 S/m).

2.6.2 Surface Resistivity of Thin Gold Film

Since the penetration depth of thin gold film at THz frequencies is still much smaller than the thickness of the film practically used for antenna fabrication (> 1 μm), the boundary condition can be expressed in terms of equivalent surface impedance given by:

$$R_s = \frac{\alpha + j\beta}{\sigma(\omega)} \approx \sqrt{\frac{j\omega\mu}{\sigma(\omega)}} \tag{2.16}$$

where a and b are the attenuation and propagation constants in the gold medium, while σ(ω) is the complex conductivity given by (2.14). The approximation is valid when $|\sigma(\omega)| >> \omega\varepsilon_0$. According to the Drude model, the negative real permittivity of gold at THz frequencies corresponds to an inductive reactance as opposed to the constant permittivity of free-space assumed for good conductors at low frequencies. (2.16) is valid when the thickness of metal is infinite and it provides a good approximation when the thickness of thin gold film used for the strip antenna is set to twice the skin depth. The skin depth is simply the inverse of the attenuation constant (d = 1/a). Similar to the resistive sheet model, the boundary condition of thin gold film is given by

$$\begin{aligned} &\hat{n} \times \left(\hat{n} \times \overline{E} \right) = -R_s \overline{J}_s, \\ &\overline{J}_s = \hat{n} \times \overline{H} \end{aligned} \tag{2.17}$$

where $\overline{J}_s$ is an equivalent surface current on thin gold film.

2.7 Antenna Simulation

To evaluate the performance of an antenna composed of BCNTs or thin gold film, the length (L) of the strip dipole antenna in Fig. 2.2 is varied to obtain its fundamental resonance over the frequency range of 1 ~ 50 THz.

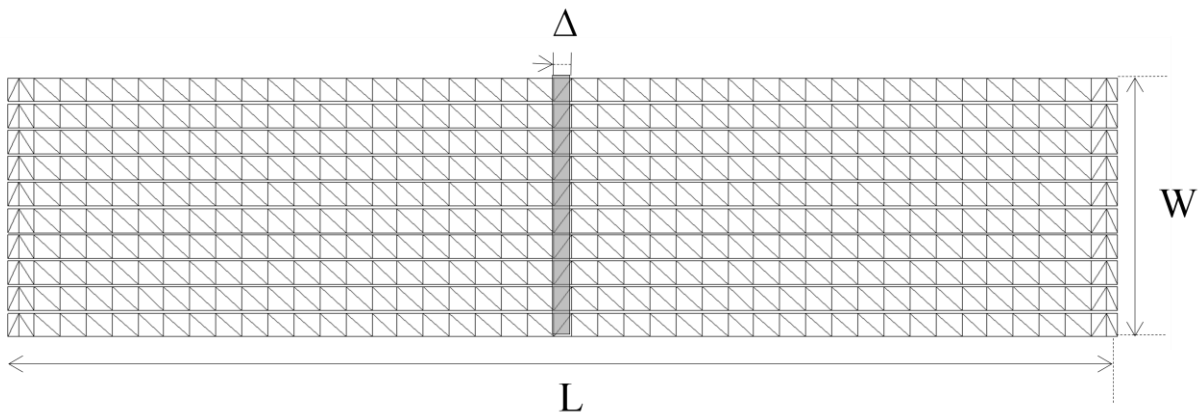

Figure 2.4: Strip dipole antenna geometry fed at center using a thin voltage gap.

The antennas are excited by a voltage gap at the center as shown in Fig. 2.4. The width (*W*) is chosen to be *L*/12 and the antenna feed gap (Δ) is set to λ/100.

2.7.1 Strip Antenna

The input impedance and the reflection coefficient, using 50Ω port impedance, are then studied to evaluate the performance of BCNT and gold antennas operating at the same frequencies. The resonant length of BCNT antenna (*L*) turned out to always be less than half of the wavelength at operating frequency due to the kinetic inductance of its equivalent circuit.

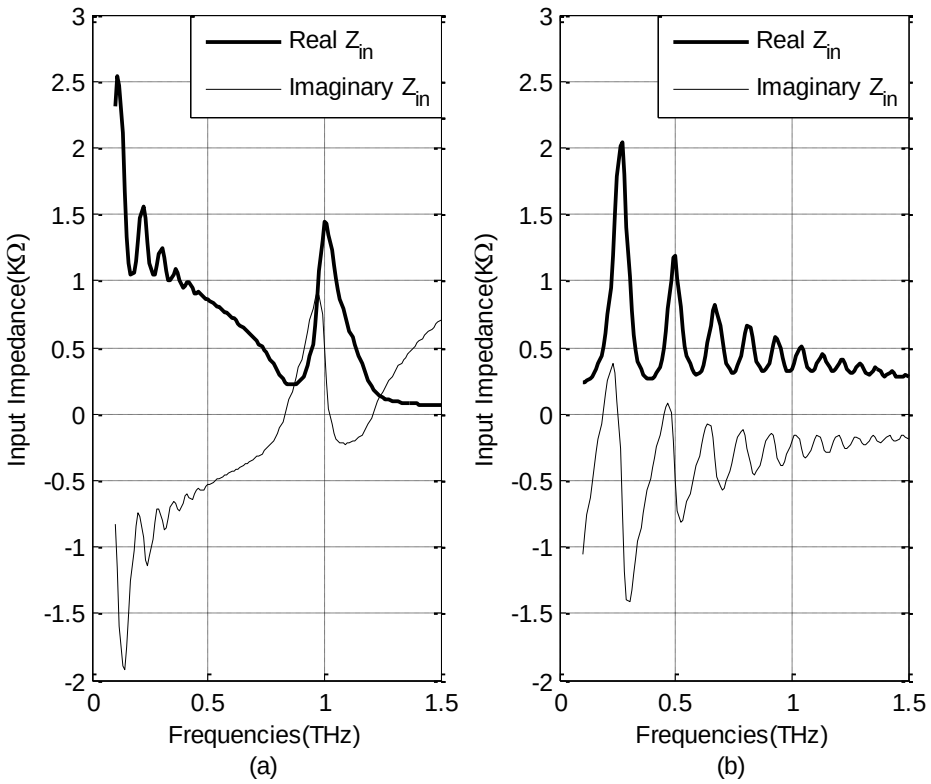

Figure 2.5: Input impedance of 150 μm strip antenna with BCNT density of (a) N:10 [CNTs/μm], (b) N:50 [CNTs/μm].

Two strip BCNT antennas with density values of 10 and 50 CNTs/μm are considered. The antenna length was chosen to be 150 μm corresponding to an ideal dipole antenna operating at 1 THz. Such number density values are realizable in current nanofabrication facilities; however, as shown in Fig. 2.5, the input impedance of these antennas are rather high (in kΩ range) and cannot be matched to any realizable transmission line. It is also shown that the inductive reactance is quite large. This simulation clearly indicates that such low densities of BCNTs cannot be used as a viable antenna due to very low mismatch efficiency.

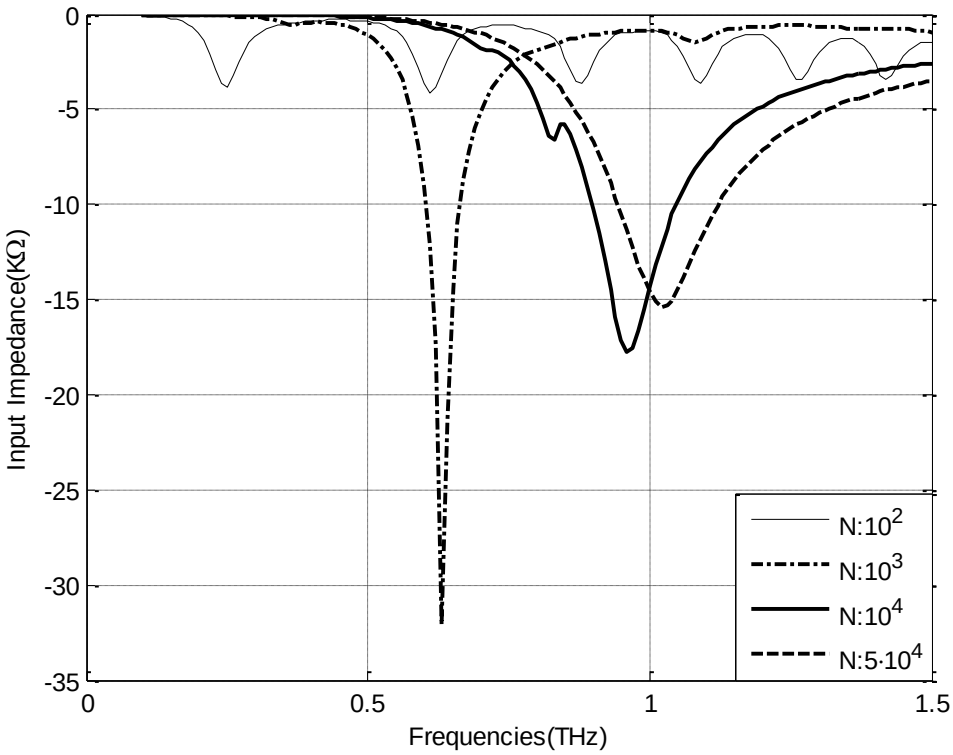

Figure 2.6: Reflection coefficient of 150μm strip antenna with different BCNT densities [CNTs/μm].

Higher BCNT number densities, however, lowers the input impedance of the antenna. Fig. 2.6 indicates the input reflection coefficient of a 150 μm antenna for different BCNT density values using a 50 Ω port (transmission line). The first resonance is approximately 0.25 THz corresponding to BCNT density of 10^2 [CNTs/μm]. It is also shown that a good impedance match still cannot be achieved without an external matching network due to high surface resistance and inductance of the equivalent anisotropic resistive sheet. The miniaturization effect is also notable. Basically, the antenna is resonant at almost 1/4 of a perfect conductor antenna of the same size. This is accomplished due to the fact that the inductance of the equivalent resistive sheet has compensated the capacitive reactance of a short dipole antenna. Fig. 2.6 also illustrates

the performance of a 150 μm strip antenna for higher BCNT density values. As shown, at BCNT density values above 10^3 [CNTs/μm], the antenna can easily be matched (without external matching elements). In these cases, the surface resistance and inductance are much reduced while maintaining the quality factor. Different miniaturization factors with a good impedance match can be accomplished in a high BCNT density range (> $5 \cdot 10^2$ [CNTs/μm]). It is important also to point out that most SWNTs are assumed to have diameters of approximately 1nm in the bundle [56] and thus it is impossible to exceed density values beyond 10^3 [CNTs/μm] in a single sheet. The BCNT density values mentioned here can be regarded as the equivalent density values of BCNTs assuming SWNTs of almost zero diameter spread on a single sheet.

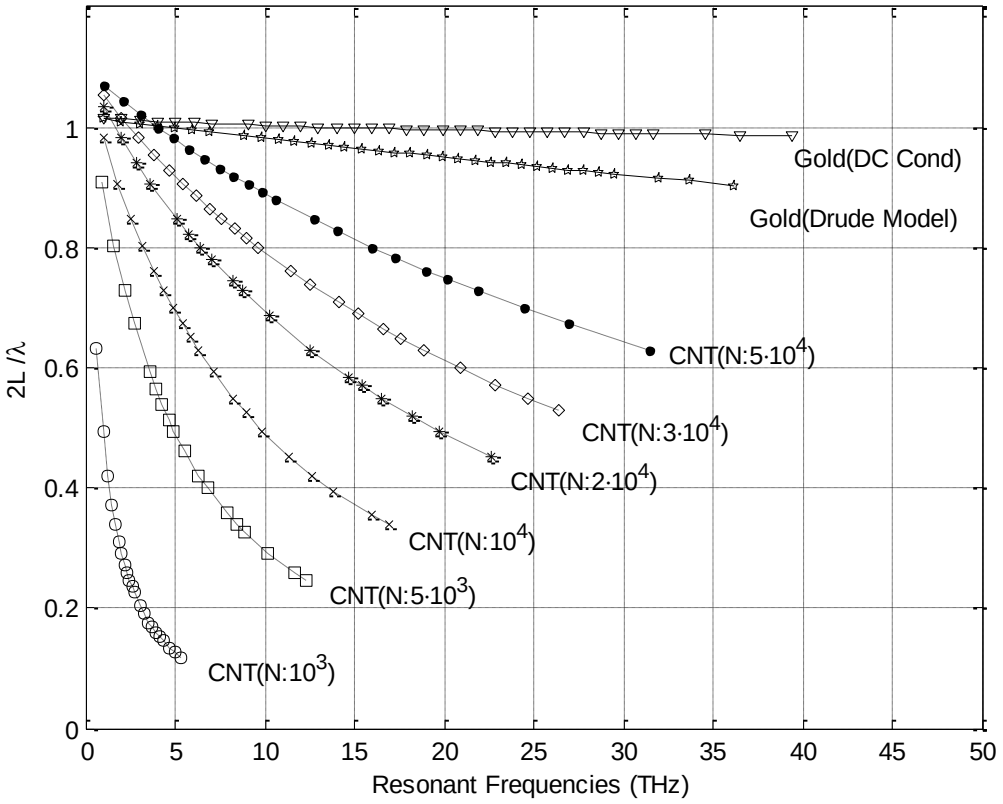

Figure 2.7: Normalized antenna length ($2L/\lambda$) versus resonant frequencies.

To demonstrate the miniaturization effect of BCNTs as a function of frequency, a large number of BCNT antennas are simulated. For a given BCNT density, strip dipole antennas whose lengths are equal to half of wave lengths from 1 THz to 50 THz were designed and their first resonant frequencies were determined. The resonant frequency corresponds to a frequency at which the antenna input reactance is zero (not necessarily matched to the port impedance). The miniaturization factor defined by ($2L/\lambda$) versus resonant frequency is shown in Fig. 2.7 for different BCNT density values. Also, the same quantity for the thin gold antenna using the conductivity of bulk gold at low frequencies and the Drude model for gold is shown. As the density of BCNT increases from 10^3 to $5 \cdot 10^4$ [CNTs/μm], the normalized antenna length approaches unity. This is due to the fact that the density of BCNT is inversely proportional to the inductance of the bundle, so that the lower density causes a lower resonant frequency and identically a higher resonance wavelength. The BCNT antenna with the density of $5 \cdot 10^4$ [CNTs/μm] has a surface resistivity which is very similar to thin gold film in low THz frequencies, whereas it still has a certain finite reactance causing further antenna miniaturization. As the thin gold film becomes more inductive at higher frequencies, the normalized length of thin gold film antenna becomes smaller. Basically, at frequencies higher than 5 THz, the normalized length is clearly lower than unity, since the inductive reactance of the surface impedance of thin gold film, as predicted by the Drude model, is dominant. Also, to effectively demonstrate the relationship between the miniaturization effect and the number density of BCNT antenna, the normalized antenna length as a function of BCNT number density is shown in Fig. 2.8.

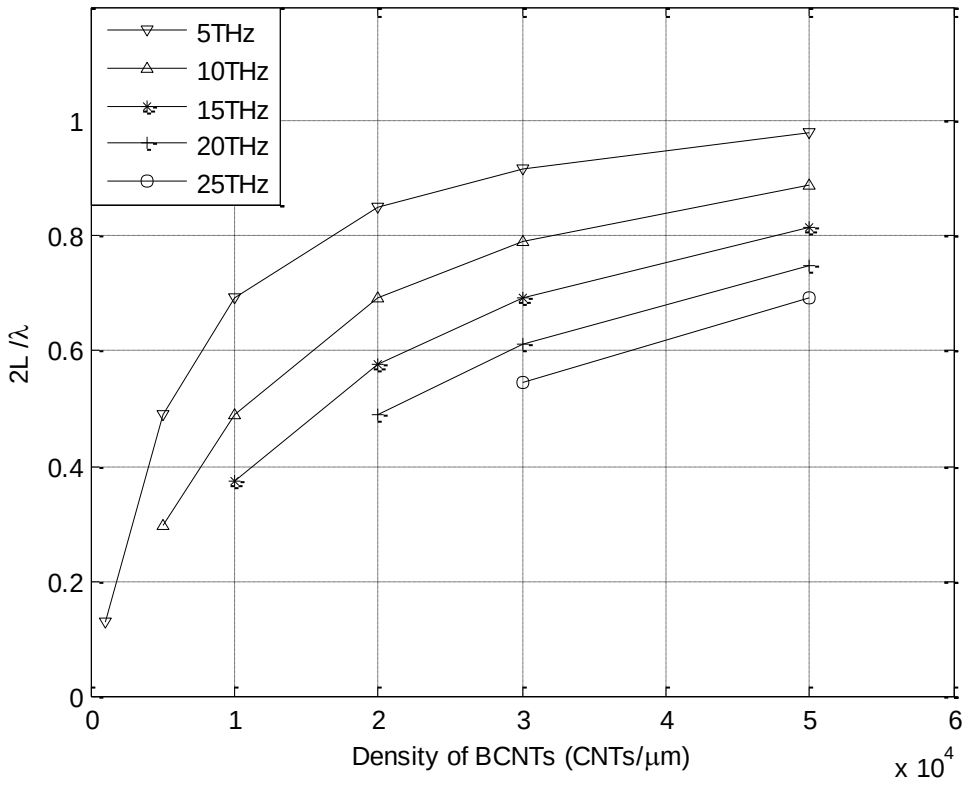

Figure 2.8: Normalized antenna length ($2_L/\lambda$) versus density of BCNT.

Each line indicates the normalized length at a specific resonant frequency of BCNT antennas from 5 THz to 25 THz. It can be seen from Fig. 2.8 that both lower number densities and smaller antenna lengths result in shorter normalized antenna lengths, hence greater overall antenna miniaturization.

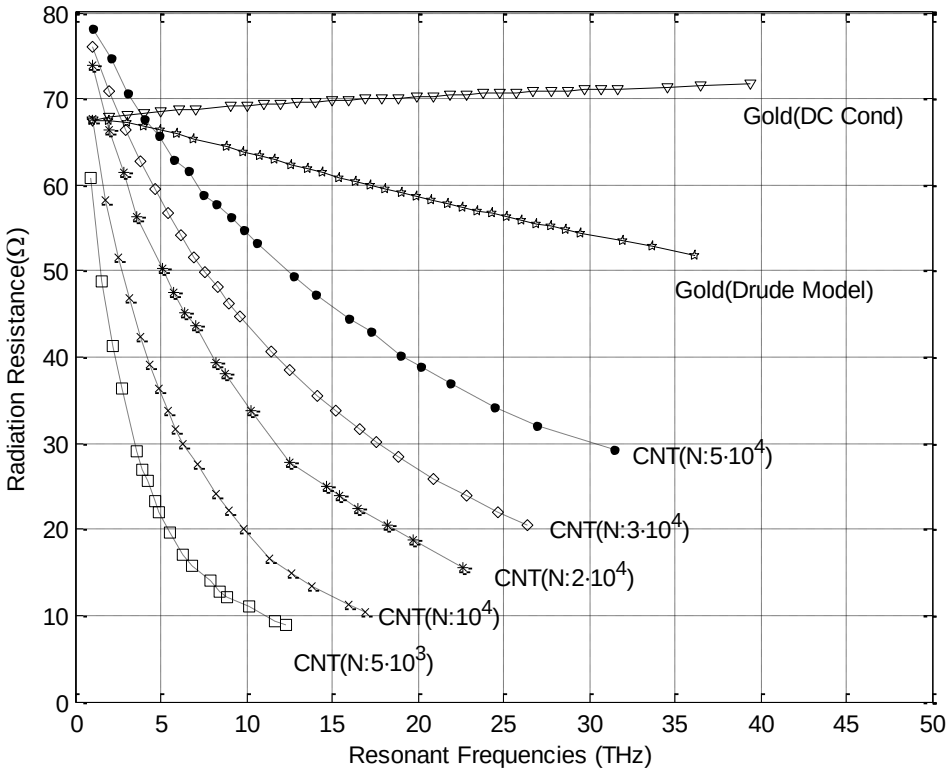

Figure 2.9: Radiation resistance of BCNT (N is higher than $5 \cdot 10^3$[CNTs/μm]) and thin gold film at its resonant frequencies.

Fig. 2.9 illustrates the radiation resistance of the same strip dipole antennas used in Fig. 2.8 as a function of frequency and BCNT number density. The radiation resistance of dipole antennas decreases as the antenna length decreases. This expected behavior is observable in Fig. 2.9 for BCNT and thin gold antennas simulated in Fig. 2.8. It is noteworthy that BCNT antennas with densities in the range of 10^3 to $5 \cdot 10^4$ [CNTs/μm] have input radiation resistance from 10 Ω to 80 Ω. That can easily be matched to conventional 50 Ω port impedances.

2.7.2 Radiation Efficiency

One of the most significant features of an antenna is its radiation efficiency. As mentioned earlier, due to increasing quality factor of BCNTs with frequency, the radiation efficiency of antennas made with BCNTs is expected to be better than the radiation efficiency of metallic antennas at a certain high frequency. In this section, the radiation efficiency of strip dipole antennas made up of BCNTs with different densities is calculated at their first resonant frequencies. These values are then, compared to those of thin gold film antennas at their corresponding first resonant frequencies. The far-field radiation power is calculated on a sphere whose radius is 1,000 λ.

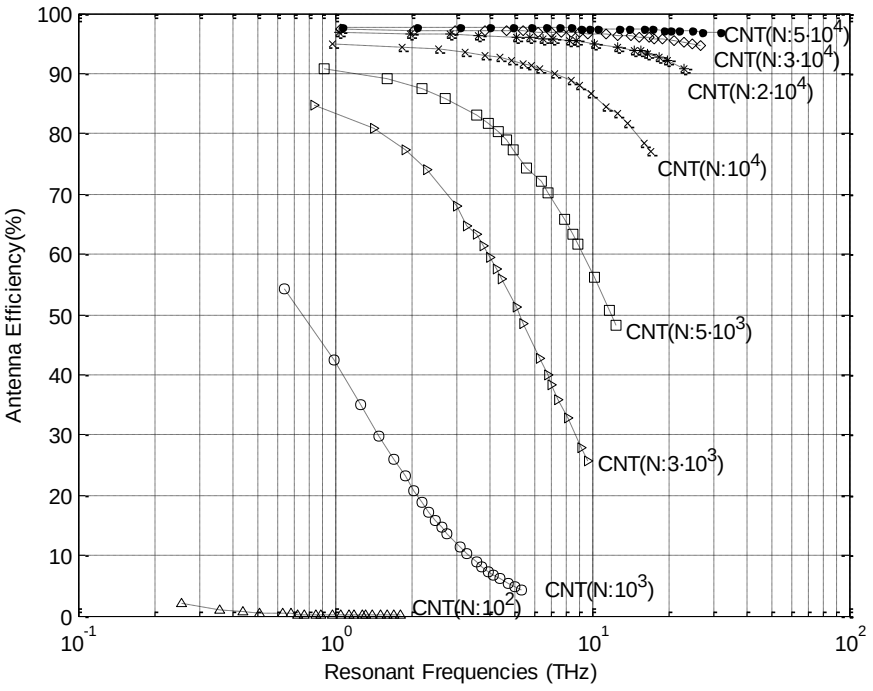

Figure 2.10: Antenna efficiency of strip antenna of BCNTs and thin gold film of BCNT densities of 10^2 to $5 \cdot 10^4$ [CNTs/μm].

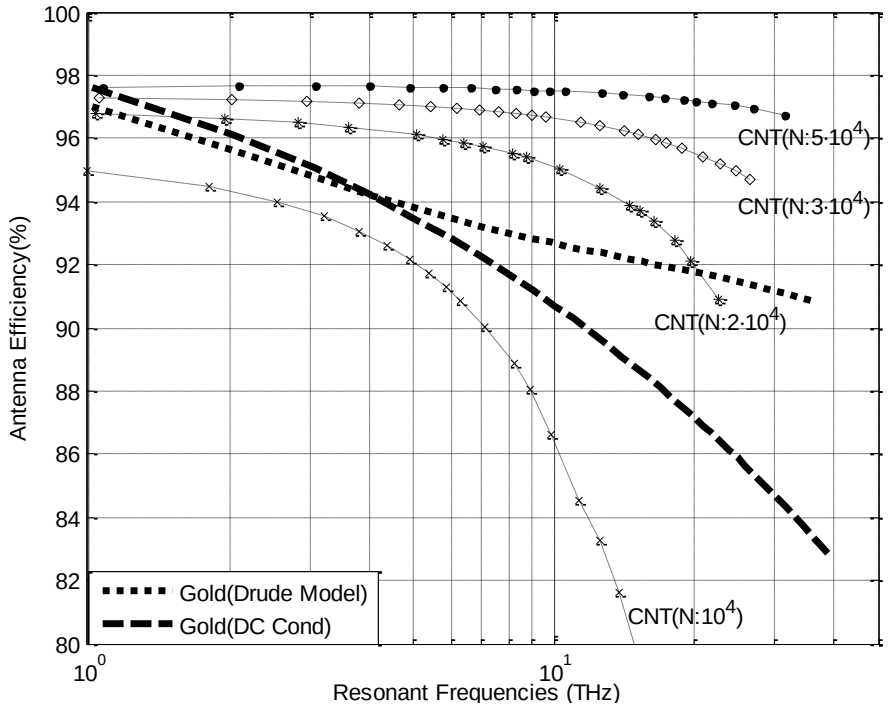

Figure 2.11: A magnified plot of antenna efficiencies for BCNT densities of 10^4 to $5 \cdot 10^4$ [CNTs/μm] and a comparison to efficiencies of thin gold antenna.

Fig. 2.10 and Fig 2.11 compare the antenna efficiency of BCNT and thin gold film antennas. In these calculations, the antenna efficiencies only account for power loss on the antenna material and ignore the mismatch loss. The MoM simulation indicates that the radiation efficiencies obtained by the calculation of the power loss and the far-field radiation power are consistent.

Fig. 2.10 and Fig 2.11 indicate that BCNT antennas with number density values equal or lower than 10^3 [CNTs/μm] do not demonstrate high radiation efficiency. Since the imaginary component of conductivity is greater than its real component at high THz frequencies, the thin gold film antenna whose conductivity is calculated using the Drude model shows a more gradual decrease in the efficiency than that calculated using the DC conductivity. This results in a lower surface resistance than that of DC gold. When the

number density is higher than 10^4 [CNTs/μm], antenna efficiencies of BCNT antennas are comparable to those of thin gold film antennas modeled by the Drude model. The number density of BCNT antenna should be approximately $2 \cdot 10^4$ [CNTs/μm] to surpass a thin gold film antenna. However, it is important to mention that thin gold film provides very high radiation efficiency up to tens of THz. It suggests that the increased efficiency of BCNTs with very high densities may not be worth the complicated fabrication processes needed to make BCNT antennas.

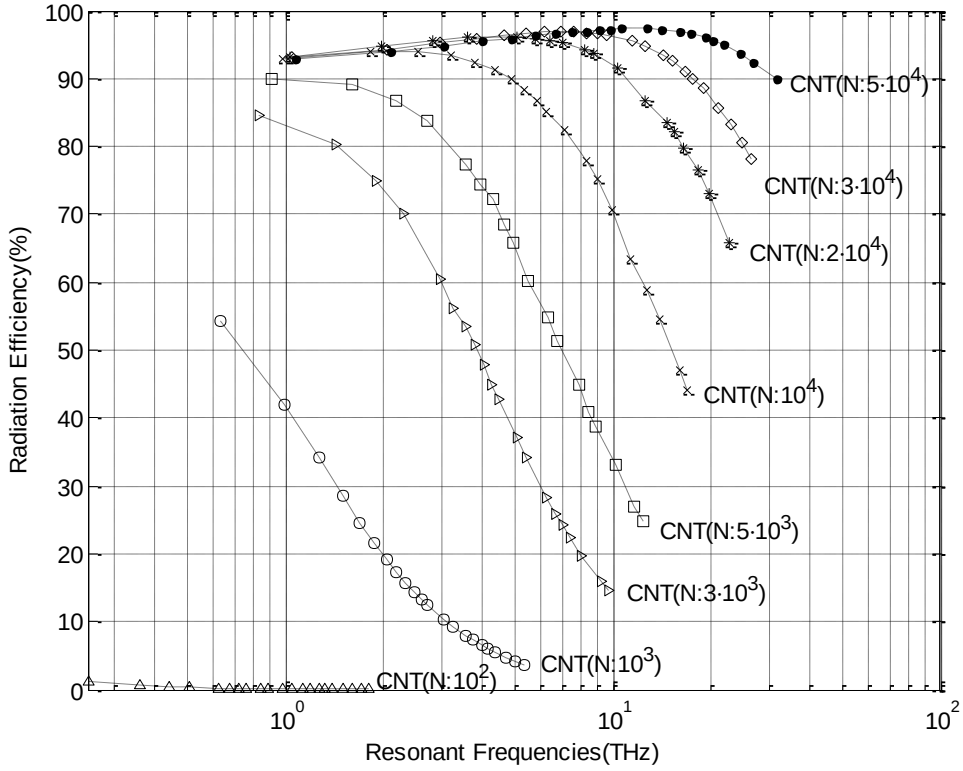

Figure 2.12: Radiation efficiency (including impedance mismatch power loss to a 50 Ω transmission line) of strip dipole antenna of BCNTs (N: CNTs/ μm) and thin gold film BCNT densities of 10^2 to $5 \cdot 10^4$ [CNTs/μm].

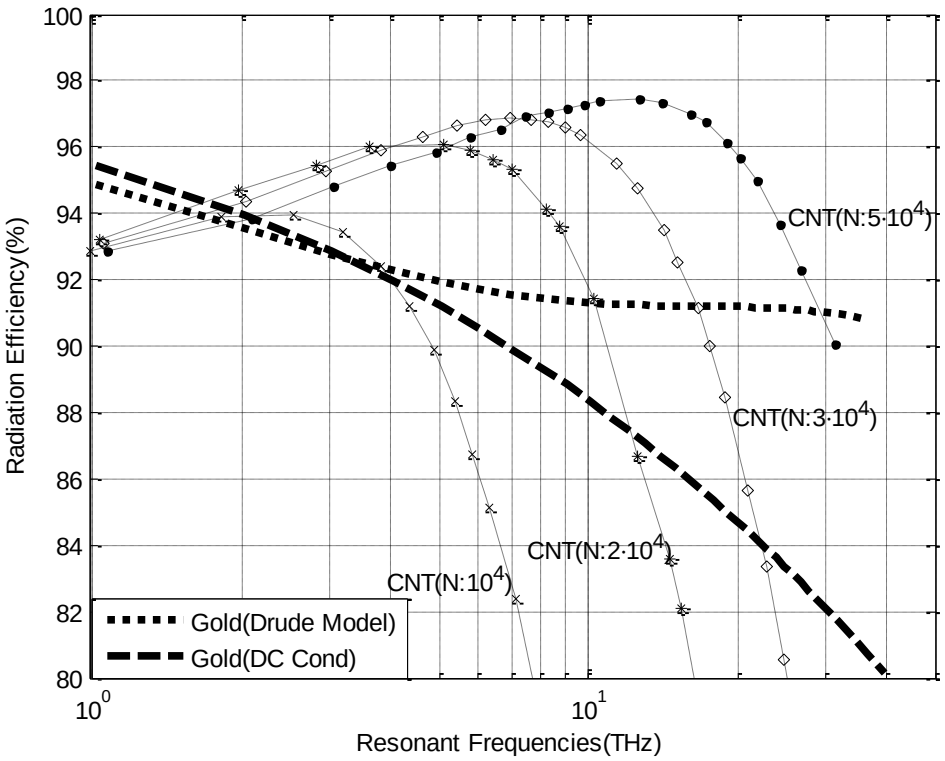

Figure 2.13: A magnified plot of BCNT densities of 10^4 to $5 \cdot 10^4$ [CNTs/μm] and a comparison to efficiencies of thin gold antenna.

The antenna efficiencies reported in Fig. 2.12 and Fig. 2.13 show the radiation efficiency including the mismatch (to 50 Ω transmission line) power loss. Matching networks are usually lossy and may be complicated to fabricate at high THz frequencies. To evaluate the performance of antennas without an external matching network, the impedance mismatch in the calculation of antenna efficiency must be considered. Fig. 2.12 and Fig. 2.13 show that when the number density (N) is higher than $2 \cdot 10^4$ [CNTs/μm], then the radiation efficiency of BCNT antennas outperforms thin gold film up to a certain frequency. For example, with number densities of $2 \cdot 10^4$, $3 \cdot 10^4$, and $5 \cdot 10^4$ [CNTs/μm], the radiation efficiency of BCNT antennas outperforms thin gold film at frequencies up to approximately 10 THz, 16 THz, and 30 THz, respectively. This behavior can be explained by the large mismatch due to the small input resistance of

BCNT antennas, which causes their radiation efficiency to be lower than the radiation efficiency of thin gold film antennas.

2.8 Conclusion

Utilizing the scalability of the equivalent circuit of SWNTs in its bundle structure, BCNTs are modeled electromagnetically by an anisotropic resistive sheet. The numerical simulation based on the MoM in conjunction with the resistive sheet model is used to assess the performance of the antennas. The results indicate that a BCNT antenna with a density of SWNTs less than 10^3 [CNTs/μm] has a very poor radiation efficiency. The fact that the equivalent number density of BCNT antenna should be greater than 10^4 [CNTs/μm] to achieve acceptable values of radiation efficiency suggests the necessity of fabricating much more densely aligned SWNTs. Thus, to be utilized as an effective antenna radiator in the THz frequency range, the density of BCNTs should be approximately three order of magnitude higher than the maximum density which the current fabrication technology can realize (10 [CNTs/μm]).

Chapter 3

Gold Bowtie Antenna Topology for High-Efficiency Thermophotovoltaics

Gold antenna which is featured by plasmonic effect at terahertz and optical frequencies is used to enhance the performance of optical devices, specifically, TPVs (Thermophotovoltaics), a traditional infrared (IR) energy absorbing device. A low bandgap semiconductor material, indium gallium arsenide antimonide (InGaAsSb) for conversion from IR waves to DC power is firstly chosen, and the operating band of the antenna is set near a frequency where the maximum quantum efficiency of InGaAsSb exists. Then a novel method to realize the maximum power transfer between the antenna to the InGaAsSb at the IR band is presented and an optimum antenna topology for TPV application is followed. Also a novel configuration of the bowtie antenna array is presented that allows for collection of DC currents through an almost arbitrary parallel or series configuration of TPV cells without adversely affecting the IR performance of the individual antennas. Before introducing the efficient gold antenna design for TPV devices, the introduction of TPV is followed firstly.

3.1 Thermophotovoltaics

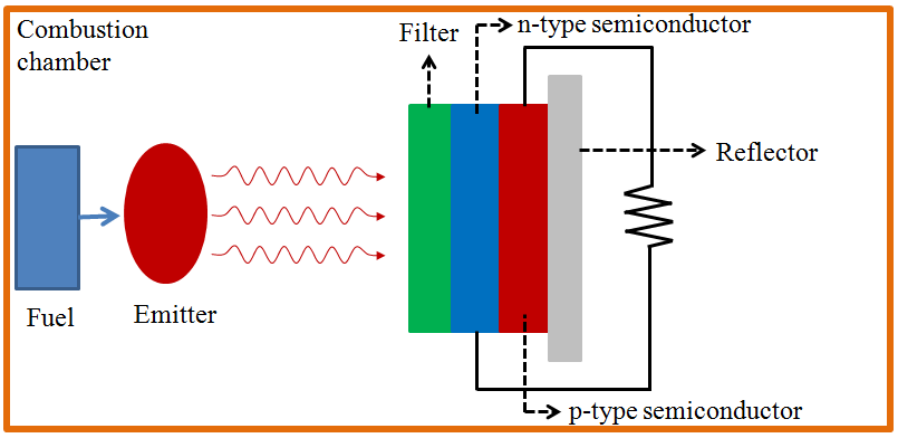

Figure 3.1: Thermophotovoltaic structure.

TPV is a semiconductor p-n junction device which converts IR signals to DC power [61]. Different from photovoltaics (PV) which absorb visible lights from solar energy, TPV requires a separate IR emitter. This emitter can be a hot temperature engine from a satellite or a built-in metallic IR-emitting structure heated by a fuel such as hydrogen gas. For the first case, a separate TPV can be located adjacent to the hot engine to function as an IR energy collector. The second case indicates a combustion chamber where the cell and the IR emitter reside together and it independently functions as an IR energy generation device as shown in Fig. 3.1. Such devices are envisioned as efficient and small-scale (cm^2-based) converters of chemical to electrical energy. Radiated energy from the emitter operating at a lower temperature of approximately 2000°C compared to 6000°C of PV falls into the near infrared (NIR) spectrum. Due to the emission of NIR signal from the emitter, the bandgap of the semiconductor should be lower than silicon in a PV system. The antimonide-based cells such as InGaAsSb or Gallium Arsenide (GaAs)

are shown to have low band-gap values (E_g = 0.35 ~ 0.7 eV) suitable for TPV cells [47]. This material is chosen for TPV material in the chapter.

In conventional TPV systems, the semiconductor layer should be thick, such as a few microns, to absorb IR power efficiently and the area of the semiconductor junction has to be a few cm^2 wide because the semiconductor has a low absorption coefficients in IR frequencies [62, 63]. Also a conventional TPV implements a filter structure between the emitter and the semiconductor p-n junction and a photonic crystal-based emitter. Both elements are designed to reduce the mismatch between the emission spectrum of emitter and the absorption spectrum of low bandgap semiconductor [64, 65, 66]. Recently, a compact mm-size TPV system where the photonic crystal emitter, InGaAsSb cells, and a maximum power point tracker are all integrated into a single device has recently been fabricated and shown to present a power conversion efficiency of ~ 2.2% and output power of 220 mW [62].

In this chapter, the use of a low bandgap semiconductor, InGaAsSb with a bandgap, E_g = 0.52 eV in conjunction with a resonant metallic antenna is presented in order to improve the performance of TPV cells maximally. Instead of a bulk semiconductor that is commonly used for IR energy conversion, the antenna mounted with a nanometer size low bandgap semiconductor load also has the potential to reduce a TPV system's volume and improve its efficiency due to the field enhancement at the terminals. However, such a low bandgap material at IR frequencies possesses low conductivity and high permittivity with significant frequency dispersion. This relevant high impedance of the load cannot easily be matched to traditional dipole antennas operating in its series resonance considered in microwave frequencies. As a result,

realizing a high impedance bowtie antenna for the matching with the high impedance of TPV semiconductor material at its absorption frequency band becomes a formidable challenge in the efficient IR or optical antenna design. For this process, a combination of the frequency dependent load size and the antenna structure is simultaneously optimized to achieve the impedance matching which means also the maximum power transfer. The antenna is designed to be operated at its anti-resonance mode, instead of the series resonance mode normally used in RF antennas. Also an extra transmission line stub has to be placed in parallel with the semiconductor load to compensate for the high capacitance of the load. This process provides a bowtie antenna topology connected with the stub as an optimum design. The bowtie topology is also favorable due to its higher intrinsic bandwidth. Another good feature is that the wide end of the bowtie can give a significant transition with wiring among antennas. When thin nano-wires connect the ends of adjacent bowties for collecting DC current, the characteristic impedance transition prevent the degradation of the individual IR antenna's performance.

To demonstrate the enhanced performance of the proposed TPV cells the power absorption efficiency of a bulk thick TPV cell is compared with that of an infinite array of metal-backed antennas loaded with the same material. Finally the design of an array of series/ parallel antenna TPV cells with DC interconnects among them for obtaining the required DC voltage and current is presented. With this design it is possible to fabricate a mm-size TPV array with an almost arbitrary voltage output (using approximately 10^6 optimized bowtie antenna cells) and a higher DC conversion efficiency than the bulk material.

3.2 Bowtie Nanoantenna Design

Lenses and reflectors are commonly used to increase the sensitivity of photodetectors or as concentrators for PV cells. These concentrators are bulky and cumbersome for integration with such devices. In addition, the spot size at the focal plane is diffraction limited. Considering the fact that resonant antennas present effective apertures that are commonly much larger than their physical aperture and that their ports at which the signal concentrates can be made much smaller than a wavelength, resonant antennas can be used to concentrate the IR energy into a very small area. InGaAsSb is shown to provide a low bandgap energy level of 0.52 eV which is suitable for photovoltaic and photoconducting applications in the NIR region. This band-gap energy level corresponds to energy of a photon at 130 THz. Hence such a material has a cut-off wavelength of 2.4 μm, i.e. the bulk material conductivity is expected to be very low at frequencies below 130 THz. The center of the band at which the material (InGaAsSb) assumes its maximum quantum efficiency occurs at approximately 1.67 μm which corresponds to 180 THz [67]. This center frequency will be used as the optimal resonant frequency for the antenna.

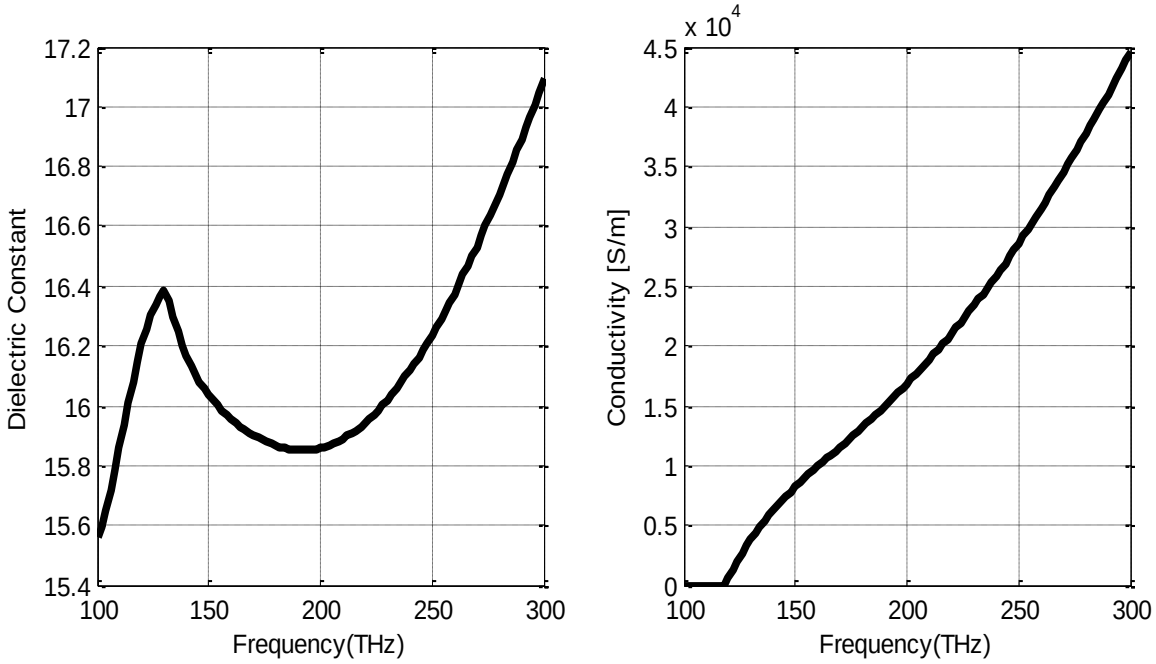

Figure 3.2: Dielectric constant and conductivity of InGaAsSb.

To calculate the equivalent impedance of InGaAsSb with a specific dimension as the antenna load, the constitutive parameters of InGaAsSb as a function of frequency are needed. The relative permittivity and conductivity of InGaAsSb from 100 THz to 300 THz is shown in Fig. 3.2 [68]. As shown the real part of the relative dielectric constant is approximately 16 and its variation with frequency (beyond the cut-off frequency) is rather gentle. However, the material conductivity (extracted from the imaginary part of the complex dielectric constant), which is proportional to absorption, is a strong function of frequency and assumes high values only after the cut-off frequency near 126 THz. At the desired frequency of 180 THz, the conductivity of InGaAsSb is ~ 1.5×10^4 [S/m] and the corresponding skin depth is 419 nm.

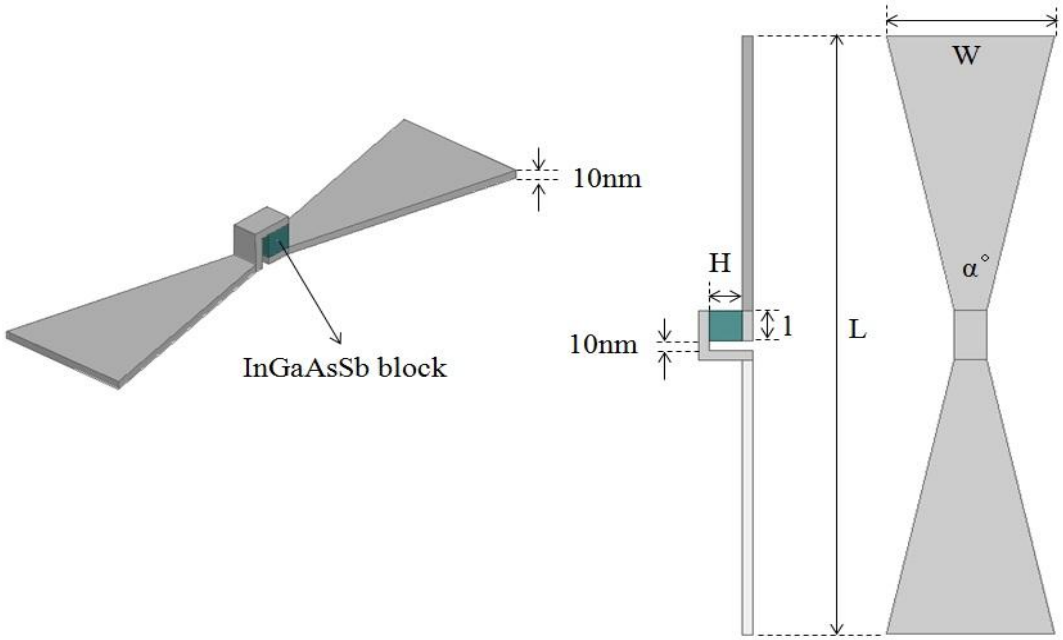

Figure 3.3: Bowtie antenna structure in one plane.

The proposed bowtie antenna structure is shown in Fig. 3.3. The integrated antenna load is placed in the middle between two small metallic electrodes. The equivalent circuit of InGaAsSb load can be represented by a conductance ($G_{InGaAsSb}$) and a susceptance ($B_{InGaAsSb}$) connected in parallel. Both parameters can simply be modeled by $G_{InGaAsSb} = \sigma_{InGaAsSb} \cdot A/H$ and $B_{InGaAsSb} = j\omega\varepsilon_0\varepsilon_{InGaAsSb} \cdot A/H$ where A is the area of the electrode and H is the separation between the two electrodes. The expected size of the antenna at 180 THz is on the order of hundreds of nanometers; hence the size of the load at the antenna port falls into tens of nanometer scale. This tiny InGaAsSb load shows high capacitance and resistance despite its relatively high conductivity. Both the center frequency and the equivalent impedance of the InGaAsSb load affect the bowtie antenna geometry.

Considering the fabrication constraints, the metallic wings of the bowtie antenna are patterned over a thin flat sheet on which a small block of InGaAsSb with appropriate

dimensions is grown. All metallic traces in the simulations are modeled by the Drude formula for conductors. Using gold, a plasma frequency of 2,080 THz and the scattering coefficient of 55×10^{12} [s^{-1}] are used in the Drude model [5]. The geometric parameters of the antenna are denoted as follows: the length of the bowtie antenna including its terminals is *L*, the end width of the bowtie antenna is represented by W, the angle of the bowtie antenna is α, the thickness of the gold is *T* (set to 10 nm), the height of the InGaAsSb load is *H*, and the length of the InGaAsSb load having a square cross section is *l*.

As mentioned before, the load resistance of a very thin InGaAsSb load is rather high due to the very small lateral dimensions of the load (comparable to the size of the bowtie antenna terminals). These high input impedance values cannot easily be matched to the traditional 73 Ω dipole antennas. Noting that linear antennas can present an anti-resonance behavior at a frequency slightly above the series resonance, the antenna length is chosen to be larger than λ/2. For this mode the input resistance of the antenna is very large (an order of kΩs). To match the input resistance of the antenna to the load resistance at the center frequency (180 THz), the angle of the bowtie antenna can be adjusted. This parameter also affects the antenna bandwidth. It is noted here that the higher the antenna input resistance, the smaller the bandwidth. Hence it is desirable to reduce the load resistance as much as possible. Since the material conductance is fixed, the value of this resistance is determined by the load length and height. The maximum length is limited by the maximum antenna terminal size and the minimum load height is limited by the material growth technique. Herein, the dimension of the load is fixed to 30 nm × 30 nm × 30 nm which is compatible with epitaxial growth fabrication process. To

design the structure, first the antenna should be designed and characterized without considering the effect of the load. This can be done by de-embedding the capacitance at the antenna terminals from the input impedance of the bowtie antenna where the load is placed [29]. This way the intrinsic input impedance of the bowtie antenna is calculated.

3.2.1 Maximum Power Transfer

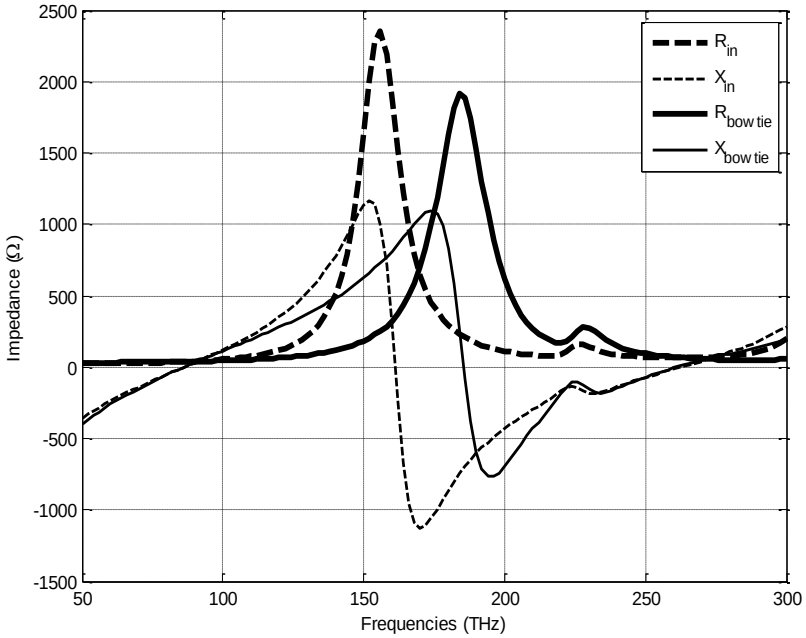

Figure 3.4: Input impedance of bowtie antenna loaded with an air gap(dashed line) and bowtie antenna intrinsic input impedance(solid line) with L = 605 nm, W = 160 nm, α = 30°, H = 30 nm, and l = 30 nm.

In Fig. 3.4, the parallel resonance (anti-resonance) behavior of the intrinsic input impedance of the bowtie antenna is shown. Here L is chosen to be 605 nm to achieve a center frequency of 180 THz. The rest of the dimensions are set as follows: W = 160 nm, α = 30°, and H = l = 30 nm. The solid line shows the intrinsic impedance of the bowtie antenna where the resistance at the parallel resonance is shown to be around 1.9 kΩ. This input resistance value is optimized by varying α, the bowtie antenna angle, and is

determined from the load dimension and material conductivity. It should also be mentioned that the parallel resonance of the bowtie antenna, where gold is modeled by Drude formula, shows a reasonable effective wavelength scaling due to the plasmonic effect of metals at IR bands and above. 605 nm-length PEC bowtie antenna would have its computed parallel resonance at ~ 264 THz, whereas the same antenna made with gold (using the Drude model) shows its parallel resonance at ~ 156 THz. This corresponds to a wavelength scaling factor of 1.69 ($\lambda_{eff} = \lambda/1.69$) which is a consistent with the phenomenon reported in [12].

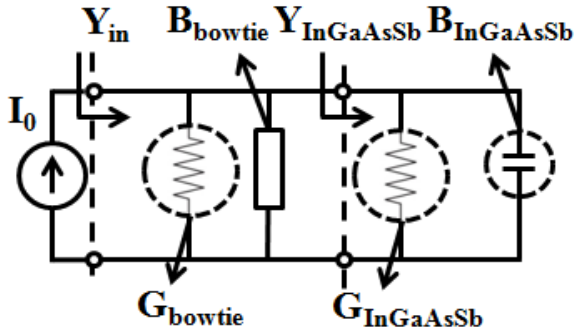

Figure 3.5: Equivalent circuit of the bowtie antenna loaded with InGaAsSb load in receiving mode.

For the maximum power transfer, G_{bowtie} is set equal to $G_{InGaAsSb}$ which is obtained from: $R_{bowtie} = H/(\sigma_{InGaAsSb} \cdot A)$. This value is 1.9 kΩ at 180 THz, using $\sigma_{InGaAsSb} = 1.5 \cdot 10^4$ [S/m], H = 30 nm, and l = ~ 30 nm. Though the high resistance of InGaAsSb load can be matched by the high input resistance of the parallel resonance mode of the bowtie nanoantenna, the capacitance of the InGaAsSb block has not been taken into consideration yet. The effect of the load capacitance can easily be studied using the equivalent circuit model of the bowtie antenna together with the InGaAsSb load (30 nm × 30 nm × 30 nm) as shown in Fig. 3.5.

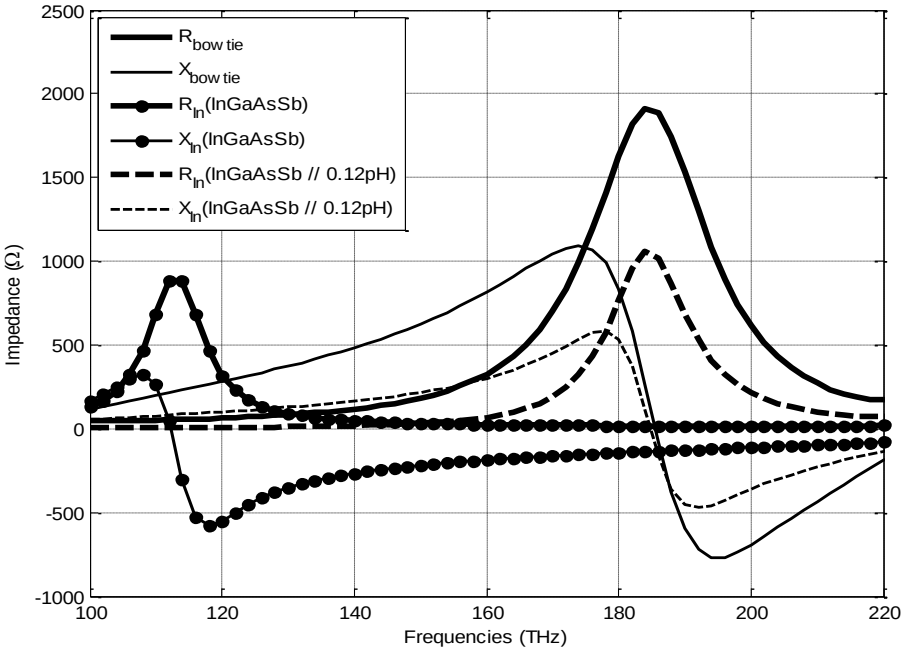

Figure 3.6: Input impedance of the bowtie antenna loaded with the InGaAsSb load (solid line with dots), and input impedance of the bowtie antenna loaded with the InGaAsSb load and a shunt ideal inductor having inductance of 0.12 pH (dashed line), and bowtie antenna intrinsic input impedance (solid line).

The load capacitance that appears in parallel with the parallel LC equivalent circuit of the antenna reduces the resonant frequency. This effect is shown in Fig. 3.6 (solid line with dots) where the input impedance of the bowtie antennas loaded with InGaAsSb load is plotted. The peak at resonance is shifted down to 115 THz. At this frequency the load resistance is significantly higher than the designed value of 1.9 KΩ due to its low conductivity. Also the antenna at the new resonant frequency shows significantly lower input resistance. These perturb the impedance matching and the maximum power transfer condition. To shift the parallel resonance back to 180 THz, the bowtie antenna length can be shortened to resonate at a much higher frequency than 180 THz so that the combined inductive reactance of the antenna can cancel out the capacitive reactance of the load at the desired frequency. However, as shown in Figure 3.6, the input

resistance at a frequency much lower than the resonance frequency is significantly lower than the input impedance of the antenna at the intrinsic resonance. In this case, the input resistance of the antenna shows a much lower resistance, 0.9 kΩ at 115 THz than 1.9 kΩ at 180 THz. For maximum power transfer at the lower resonance, a smaller load resistance (larger area or lower thickness) will be required. It should be noted that at lower frequencies the material conductivity is significantly reduced, and therefore the required load area does not scale with frequency. In addition, the larger load area will also increase the capacitance which in turn further reduces the resonant frequency. Thus matching at 180 THz, by simply varying the load dimensions, is impossible. Hence the antenna size scaling approach cannot satisfy the maximum power transfer condition for the parallel resonance mode at 180 THz. An alternative approach is proposed by introducing a reactive load as an additional parameter to facilitate the maximum power transfer for a load with prescribed dimensions. Basically, a shunt inductance to compensate for the capacitance of InGaAsSb load at 180 THz is introduced. To determine the value of the shunt inductive reactance, the accurate capacitance value of the load must be determined. Fringing effects of the InGaAsSb load (30 nm × 30 nm × 30 nm) are taken into account in a full-wave simulation. It is shown that an inductive load with an equivalent inductance of 0.12 pH is required. In Figure 3.6, the input impedance of the bowtie antenna loaded with the InGaAsSb load in parallel with an ideal inductor having an inductance value of 0.12 pH is also shown. As observed, the parallel resonance is shifted back to the desired frequency, 180 THz. Also the combined resistance value shown is almost half of the intrinsic antenna input resistance which indicates a perfect impedance match and the fulfillment of the maximum power transfer condition. To

implement this inductance for the bowtie antenna structure, an open-ended transmission line stub connected to the InGaAsSb load in shunt is proposed.

3.2.2 Open-ended Transmission Line Stub

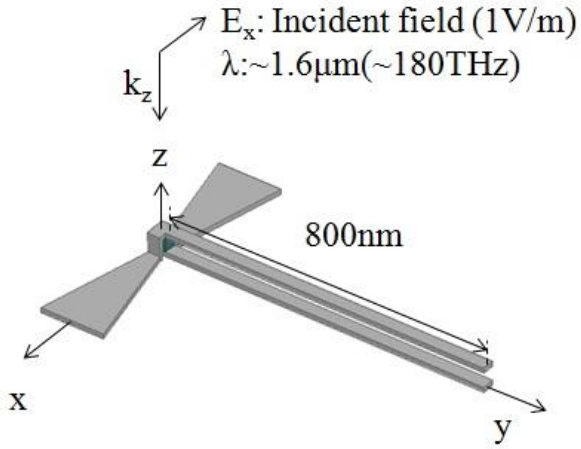

Figure 3.7: Open-ended transmission line connected in shunt with the InGaAsSb load.

In Fig. 3.7, an open-ended parallel strip transmission line is connected to the top and bottom of the load electrodes. An open-ended transmission line, instead of a short-circuited stub, is used to avoid short circuiting the DC voltage of the InGaAsSb p-n junction for TPV application. To estimate the length of the open-ended transmission line which realizes the required inductance, the effective wavelength at the center frequency should be determined.

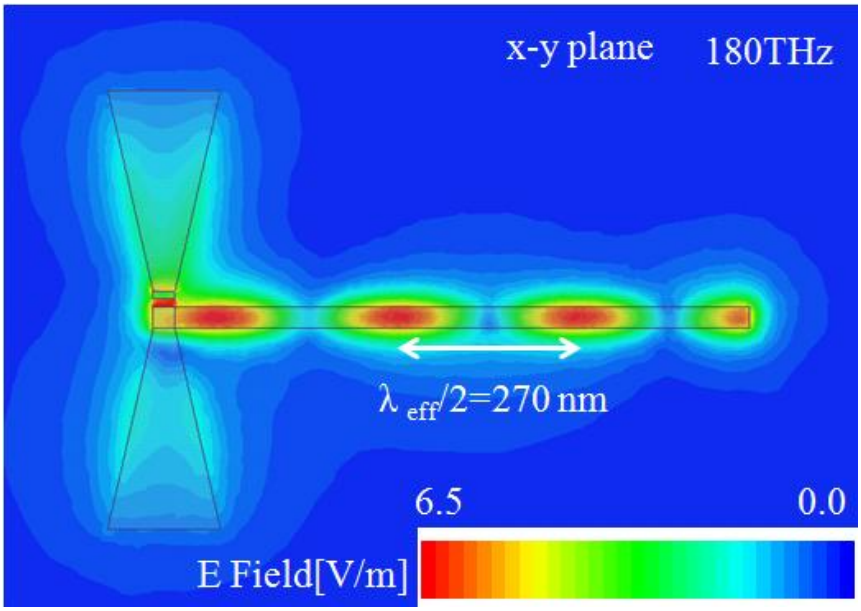

Figure 3.8: Magnitude of complex E field on a plane between the two strips of the transmission line for a plane wave illumination at 180 THz.

This is done by simulating the standing-wave pattern on a long open stub connected to the bowtie antenna that is illuminated by a co-polarized plane wave. The standing wave pattern on the line can be used to find the propagation constant or the effective wavelength of the line [69]. The simulation shown in Fig. 3.8 uses an 800 nm-long open-ended transmission line. As shown in this figure the peak to peak separation is about 270 nm, indicating the effective wavelength of 540 nm at 180 THz. To obtain an inductive reactance from the open-ended stub, its length should be larger than a quarter wavelength.

3.2.3 Field Enhancement at the terminals of the bowtie antenna

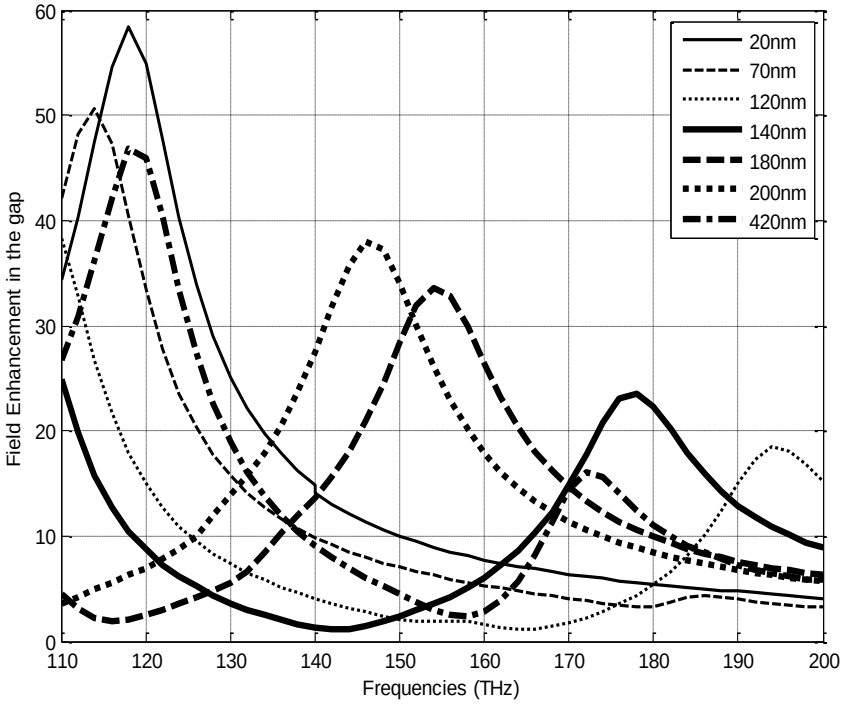

Figure 3.9: Field enhancement at the center of the InGaAsSb load versus the stub length as a function of frequency.

For an incident plane wave with field intensity of 1 V/m, the electric field intensity at the antenna terminals is plotted in Fig. 3.9. The field enhancement, the ratio between the electric field intensity at the antenna terminals and the incident electric field intensity is plotted versus the stub length as a function of frequency. A very short open stub with 20 nm shows a voltage peak near 115 THz which is expected as the uncompensated load capacitance lowers the resonance to ~ 115 THz. The load resistance is much higher than the resistance of the antenna which results in a higher gap voltage, nearly equal to open-circuit voltage. Also, as expected from the analysis of the open-ended transmission line, the bowtie antenna shunt with a 140 nm open stub (longer than the quarter wavelength in the parallel strip line) shows the peak at near 180 THz. For this stub length the field enhancement is approximately 23.5 which is almost half the field

enhancement value observed for the antenna with the shortest stub. The fact that the voltage at the terminals of a matched antenna is half of the open-circuit voltage demonstrates that two necessary conditions for the impedance matching between the load and the antenna are fulfilled. The first is that the antenna input resistance is almost equal to the resistance of the load at the desired resonant frequency 180 THz. The second is that the inductance of the 140 nm stub compensates for the load capacitance at 180 THz.

3.2.4 Absorption Efficiency

To examine the efficiency improvement of the tiny TPV cell at the terminals of the bowtie antenna compared to a bulk TPV cell, the absorption efficiency is simulated. An infinite slab of bulk InGaAsSb is compared with an infinite array of bowtie antennas loaded with the InGaAsSb load (30 nm × 30 nm × 30 nm).

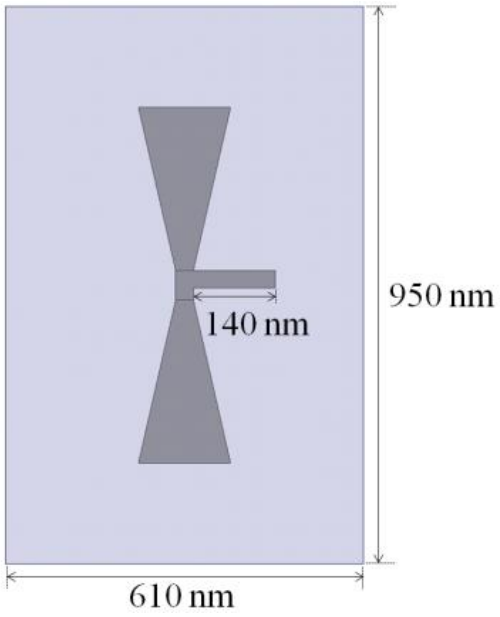

Figure 3.10: Unit cell (950 nm × 610 nm) of the bowtie antenna for infinite array.

These simulations are carried out using the periodic boundary condition for a unit cell (950 nm × 610 nm) using a FEM full-wave simulation tool as shown in Fig. 3. 10. In

this simulation the area of the unit cell is set to be the effective area of the bowtie antenna and the samples are illuminated by a vertically polarized plane wave at a normal incidence. The field enhancement for the infinite array of the antennas is shown as 23.5 which is identical to the value of a single antenna case. This fact physically shows that the unit cell size corresponds to the effective area of the bowtie antenna. The percentage of the absorbed power is calculated for each case and plotted as an absorption efficiency. Note that the DC power generation is directly proportional to the absorbed power by the semiconductor.

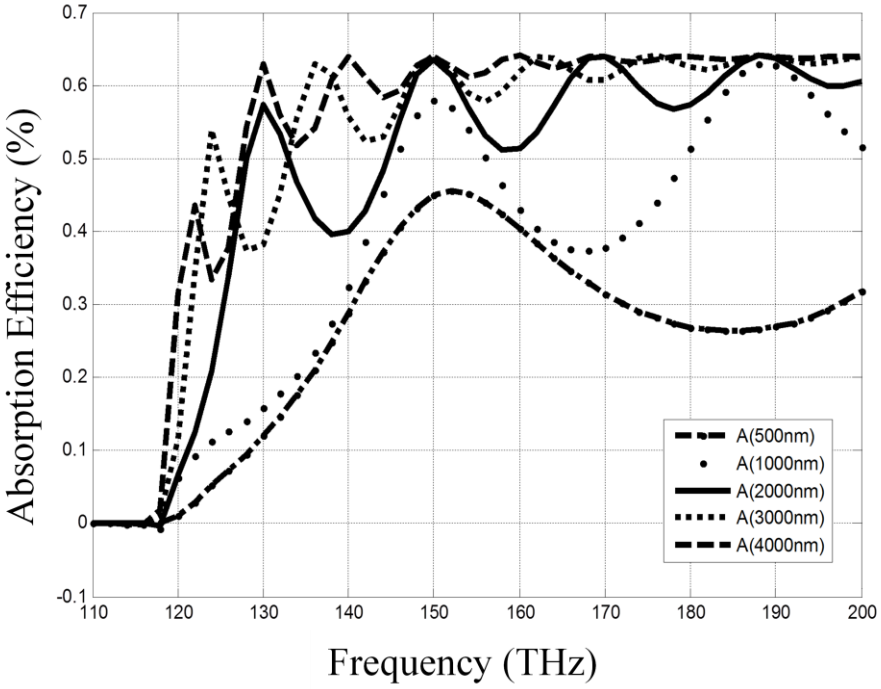

Figure 3.11: Absorption efficiency of InGaAsSb slab as a function of the slab thicknesses from 500 nm to 4000 nm.

In Fig. 3.11, the absorption efficiency of a 2 ~ 3 micron-thick InGaAsSb block is shown to saturate at around 65%. This is mainly due to the impedance mismatch between air and the slab of InGaAsSb. The thickness of the dielectric layer is chosen to be larger

than multiple skin depths and hence it practically can be viewed as a semi-infinite lossy dielectric medium.

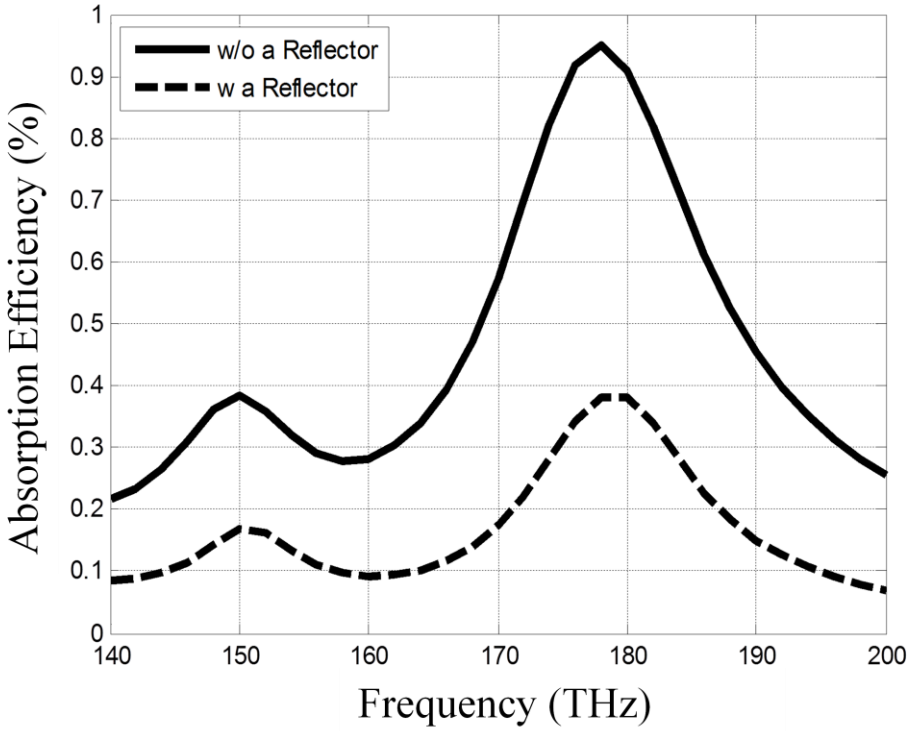

Figure 3.12: Absorption efficiency of bowtie antenna loaded InGaAsSb block (30 nm × 30 nm × 30 nm) with and without a back metallic reflector.

The simulation results for the absorption efficiency of the infinite array of bowtie antennas are shown in Fig. 3.12. Here an absorption efficiency of only 38% at the resonance is shown. This level is low due to that the antennas scatter significant amounts of energy in the forward direction. For a fair comparison with the semi-infinite InGaAsSb layer, the forward-scattered energy must be redirected back to the array. By placing a metallic reflector located at a quarter-wave behind the array the forward scattered wave can also be captured by the antenna array. The absorption efficiency of the array with the metallic reflector behind the array is also shown in Fig. 3.12 where ~ 95% absorption

efficiency is demonstrated. The higher absorption efficiency of the antenna array verifies that high efficiency of the antenna and the maximum power transfer between the load and the antenna. Also lower material usage and flexible implementation using the antenna design provides additional advantages to be used for a compact TPV system. Also in a TPV system, a finite number of antennas can be arranged to obtain a desired voltage or current outputs.

3.2.5 Radiation Efficiency

In this section the radiation efficiency of the antenna is present to examine the ratio of power loss in the metallic traces of the antenna to the power absorbed in the InGaAsSb load. The radiation efficiency of the bowtie antenna is computed as the ratio of total power radiated to the power delivered to the antenna terminals. It is found that the radiation efficiency of the antenna made from 10 nm-thick gold is about 70% at its parallel resonance. It is also interesting to note that the radiation efficiency of the bowtie antenna at its series resonance (the first resonance) is merely about 30%. This is another reason for operating the antenna at its parallel resonant mode. To increase the efficiency of the antenna, the thickness of the gold traces can be increased. Increasing the metal thickness leads to a slightly lower wavelength scaling factor or equivalently longer bowtie for resonance at 180 THz. This also leads to a lower input impedance for which the load size must be adjusted. Two additional simulations for metal thickness values of 15 nm and 20 nm are carried out. The antenna with 15 nm metal thickness shows an improved radiation efficiency of 75% and efficiency of the antenna with 20 nm metal thickness reaches up to 80% efficiency. Both are at the parallel resonance (~ 180 THz).

3.3 Array Design

As mentioned before, a bowtie antenna loaded with InGaAsSb can be considered as a tiny block of a TPV system which can be configured to generate a desired DC current or voltage. The value of the DC current and/or voltage can be controlled by properly making series and/or parallel connections of the cells. The length of the connecting traces in series or parallel should be in such a way as not to perturb the IR performance of the adjacent antennas. A narrow metallic trace is used to connect the two ends of adjacent bowtie antennas in the middle of the base of the metallic triangle where the current distribution is null at the resonance. The optimization of the length of the connecting traces is guided by inspecting the standing wave pattern along the trace. Choosing a proper length creates a current standing wave pattern with minima at the end of all bowtie antennas in the array. It should be noted that the field enhancement value at the terminals of an antenna component in this array is the same value (~ 23.5) as that of an isolated antenna.

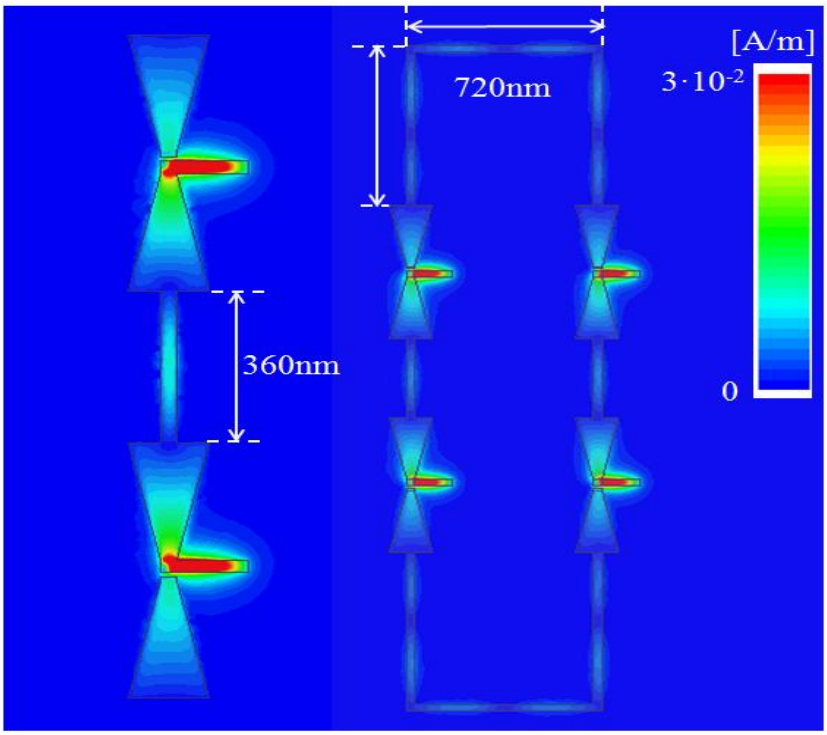

Figure 3.13: The series and its parallel array configuration of the bowtie antennas and the field distribution calculated from the tangential H field on the gold surfaces.

In the configuration shown in Fig. 3.13, the optimized length of the gold trace between the antennas in series is found to be around 360 nm. This length supports a current standing wave distribution over the antennas that is identical to the current distribution of an isolated antenna. The length of the connecting trace for parallel configuration is set to be 720 nm at each vertical and horizontal side. Again the lengths of these traces are chosen to support a standing wave to maintain a null current at the end of the bowties. We also chose the segment lengths to set a null current at the bends to minimize their radiation, and set the desired horizontal separation between the adjacent series elements. The number of connected TPV cells in series and parallel can be chosen in order to satisfy the required DC voltage and current from the TPV panel.

3.4 Conclusion

A bowtie antenna loaded with a nanometer-size (30 nm × 30 nm × 30 nm) low bandgap InGaAsSb block is designed for the maximum power transfer between the antenna and the load. This efficient antenna integrated with the thin semiconductor load can be used for an efficient and flexible TPV cell. The frequency dependent high impedance of the semiconductor load at IR frequencies is matched to the input impedance of the bowtie antenna. To achieve the input impedance match at the desired frequency, the bowtie antenna is designed to operate at its anti-resonance mode where a high input resistance can be achieved. The nanometer-size load dimensions are adjusted to match the input resistance and the high capacitance of the load is compensated by a shunt open transmission line stub. The dimensions of the antenna, the load, and the inductive open stub are optimized for maximum power transfer at the desired band near 180 THz where the quantum efficiency of the semiconductor is maximum.

At the desired band, the optimized antenna loaded with an InGaAsSb block shows a field enhancement on the order of ~ 23.5 (27.4 dB) at its terminals. Also, the absorption efficiency of an infinite array of the optimized bowtie antennas, backed by a metallic reflector located at a quarter-wave behind the array, is ~ 95% which is 50% higher than the absorption efficiency of a thick layer of the bulk InGaAsSb. In addition the design of series and parallel array configurations for achieving the desired DC voltage and current output is considered. Antenna elements are connected by resonant segments of metallic traces at the base of the adjacent bowtie antennas to form different connection configurations without adversely affecting the IR performance of the antenna elements.

In practice, a dense array (~ 10^6 antenna elements) of tiny bowtie antenna loaded with InGaAsSb TPV cell can be integrated into a mm-sized TPV system. Also a thin flexible/conformal implementation of such an IR photovoltaic conversion unit can be used for power scavenging from heat sources; for example, from electronic circuits or spacecraft thrusters for deep space missions.

Chapter 4

Gold Bowtie Antenna Topology

for Uncooled Infrared Detector with Enhanced Sensitivity

In this chapter the same topology of gold bowtie antenna which is operated at its anti-parallel resonance and loaded with a small low-bandgap (E_g = 0.52 eV) indium gallium arsenide antimonide (InGaAsSb) p-n junction is utilized and its application for a highly sensitive IR detector is studied. The sensitivity improvement of a proposed IR detector using the antenna is evaluated against the traditional bulk detector. The effective area of the bowtie antenna and the field enhancement at the terminals of the antenna are used for analyzing the sensitivity improvement.

4.1 Introduction

Traditional IR detector utilizes anti-reflection coating to eliminate impedance mismatch between the air and the high index semiconductor material [70]. This enhances the absorption and provide some limited improvement in the signal-to-noise. It is well known that the performance of conventional infrared detectors is limited by the absorption coefficient of the active semiconductor material and that the performance is improved if thicker layer of the semiconductor is used for materials with low absorption

coefficients [63]. To increase the signal-to-noise ratio or sensitivity, antenna-coupled detectors where the antenna is mounted at the boundary between the surrounding media and the active material have been studied [14, 34, 71, 72]. The antenna utilizing the surface plasmonic effect of the metals at optical frequencies, collects the incoming signal into a small volume of the active material [14]. The enhanced field confined near the antenna terminals can reduce the required thickness of the active area. This reduction of the active region lowers the dark current which in turn increases the signal-to-noise ratio of the detector. The enhanced sensitivity can be attributed to the effective area of the antenna which is much larger than the physical area of the antenna and the area of coupled field concentration [72]. A recent study related to the antenna-mounted detector using metal-oxide-metal diodes has been predicted to give Noise Equivalent Power (NEP) of 1.53 nW and Detectivity (D*) of about 2.15×10^6 cm $Hz^{1/2}$ W^{-1} [72]. Also an experimental study of the antenna-mounted detector operating in room temperature and zero bias is reported in [73, 74] where it has been reported that the device can provide SNR of 626, NEP of 4.11 nW, and D* of 1.91×10^5 cm $Hz^{1/2}$ W^{-1}. It has also been shown that the noise from the structure is mainly due to Johnson noise. These devices were not optimized for maximum power transfer from the load to the antenna through impedance matching mainly due to the fact that the load impedance of such materials with low absorption efficiency is very high. It is noted that the detectivity and SNR can be improved significantly if the antenna could be matched to the detector at its terminals. Another issue with antenna-mounted detectors is the difficulty associated with signal pick up in such a way not to disturb the antenna performance. As a method to solve the problem, a focal planar array of the bowtie antennas can be built and metallic connections

among the antennas can be engineered. This focal planar array of the antenna load with InGaAsSb block can realize a sensitive uncooled near-IR detector. Additionally polarization dependence of the antenna can equip the traditional IR detector with polarization sensitivity feature [72]. By connecting different polarized antennas in an IR detector system, an IR polarimetric system also can be realized.

In this section, a resonant bowtie antenna match-loaded with a low bandgap semiconductor (InGaAsSb with a bandgap, E_g = 0.52 eV) at its anti-parallel resonance is also considered. Different from referenced works, [73, 74], the realization of the maximum power transfer through the optimized bowtie antenna using InGaAsSb material could result in the maximized sensitivity improvement for the near-IR detector. The detectivity of the IR detector which generally indicates its sensitivity is formulated. The affecting parameters are the field enhancement and the absorption cross section of the bowtie antenna loaded with InGaAsSb. The detectivity enhancement of the IR detector using the bowtie antenna versus the bulk semiconductor IR detector is quantized for general two cases of IR detectors: Johnson noise-limited detector and photon noise-limited detector.

4.2 Bowtie Antenna Integrated with InGaAsSb Block

Considering the fact that resonant antennas present an effective area that is commonly much larger than their physical area and that they can concentrate the collected power at a small area around their terminals, resonant antennas are ideal for enhancing the detectivity of uncooled IR detectors. The same bowtie-shaped antenna topology loaded with InGaAsSb is utilized for the IR detector application. The field

enhancement and the corresponding sensitivity enhancement of the antenna occurs at 180 THz where the maximum quantum efficiency of InGaAsSb is shown.

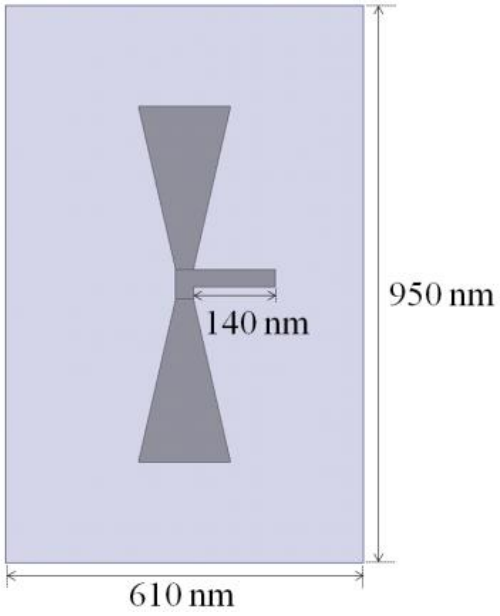

Figure 4.1: Unit cell (950 nm × 610 nm) of the bowtie antenna for infinite array of IR detector.

To compare the performance of the antenna loaded IR detector with the conventional detectors, an infinite periodic array of the antenna loaded IR detectors is examined against an infinite slab of the conventional detectors. The effective area of an antenna in isolation is chosen as the area of the unit cell of the array which is equal to the case of TPV, 950 nm × 610 nm. The same geometric setup for the periodic boundary as shown in Fig. 4.1 is applied and this infinite array of the antenna also shows 23.5 of the field enhancement on the InGaAsSb at 180 THz. This value of the field enhancement is directly related to the sensitivity enhancement of IR detector in the following section.

4.3 Sensitivity Comparison between Antenna-Loaded and Conventional IR Detectors

The analysis is aimed at determining the advantages of the nanometer size InGaAsSb p-n junction block mounted at the terminals of the bowtie antenna over the traditional IR photo-detector made from the same material. The expected sensitivity enhancement pertains to the following three major factors: 1) field enhancement at the terminals of the bowtie antenna (> 20), 2) the reduced surface area of the InGaAsSb p-n junction, and 3) the antenna ability of maximum power transfer.

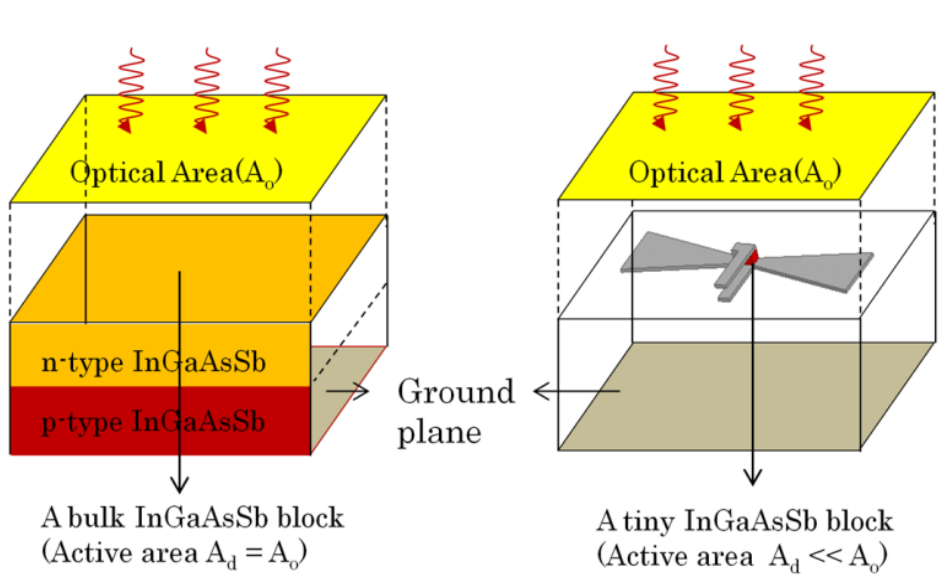

Figure 4.2: Optical area and detector area for a bulk InGaAsSb detector and an antenna loaded IR detector.

Fig. 4.2 illustrates a simple schematic of a traditional p-n junction InGaAsSb IR-detector (with relatively large surface area ~ 40 μm × 40 μm) and the proposed loaded tiny block (30 nm × 30 nm) of InGaAsSb photodiode on a bowtie antenna. For comparison, the optical area (A_o) of the traditional IR detector, defined as the physical

area where the bulk photodetector is exposed to near IR radiation, is chosen to be equal to the antenna effective area. Note that the simulation uses the periodic boundary conditions and thus the results are valid for much larger surface area. The active area of the semiconductor (A_d) for the nanoantenna photodetector is merely 30 nm × 30 nm. The impedance matched resonant bowtie antenna generates a field enhancement of the order of approximately 23.5 in the InGaAsSb block which in turn increases the gain of photon generation. At the same time the smaller active area of the photo-detector generates less noise current and therefore it is expected that the detectivity of the proposed photo-detector be significantly improved. Other advantages include design of detector arrays on flexible membranes, high resolution focal plane array design (close to diffraction limit), polarimetric sensing, ease of signal pickup, and ease of grouping elements in series or parallel configuration.

Here we examine the signal-to-noise ratio (SNR) advantage due to the field enhancement and the size reduction of the active area of the InGaAsSb diode attached to the bowtie antenna. In the example the ratio of A_o/A_d is almost 644 where A_o is the effective area of the antenna modeled by a rectangle with dimensions 950 nm × 610 nm and is A_d is 30 nm × 30 nm. The noise current of traditional photodetectors depends on the dark current $i_D = i_{sat}\,(e^{qV/kT} - 1)$ and the photo-generated current $i_p = q\eta(\Phi_{sig}+\Phi_b)A_d$. Here i_{sat} is the reverse saturation current which scales with the area of the detector A_d, q is the charge of an electron, K is Boltzmann constant, and T is the temperature in Kelvin. Also η is the quantum efficiency (including the reflectance of the detector). The photon flux density incident on the photodetector has unit of photons/(cm^2·s). Φ_{sig} and Φ_b are respectively the photon flux densities from the signal and

the background sources. By using the dark resistance of the diode at zero bias voltage, given by

$$R = \left(\frac{\partial i_D}{\partial V}\right)^{-1}_{V=0} = \frac{kT}{q i_{sat}} \tag{4.1}$$

the reverse saturation current is found to be $i_{sat} = kT/qR$. The noise current generated in the photodetector can be computed from [46]

$$i_N = \sqrt{2q(i_D + 2i_{sat} + i_p)\Delta f} \tag{4.2}$$

where i_D, i_{sat}, and i_p represent, respectively, the contribution of the shot noise, the Johnson noise, and the photon noise. Using expressions for the dark current, the reverse saturation current, and the photo-generated current, the noise current is explicitly represented by

$$i_N = \sqrt{2q\left[\frac{kT}{qR}\, e^{\frac{qV}{kT}} + \frac{kT}{qR} + q\eta(\Phi_{sig}+\Phi_b)A_d\right]\Delta f} \tag{4.3}$$

where Δf is the detector bandwidth. When Johnson noise is dominant, the detector is considered as Johnson noise-limited detector and when the photon noise is dominant, the detector is considered as the photon noise-limited detector. Thus for conditions where $\Phi_{sig} \ll \Phi_b$ and under zero bias voltage (V = 0) we have

$$i_N = \sqrt{\left[4\, \frac{kT}{R} + 2q^2\eta\Phi_b A_d\right]\Delta f} \tag{4.4}$$

The first term is the well-known Johnson noise current. Note that this includes the shot noise corresponding to zero bias voltage. The sensitivity of traditional photo-detectors for this Johnson noise-limited case will be detailed.

4.3.1 Johnson noise-limited case

When Johnson noise is the dominant factor in detector's noise current, SNR can be obtained from

$$\frac{i_{sig}}{i_N} = \frac{q\eta\Phi_{sig}A_d}{\sqrt{4\frac{kT}{R}\Delta f}} \tag{4.5}$$

The kT/R term is proportional to the reverse saturation current which scales with the detector area (since R is inversely proportional to A_d). Thus SNR scales with the square root of the detector area which is equal to the physical area for the traditional detectors. Noise Equivalent Power (NEP) is defined as the signal power ($hc/\lambda \cdot \Phi_{sig} \cdot A_d$) equal to the noise power corresponding to SNR of 1 and is given by

$$NEP = \frac{1}{q\eta}\sqrt{4\,\frac{kT\Delta f}{R}}\left(\frac{hc}{\lambda}\right) \tag{4.6}$$

Hence NEP scales with the square root of the detector area since R is inversely proportional to A_d which is equal to A_o. A figure of merit called Detectivity (D*) is often used to compare different photo-detectors. This quantity is defined in such a way to normalize the sensitivity (1/NEP) to a 1-cm^2 area and 1-Hz detector bandwidth with a unit of cm Hz$^{1/2}$ W^{-1} [46]. Hence the detectivity for Johnson noise limited case can be computed from

$$D^* = \frac{\sqrt{A_o\Delta f}}{NEP} = q\eta\sqrt{\frac{A_oR}{4kT}}\left(\frac{\lambda}{hc}\right) \tag{4.7}$$

Since the detectivity is area independent, the sensitivity of the conventional photo-detectors cannot be enhanced by changing the detector area. Considering the field enhancement at the terminals of the antenna and noting that photon flux density is proportional to the square of the field intensity, the photon flux density on the small photo-detector is $\Phi'_{sig} = \Phi_{sig} \cdot g^2$ where g is the antenna field enhancement factor. This equation assumes all photons captured by the effective area of the antenna are delivered

to the antenna terminals. Surely even under impedance matching condition, a percentage of the photons are scattered similar to the reflection of the photons from the bulk material. Placing a reflector behind the antenna array at a distance equal to the odd integer multiple of λ/4 reflects the forward scattered field and the array will absorb that component as well. The calculation shows that the matched antenna array can absorb 95% if the incident energy of which 25% is lost in metallic traces. Hence the overall power absorption is slightly higher than 70%. Absorption efficiency of thick layer of InGaAsSb at normal incidence is close to 60%. Thus we assume the scattered photons are accounted for in the quantum efficiency and that the quantum efficiency for both cases are approximately the same. As a result SNR of the detector within the bowtie antenna can be evaluated from

$$\frac{i_{sig}}{i_N} = \frac{q\eta\Phi_{sig} g^2 A_d}{\sqrt{4\frac{kT}{R'}\Delta f}} \tag{4.8}$$

where R' is the dark resistance of the diode at the antenna terminals which is inversely proportional to A_d. SNR is proportional to the square of the antenna field enhancement factor. In this case, it is noted that the incident energy is captured by the effective area of the array (A_o) and the calculation of NEP and D* is shown as

$$NEP' = \frac{1}{q\eta g^2}\sqrt{4\,\frac{kT\Delta f}{R'}}\,\frac{hc}{\lambda}\frac{A_o}{A_d} \tag{4.9}$$

$$D'^{*} = \frac{\sqrt{A_o \Delta f}}{NEP'} = q\eta g^2\sqrt{\frac{A_o R'}{4kT}}\,\frac{\lambda}{hc}\left(\frac{A_d}{A_o}\right) \tag{4.10}$$

Comparing (4.10) and (4.7), and noting that R'/R = A_o/A_d, it becomes clear that the detectivity of photo-diode embedded in the antenna is improved by $g^2\sqrt{A_d/A_d}$. For the bowtie antenna considered here, with g = 23 and $\sqrt{A_d/A_d}$ = 1/25.38, the detectivity

can be improved by a factor of 20.85 which is almost similar to the field enhancement factor. From this analysis, Johnson noise-limited detector has a quite significant improvement of detectivity by implementing the antenna structure. It is noted that the antenna structure implements a much smaller semiconductor material compared to the bulky p-n junction semiconductor of the traditional IR detector.

4.3.2 Photon noise-limited case

In this case, the photon noise is the dominant factor in the noise current. Thus equation (4.4) reduces to

$$i_N = \sqrt{2q^2\eta\Phi_b A_0 \Delta f} \tag{4.11}$$

The following SNR can be shown as

$$\frac{i_{sig}}{i_N} = \frac{q\eta\Phi_{sig}A_0}{\sqrt{2q^2\eta\Phi_b A_0\Delta f}} = \frac{\sqrt{\eta}\Phi_{sig}\sqrt{A_0}}{\sqrt{2\Phi_b\Delta f}} \tag{4.12}$$

SNR for this case also scales with the square root of the detector area which is equal to the physical area for the traditional detectors. NEP and the detectivity of the conventional photodetector for photon noise-limited case are as follows:

$$NEP = \sqrt{\frac{2\Phi_b\Delta f}{\eta}}\left(\frac{hc}{\lambda}\right)\sqrt{A_0} \tag{4.13}$$

$$D^* = \sqrt{\frac{\eta}{2\Phi_b}}\frac{\lambda}{hc} \tag{4.14}$$

(4.13) and (4.14) shows that NEP scales with the square root of the detector area and detectivity is independent of the detector area.

For the photon-noise-limited case, SNR of the bowtie antenna photo detector can also be computed easily and is given by

$$\frac{i_{sig}}{i_N} = \frac{q\eta\Phi_{sig}A_d g^2}{\sqrt{2q^2\eta\Phi_b A_d g^2 \Delta f}} = \frac{\sqrt{\eta A_d}\Phi_{sig} g}{\sqrt{2\Phi_b \Delta f}} \tag{4.15}$$

Because the noise is also amplified by the enhancement factor of the bowtie antenna, the SNR is linearly proportional to g, the antenna field enhancement factor. From which the expressions for NEP and D* are obtained as:

$$NEP' = \sqrt{\frac{2\Phi_b \Delta f}{\eta A_d}} \frac{hc}{\lambda g} A_0 \tag{4.16}$$

$$D'^* = \sqrt{\frac{\eta}{2\Phi_b}} \frac{\lambda}{hc} \sqrt{\frac{A_d}{A_0}}\, g \tag{4.17}$$

Comparing (4.14) with (4.17) the improvement in the detectivity of photon noise-limited case is represented by $g\sqrt{\frac{A_d}{A_0}}$ which approximately unity. This is due to the fact that the source of the noise and signal are similar and the antenna cannot differentiate them.

4.4 Focal Plane Array Design

As demonstrated, near IR detectors with substantially improved detectivity can be designed over a very small area (950 nm × 610 nm) and therefore in principle very high resolution focal plane array uncooled IR imagers can be realized. For most practical applications the pixel area is on the order of tens of microns where a large number of bowtie antennas can be accommodated. Bowtie antennas within each pixel can be connected in series, parallel, or combination to adjust the desired output voltage and current configuration. The chosen antenna configuration allows for such arrangements.

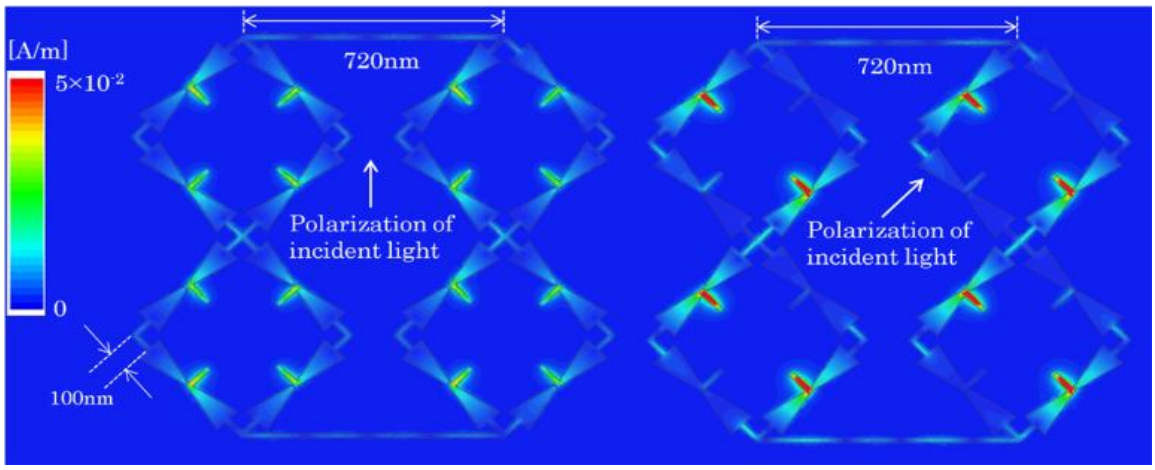

Figure 4.3: 45°-titled array configuration of bowtie antennas illuminated with a vertical and 45°-titled polarizations and the resulting current distributions (calculated from the tangential H field on the gold surface).

In Fig. 4.3, thin traces of gold to connect the bowtie's ends accomplish this, but the length of the thin traces must be adjusted in such a way as not to disturb the current distribution on the antenna itself. If the length of the wires connecting antennas are integer multiple of half the wavelength, the supported standing-wave current distribution will support the original current distribution of isolated antenna. The connecting trace between each bowtie antenna is set to 100 nm which preserves the required current distribution on the antennas in each square ring. Also the length of the horizontal trace which connects two adjacent 45°-tilted bowtie antenna square rings is set to 720 nm. The current distribution in this case maintains a null at the bowtie end and a maximum at the antenna terminals. Numerical simulations show the length of the line between two successive nulls in a straight section is 720 nm and for a 90° bend is 100 nm. To demonstrate this, we consider a pixel area 2.3 μm × 2.3 μm where 16 antenna elements are configured to collect all incoming polarizations. It is obvious that in this configuration, 4 elements are in series and 4 of such combined elements are placed in parallel. In this

case both the voltage and current from the detector array are multiplied by 4. Fig. 4.3 shows the current distributions on the antennas for a vertically polarized incident wave where all elements are excited equally and a 45°-tilted linear polarization where only the polarization aligned antenna elements are excited. The detected DC voltage and current can easily be picked from the middle of the horizontal lines (at the null position of IR current) without disturbing the IR current distributions on the antennas. It is also noted that other array configurations can easily be designed where the elements are polarization sensitive such vertical, horizontal, or even circular polarizations.

4.5 Conclusion

In this chapter, the utilization of the bowtie antenna loaded with the InGaAsSb for the near IR detector is presented. Sensitivity improvement of an antenna-loaded detector operating at near IR band is analyzed in terms of the field enhancement at the antenna terminals and relevant antenna effective area. The performance of the bowtie antenna loaded with InGaAsSb detector is compared to the conventional InGaAsSb detector using the detectivity parameter. When the detector noise is dominated by Johnson noise (thermal noise), it is shown that the detectivity of the antenna-loaded detector is improved significantly by a factor equal to the antenna field enhancement factor, approximately 20. Also a method for connecting many of such antennas in series, parallel, or combination of the two is presented to configure a desired output voltage or current from the detector array without affecting the performance of the constituent detector elements.

Chapter 5

Cross Dipole Antenna Topology for an IR Polarimetric Detector

Passive sensing using an infrared (IR) imagers can be improved substantially by the provision of polarimetric measurements. By measuring the Stoke's vector of the IR radiation as opposed to total power alone, much more information about the source of emission can be gleaned. The modified Stoke's vector can be measured if the signal intensity from independent polarizations are measured. The modified Stoke's vector is given by,

$$S = \begin{bmatrix} S_0 \\ S_1 \\ S_2 \\ S_3 \end{bmatrix} = \begin{bmatrix} \langle |\mathbf{E_v}|^2 \rangle \\ \langle |\mathbf{E_h}|^2 \rangle \\ 2\mathrm{Re}\langle \mathbf{E_v}\mathbf{E_h}^* \rangle \\ -2\mathrm{Im}\langle \mathbf{E_v}\mathbf{E_h}^* \rangle \end{bmatrix} \tag{5.1}$$

In the modified Stoke's vector, S_0 represents the power in the vertical polarization and S_1 represents the power in the horizontal polarization. Also S_2 and S_3 represent power quantities that are measuring the coherence between the vertical and horizontal channels and are proportional to the mean phase difference between the vertical and horizontal channels [75]. At optical frequencies, measurement of phase is not possible but it is possible to calculate three arguments from the measured response of a right-hand circular

polarized (RHCP) and 45°-polarized antennas. Suppose that the emission is measured by a RHCP antenna whose polarization vector is given by

$$\widehat{\mathbf{P}}_{\mathrm{RHCP}} = \frac{\hat{\mathbf{v}} - \mathrm{j}\,\hat{\mathbf{h}}}{\sqrt{2}} \tag{5.2}$$

Then the received power is proportional to

$$|\mathbf{E_{RHCP}}|^2 = \frac{1}{2}(\mathbf{E_v} - \mathbf{jE_h})(\mathbf{E_v^*} + \mathbf{jE_h^*}) = \frac{1}{2}\{|\mathbf{E_v}|^2 + |\mathbf{E_h}|^2 - 2\mathrm{Im}[\mathbf{E_v E_h^*}]\}$$

$$= \tfrac{1}{2}(S_0 + S_1 + S_3) \tag{5.3}$$

Now suppose that the emitted signal is measured by a 45°-polarized antenna with its polarization vector

$$\widehat{\mathbf{P}}_{45^\circ} = \frac{\hat{\mathbf{v}} + \hat{\mathbf{h}}}{\sqrt{2}} \tag{5.4}$$

the received power is then given by

$$\left|\mathbf{E}_{45^\circ}\right|^2 = \frac{1}{2}(\mathbf{E_v} + \mathbf{E_h})(\mathbf{E_v^*} + \mathbf{E_h^*}) = \frac{1}{2}\{|\mathbf{E_v}|^2 + |\mathbf{E_h}|^2 + 2\mathrm{Re}[\mathbf{E_v E_h^*}]\}$$

$$= \tfrac{1}{2}(S_0 + S_1 + S_2) \tag{5.5}$$

From the last two latter equations, S_2 and S_3 can be obtained from

$$S_2 = 2\left|\mathbf{E}_{45^\circ}\right|^2 - |\mathbf{E_v}|^2 - |\mathbf{E_h}|^2,\ S_3 = 2|\mathbf{E_{RHCP}}|^2 - |\mathbf{E_v}|^2 - |\mathbf{E_h}|^2 \tag{5.6}$$

To fully measure all the components of the Stoke's vector, an antenna which measures circular polarized (CP) radiation is required. Thus an antenna topology for CP operation is introduced in this chapter and the CP operation of the antenna topology is demonstrated experimentally in the gigahertz (GHz) range. Then, the antenna topology is applied for designing a CP antenna operating at the IR band, and its utilization for a compact antenna-loaded polarimetric IR detector is presented.

5.1 Cross Dipole Antenna Topology and its usage for Direction Finding in the GHz range

5.1.1 Introduction

In this chapter an antenna topology capable of producing the CP wave at its boresight in GHz frequency range is designed. CP radiation from this antenna operating in the GHz range is first validated experimentally before moving to a CP antenna design at the IR band. The proposed antenna topology is a cross dipole antenna instead of a microstrip antenna. A microstrip antenna topology has often been used when CP antennas are needed, such as in hand-held GPS devices, due to its low profile, light weight, and easy integration into the circuit [76]. However microstrip CP antennas suffer from their low axial ratio bandwidth. Because dipole antennas show a relatively broader bandwidth than microstrip antennas, several studies have implemented dipole CP antennas to achieve broader bandwidths and also wider beamwidths [77, 78, 79]. On the other hand, CP antenna structures based on cross-dipole geometry have complex feed including 90° phase shifter which usually requires multiple layers [77, 78, 79]. These features of current dipole CP antennas result in its bulky architecture and multi-step fabrication process.

In this section, a compact cross dipole antenna where two perpendicular dipole antennas in conjunction with two in-plane loops connecting the adjacent branches of the two dipoles to achieve a single layer and a single feed CP antenna. This architecture is easy to fabricate and the single layer of metallic traces of the antenna in conjunction with a single port gives rise to polarization excited using a balanced transmission line. The proposed antenna topology also has a polarization variation as a function of radiation direction. Basically two perpendicular dipole antennas in the cross dipole topology

radiate CP at the antenna boresight and distinct polarization at different directions except for the plane that contains the cross dipole. Thus the cross dipole can be a base for an antenna array to generate the unique polarization at any point in space. The measured power at any point in space from which the altitude of the receiver with respect to the antenna array using the cross dipoles can be determined. This feature can be used for positioning and direction-finding where the current global positioning systems (GPS) are not available [80].

The modern direction finding (DF) systems utilize the phase or amplitude of incoming signals by multiple antennas to find the angle of arrival [81, 82]. DF systems have utilized ESPRIT and MUSIC algorithms for multi-channel receiver systems and Watson-Watt and Pseudo-Doppler algorithms for single channel receiver systems [83, 84, 85]. In such DF systems, the multiple numbers of the antenna units give rise to a large physical size which is not viable for mobile or vehicle-mounted devices. Also the coupling among antennas results in ambiguity in finding the direction of incoming signals [86]. Due to the difficulties in realizing an accurate and compact DF system using multiple numbers of antennas, antennas having a unique mapping between a polarization state and a propagation direction can be used for a compact DF application. The polarization characteristic of the antenna could significantly simplify an algorithm for DF which traditionally requires the covariance matrix calculation and calibration between multiple antennas of the system. A DF algorithm here utilizes the amplitude and phase information from one horizontal and vertical dipole of a receiver and matches a polarization state of the wave measured at the receiver to the polarization map of the cross dipole antennas (the transmitter). The unique polarization at a specific arbitrary

azimuth and elevation angle allows for the receiver to calculate its angular coordinate with respect to the cross dipole antennas. The polarization state of the cross dipole antenna can be represented by the tilt (ψ) and ellipticity (χ) angles of the polarization ellipse and the receiver can use ψ and χ to estimate θ and ϕ. A unidirectional version of the cross dipole topology is fabricated and a balun structure is utilized for ease of feeding with a coaxial line. The measured S-parameters, axial ratio, radiation pattern are measured and compared with the simulation results.

5.1.2 Cross Dipole Antenna Structure

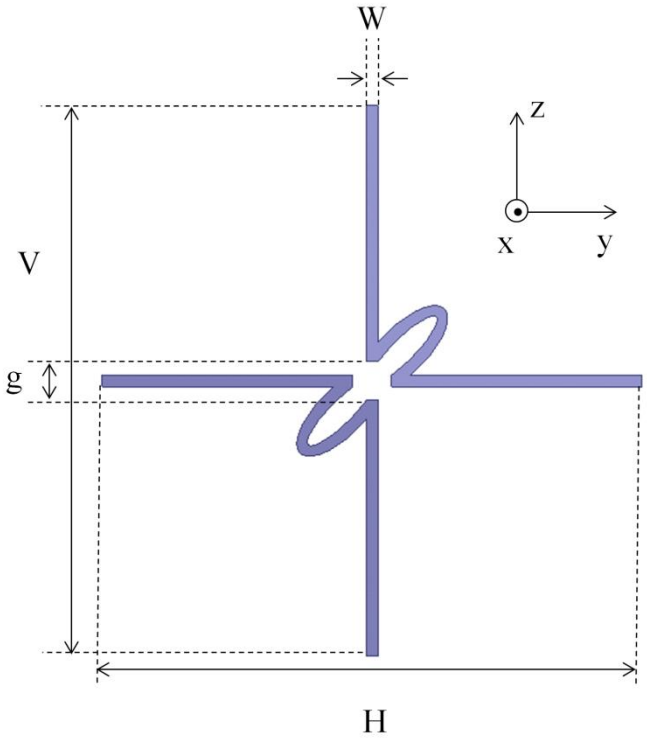

Figure 5.1: CP cross dipole antenna.

In Fig. 5.1, a CP antenna design is shown using a cross dipole with two 90° phase shift lines which are placed on the same plane. This feature makes this antenna more compact and its fabrication easier. Also, the single feeding point is needed to achieve a CP radiation at the antenna boresight. The lines are shaped as ellipses and are connected

at the terminals of each vertical and horizontal dipole with 90° phase difference. The placement of the ellipses in the first and third quadrants, or the second and fourth quadrant of the cross dipole structure can produce RHCP or LHCP respectively. The length of the phase shifter and the length of each vertical and horizontal dipole are optimized so that a perfect CP at the antenna boresight is achieved at 1.0 GHz. Also, the inductive coupling from the phase line can be utilized for an impedance matching element when this antenna is loaded with a semiconductor p-n junction for IR applications. In Fig. 5. 1, the vertical length (*V*) is 142.5 mm and the horizontal length (*H*) is 139.8 mm. The gap size (*g*) for feeding vertical dipoles is set as 10.0 mm and the width of the traces is 3 mm. The major axis of the ellipse for the phase line is 16 mm. In the antenna design procedures, the length of the vertical antenna alone is set to realize the resonance at 1.0 GHz, and the same length for the horizontal dipole is also chosen. Then the length for the ellipses for the phase shift is optimized to provide 90° phase difference between the far-field of E_θ and E_ϕ at the boresight. Finally, the length of the horizontal dipole is decreased to achieve the same magnitude of E_θ and E_ϕ at the boresight. The final antenna design is depicted in Fig. 5.1. This design realizes the perfect LHCP where the magnitudes of E_θ and E_ϕ are equal, and the phase difference between both perpendicular field components is positive 90° at the boresight.

5.1.2.1 Polarization Map

At resonance, the relative difference between azimuth (ϕ) and elevation (θ) components of the electric field in the far-field region of the cross dipole antenna is defined in (5.3). The formulas for tilt (ψ) and ellipticity (χ) angles of polarization ellipse are represented by (5.4).

$$\frac{E_\phi}{E_\theta} = Ae^{j\delta} \tag{5.3}$$

$$\tan 2\psi = \frac{2A}{1-A^2}\cos\delta,\ \sin 2\chi = \frac{2A}{1+A^2}\sin\delta \tag{5.4}$$

The polarization map represented by ψ and χ as a function of ϕ and θ angles are calculated and shown in Fig. 5.2.

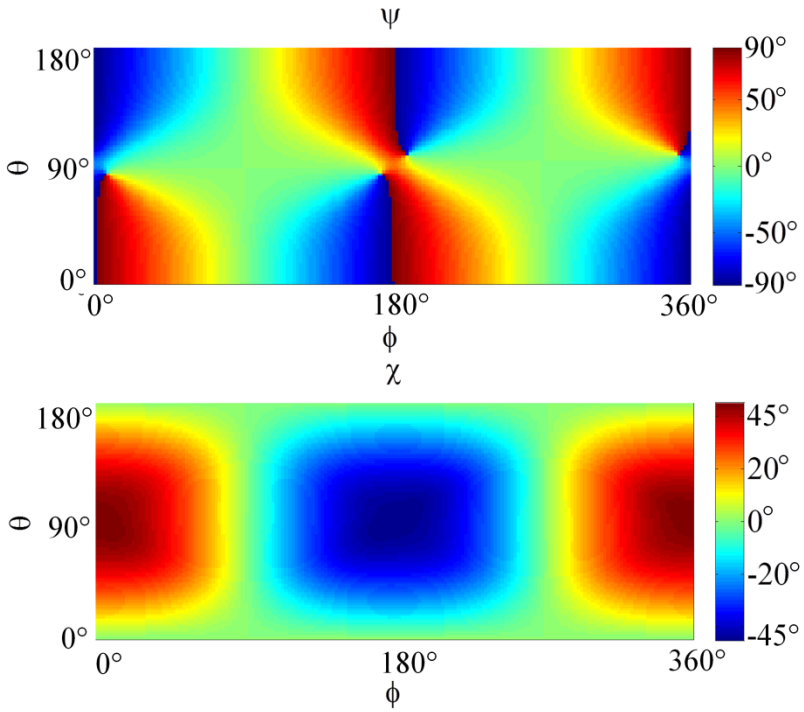

Figure 5.2: Polarization map of CP cross dipole antenna.

In the ellipticity map, the red peak (+45°) at the forward direction shows LHCP and the blue peak (-45°) at the backward direction shows RHCP. At ϕ = 90°, zero χ indicates the linear polarization. For better understanding, Fig. 5. 3 (a) illustrates the perfect LHCP at the boresight of the antenna and the linear polarization in the plane of the cross dipole antenna.

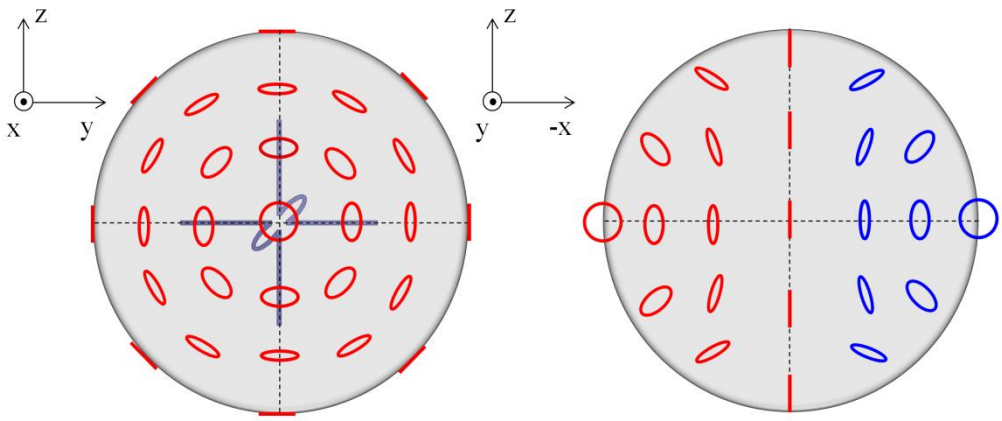

(a) (b)

Figure 5.3: Illustration of polarization status at (a) the y-z plane and (b) the x-z plane (red-colored and blue-colored shapes indicate LHCP and RHCP respectively).

The symmetry of the antenna along the axes of $\theta = +45°$ and $\phi = 90°$ or $\theta = 135°$ and $\phi = -90°$ results in the same polarization state at the opposite side along those axes. Also the unique polarization property at an arbitrary propagation direction with only ambiguities along the z axis at the x-z plane is shown in Fig. 5. 3 (b). Thus a vertical and horizontal-polarized field radiated from two units of the cross dipoles at any far-field region can be converted to a specific propagation direction from the cross dipole antenna. As a result, direction-finding from the position of the cross dipole antennas can be achieved.

Also Fig. 5.4 also, shows the radiation pattern of the proposed CP antenna at 1.0 GHz which has an isotropic radiation (no radiation null) at the x-y and the x-z plane. This feature is also useful for tracking a target without considering azimuth and elevation angle dependence.

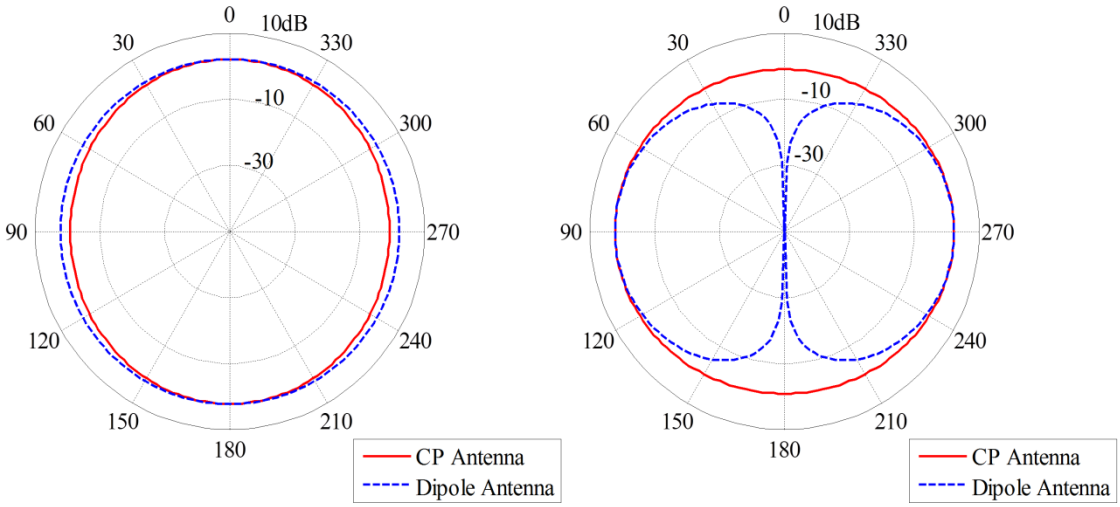

(a) (b)

Figure 5.4: A comparison between radiation pattern (gain) for the cross dipole antenna and a half-wave dipole antenna at (a) x-y plane as a function of phi (ϕ) and (b) x-z plane as a function of theta (θ).

5.1.3 Antenna Measurement

5.1.3.1 Balun for Feeding

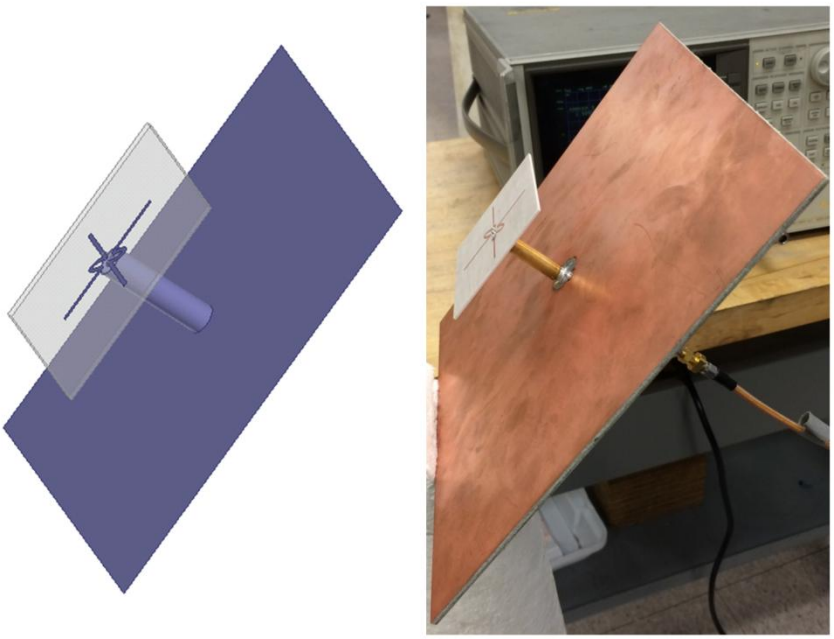

(a) (b)

Figure 5.5: (a) The CP cross dipole antenna using a balun structure in simulation and (b) the fabricated antenna.

For a feeding structure of the perfect CP cross dipole antenna, a balanced feed is required. A balanced excitation for the antenna is realized by a balun structure. Also, a ground plane to prevent the effect of the feeding line on the radiation of the antenna is used. Fig. 5.5 (a) shows the antenna structure with the balun structure in a simulation tool and Fig. 5.5 (b) shows its fabricated version. The antenna structure is patterned on a substrate, Rogers 4003 ($\varepsilon_r = 3.55$) which stabilize the position of antenna structure.

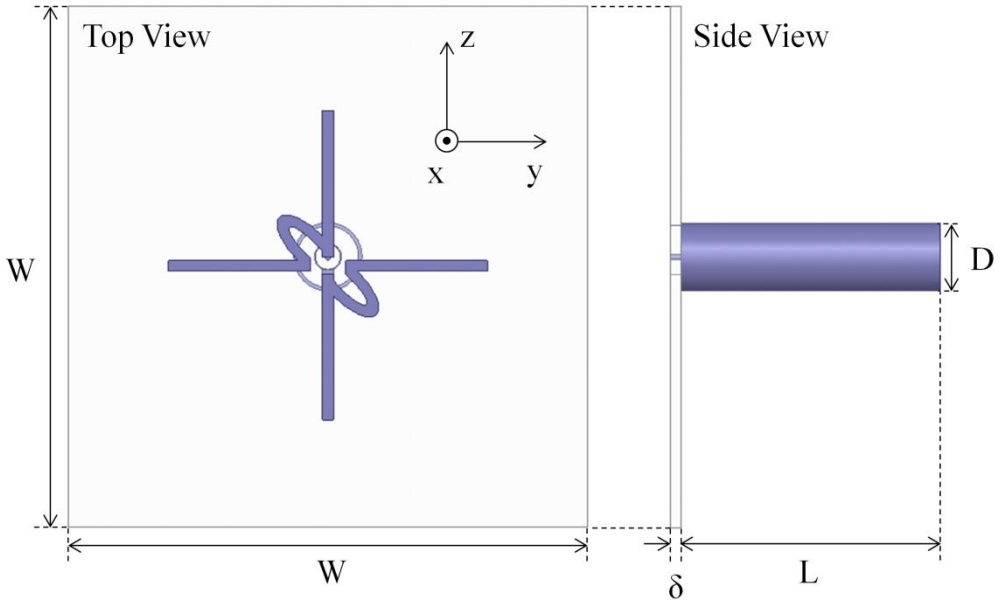

Figure 5.6: The CP cross dipole antenna structure using the balun structure in simulation.

Dimension of the antenna structure on the substrate is optimized to achieve a perfect CP at 2.58 GHz. Fig. 5.6 shows a top view of the cross dipole antenna structure mounted on the Rogers 4003 substrate with a width (*W*) and a side view of the antenna with a balun structure which covers the feeding coaxial cable. The length of the balun (*L*) is set 36.5 mm and the diameter of the stub (*D*) is set 9.65 mm. The antenna structure is patterned on the 60-mil (δ) thick and 73.25 mm (*W*) wide substrate. The vertical length of the dipole (*V*) is 43.4 mm and the horizontal length of the dipole (*H*) of the cross dipole antenna is 45 mm. The gap size (*g*) for feeding the vertical dipole is set 2.34 mm and the width of the traces is 1.5 mm. The diameter of inner and outer core of the coaxial line is chosen as 0.9 mm and 3.56 mm, respectively. The balun using a copper cylindrical tube with the same length of the coaxial cable covers the coaxial feeding line. The tip of the tube is connected to the one of the antenna's metallic traces which is also connected to the inner core of the coaxial cable. The open termination at the tip of the balun due to its

quarter wavelength from the ground plane (short termination) suppresses current flow along the surface of the outer core of the coaxial cable.

5.1.3.2 Measurement Result

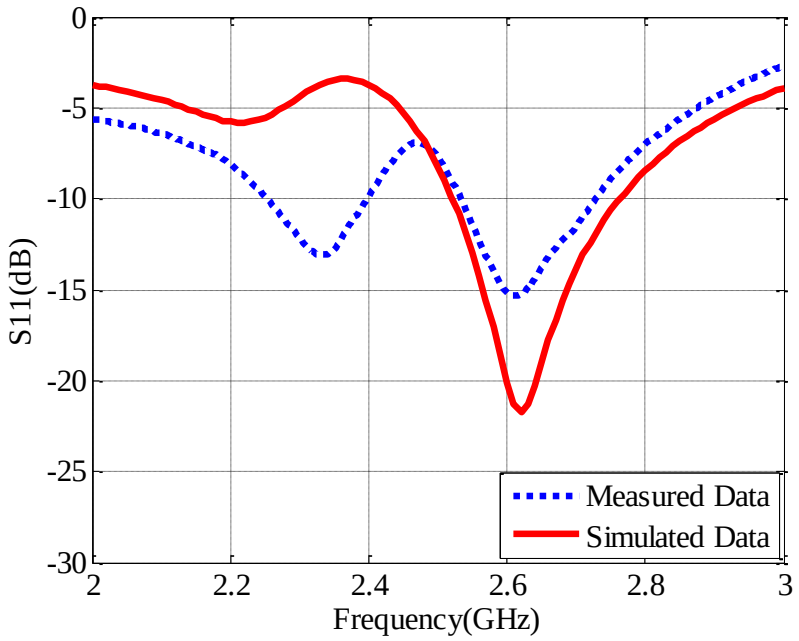

Figure 5.7: S11 of the CP cross dipole antenna using the balun structure in simulation and fabricated antenna.

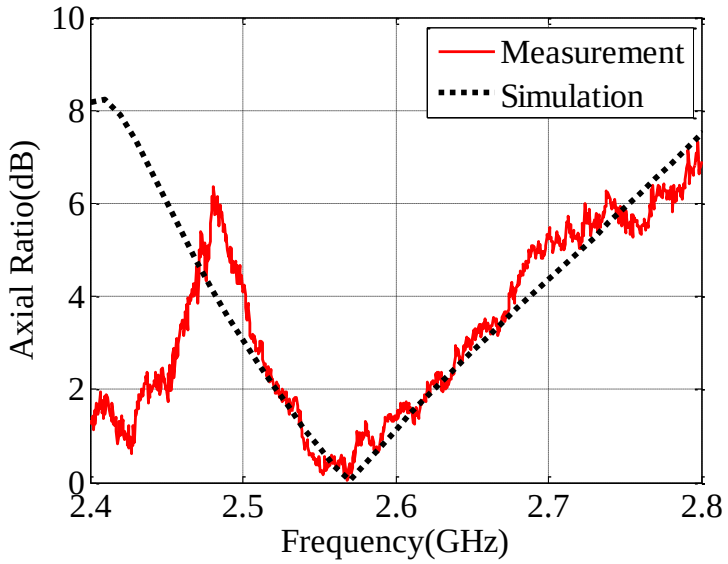

Figure 5.8: Axial ratio of the CP cross dipole antenna using the balun structure in simulation and fabricated antenna.

Fig. 5.7 and Fig. 5.8 show the S11 and the axial ratio of the antenna in simulation and measurement. The resonance of the measured S11 at 2.6 GHz is shown as expected from the simulation. The Fig. 5.8 shows that zero dB axial ratio at 2.58 GHz and 6.2% of the 3 dB axial ratio bandwidth for both measured and simulated data. The measurement result shows another S11 resonance and zero dB point of the axial ratio below 2.4 GHz due to the finite size of the ground plane of the fabricated antenna.

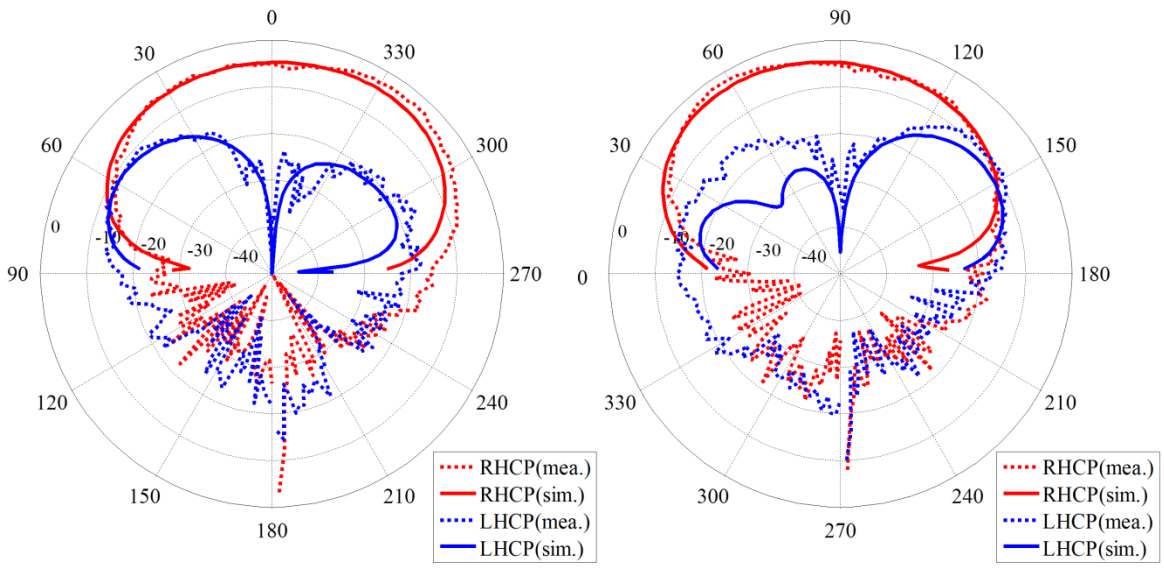

(a) (b)

Figure 5.9: Radiation pattern (normalized gain) of the antenna of in measurement and simulation of (a) x-y plane as a function of phi(ϕ) and (b) x-z plane as a function of theta (θ) at 2.58 GHz.

Fig. 5.9 shows the simulated and measured radiation pattern of a RHCP cross dipole antenna and both patterns are matched correspondingly. A slight asymmetry of the LHCP pattern along both theta (θ) and phi (ϕ) direction can be understood by a slight asymmetry of current excitation to the feed gap of the antenna. The maximum of RHCP pattern and distinct suppression of LHCP at the boresight mean that the perfect RHCP wave is radiated along the forward propagating direction of the antenna. This measured radiation pattern using the planar cross dipole antenna topology verifies the functionality of the antenna in terms of CP wave generation and detection.

5.2 Antenna-Loaded IR Polarimetry System

5.2.1 Introduction

Imaging polarimetry can measure the polarization status of the emitted field from a scene in addition to the intensity and color which traditional imagers can detect. The polarization information related to the vector nature of the optical wave can show the surface roughness, the shading of target material and the distinct contrast image which are uncorrelated with the intensity and color [87]. To describe the polarization state of an arbitrarily polarized signal, the full Stoke's vector of the signal should be measured, but characterization of the fourth element (S_3) of the vector related to CP has been a challenge. The linear polarization imaging which achieves parts of the Stoke's vector (S_0, S_1, and S_2) have been realized in the visible to long-wave IR range [88, 89, 90]. However CP sensitive imaging which commonly utilizes linear polarizers integrated with birefringent quarter-wave plates cannot be implemented easily [91]. This is due to the fact that fabricating the quarter-wave plate for detecting CP wave is quite challenging in a microscale or nanoscale. Instead of using the birefringent polarization plate, the dielectric grating or metallic grating in conjunction with the linear polarizer to detect CP wave has been demonstrated [92, 93, 94, 95]. Antenna elements such as cross-shaped dipoles, apertures, patch antennas, L-shaped antennas, and spiral grating are used to realize the birefringence [28, 96, 97, 98, 91, 99, 100, 101, 102, 103, 104]. Also, the antenna prototype of the spiral shape for CP wave detection was introduced at the IR band [105, 106]. As claimed by previous research, devices to convert the linear polarization to the perfect CP in the optical or IR band are necessary to realize a full Stoke's vector imager.

In this section, the cross dipole antenna topology for the perfect CP wave generation in microwave range is applied for designing a CP antenna topology at the IR band. The CP antenna at the IR band utilizes a tapered-bowtie shape instead of the dipole shape in the GHz range. Generally, multiple circular or rectangular turns from the spiral-shaped antenna for CP generation are required. However, in this case, the cross dipole antenna using the bowtie shape of the antenna is easier for fabrication and can be realized as a more compact device. The proposed crossed bowtie CP antenna also utilizes the InGaAsSb p-n junction on its terminals. For the CP detection at the IR band, the antenna measures the component of CP from any polarized incident wave and the DC power generated from InGaAsSb block due to the field enhancement can be used to determine the magnitude of CP component of the wave. The direct conversion from the field enhancement to DC current using the semiconductor material can provide significant advantage for measuring the polarization state of the IR incident wave. Otherwise, the birefringent material and antenna structures without being loaded with a semiconductor p-n junction require extra detecting instruments such as spectrometers or cameras for the same purpose.

In this section, the optimization of the crossed bowtie antenna to generate the perfect CP at 180 THz is presented. The resonance conditions of the antenna for generating CP wave at its boresight and the maximum power transfer between the antenna and the InGaAsSb load are discussed. For an IR polarimetry system, a conceptual focal-plane array which contains vertical, horizontal, 45°-tilted, and RHCP antennas is introduced. This proposed focal-plane array can be used for a compact

polarization imaging system where the Stoke's vector of any polarized IR wave is fully characterized.

5.2.2 IR Cross Dipole Antenna Structure

A cross tapered-bowtie antenna to realize the perfect CP is designed at the IR spectrum. Similar to the antenna built in the GHz range, the IR CP antenna consists of a vertical, a horizontal bowtie antenna and two ellipses for creating a 90° phase shift. Also, all metallic traces for the antenna structure are modeled by Drude formula of gold at IR regime. In addition, the dimension of the InGaAsSb block at the terminals of the antenna is fixed to 30 nm × 30 nm × 30 mm. Firstly, the vertical tapered-bowtie's length without being loaded with InGaAsSb block is designed. Because the antenna should be characterized without considering the effect of the load, a vacuum is loaded at the terminals of the antenna. Later, the intrinsic input impedance of the bowtie antenna is calculated by de-embedding the capacitance of the vacuum (30nm × 30nm × 30nm) from the simulated input impedance of the antenna.

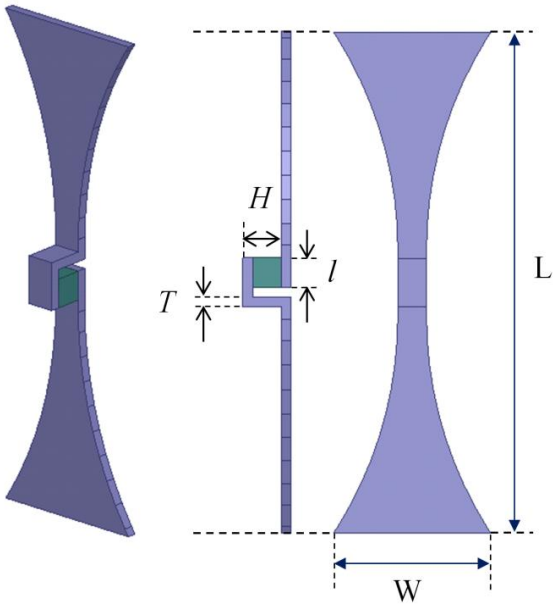

Figure 5.10: Tapered-bowtie antenna geometry for vertical polarization.

Fig. 5.10, shows the tapered-bowtie antenna of 510 nm length (L) and W = 164 nm, $H = l$ = 30 nm, and T = 10 nm.

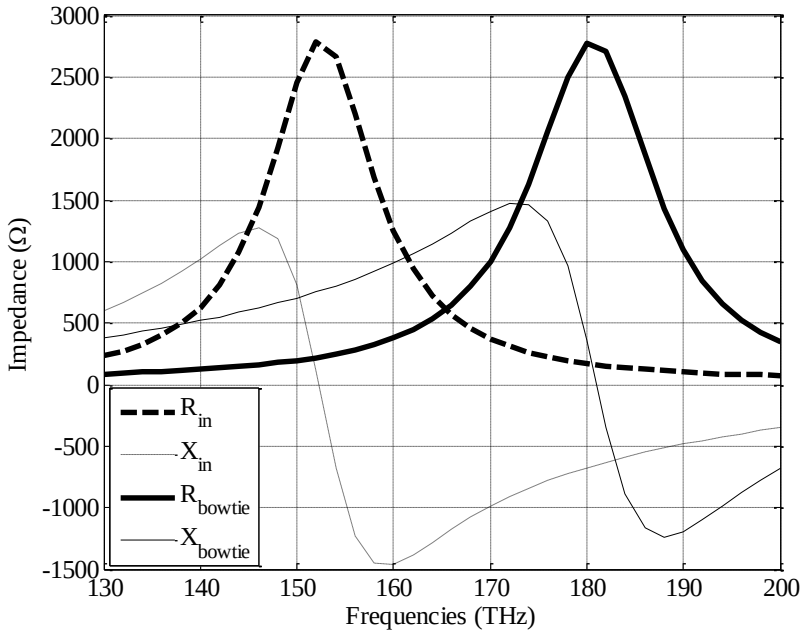

Figure 5.11: Input impedance (R_{in} + jX_{in}) of the tapered-bowtie antenna loaded with vacuum and the intrinsic input impedance (R_{bowtie} + jX_{bowtie}) of the antenna (vacuum is de-embedded).

The vertical tapered-bowtie antenna provides the first parallel resonance of its de-embedded input impedance at 180 THz as shown in Fig. 5.11. This resonant frequency is optimum for operation in the band where the quantum efficiency of InGaAsSb load is maximum. The solid line shows the intrinsic impedance of the antenna where the resistance at the parallel resonance is shown to be around 2.77 kΩ. Based on the vertical antenna dimension, the horizontal bowtie and the length of the ellipses for the phase shift are optimized. Mainly, the target for the optimization is to achieve the perfect CP operation at 180 THz and at the antenna boresight.

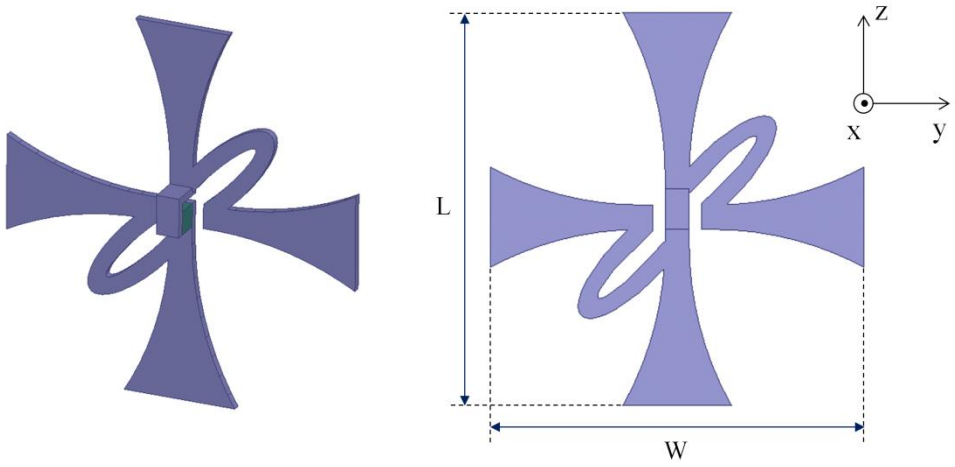

Figure 5.12: CP cross tapered bowtie antenna structure and its dimensions.

In the optimization procedure, the length of the ellipse and the length of the horizontal bowtie interchangeably are adjusted. The realization of 90° phase shift between E_ϕ and E_θ at the boresight is only possible when the length of the horizontal bowtie (*W*) is 465 nm which is shorter than the length of the vertical bowtie (510 nm). This case still does not fulfill the condition for the same magnitude of E_ϕ and E_θ at the boresight. Thus, the vertical bowtie's length (*L*) needs to be shortened to 480 nm to match the magnitude of E_ϕ and E_θ at the boresight. In the optimized design in Fig. 5.12, the

length of the horizontal bowtie antenna (*W*) is maintained as 465 nm and the major radius and width of the ellipses are set at 100 nm and 30 nm, respectively.

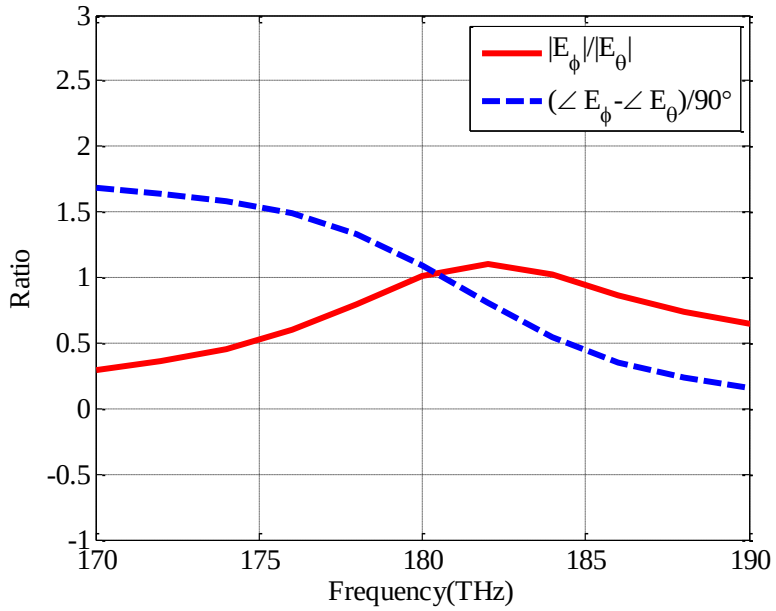

Figure 5.13: The magnitude ratio and the normalized phase difference between radiated electric field in ϕ and θ direction in the antenna's boresight.

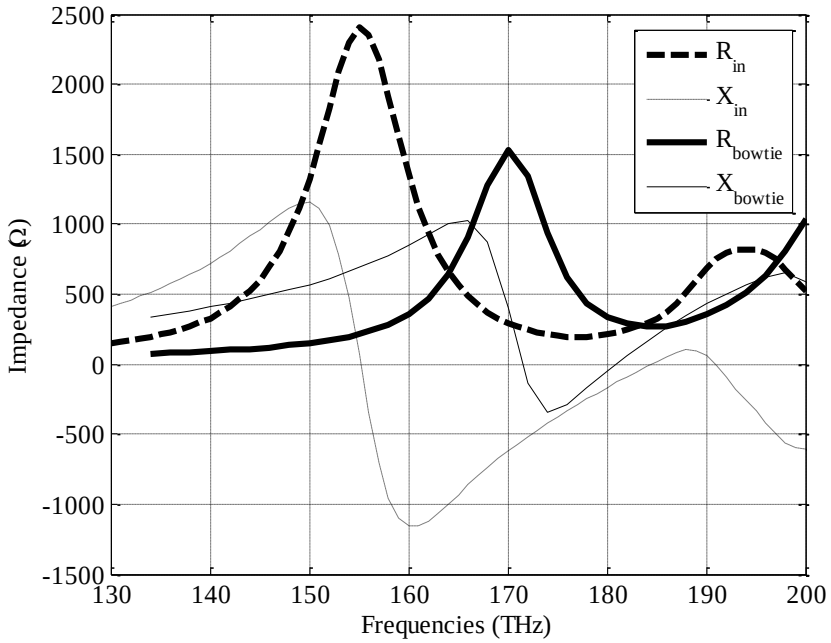

Figure 5.14: Input impedance (R_{in} + jX_{in}) of the cross bowtie antenna loaded with vacuum and the intrinsic input impedance (R_{bowtie} + jX_{bowtie}) of the antenna (vacuum is de-embedded).

Fig 5.13 shows that two conditions for the perfect CP are satisfied: 1) the magnitudes of the far-field of E_ϕ and E_θ are equal and 2) the phase difference between both fields is 90°. The input impedance of the cross bowtie antenna is also shown in Fig. 5.14. The input impedance of the antenna loaded with the vacuum block shows its parallel resonance at 158 THz. One thing to note is that the first parallel resonance of the intrinsic input impedance of the antenna is located around 170 THz which is lowered than 180 THz. Instead of the parallel resonance, CP occurs near at the second series resonance of the intrinsic input impedance of the antenna, ~ 180 THz. This fact invokes the idea that the impedance matching using the parallel resonance of the antenna for the maximum power transfer between the bowtie antenna and the high impedance semiconductor load does not correspond to the resonance condition for CP radiation at the boresight. This issue will be mentioned more clearly after analyzing the optimized cross bowtie antenna loaded with the InGaAsSb material.

As a final step, the IR CP antenna is loaded with the InGaAsSb block and its load effect at the terminals of the antenna is considered. This loading effect complicates the optimization procedure for achieving CP property of the IR antenna because the high capacitance of InGaAsSb block significantly lowers down the resonant frequency of the antenna. The same cross bowtie antenna shown in Fig. 5.12 loaded with the InGaAsSb block is expected to lose its CP property at the desired frequency. Thus, a method to compensate the capacitance of the InGaAsSb load at the resonant frequency should be applied to the CP antenna design procedure in the IR regime.

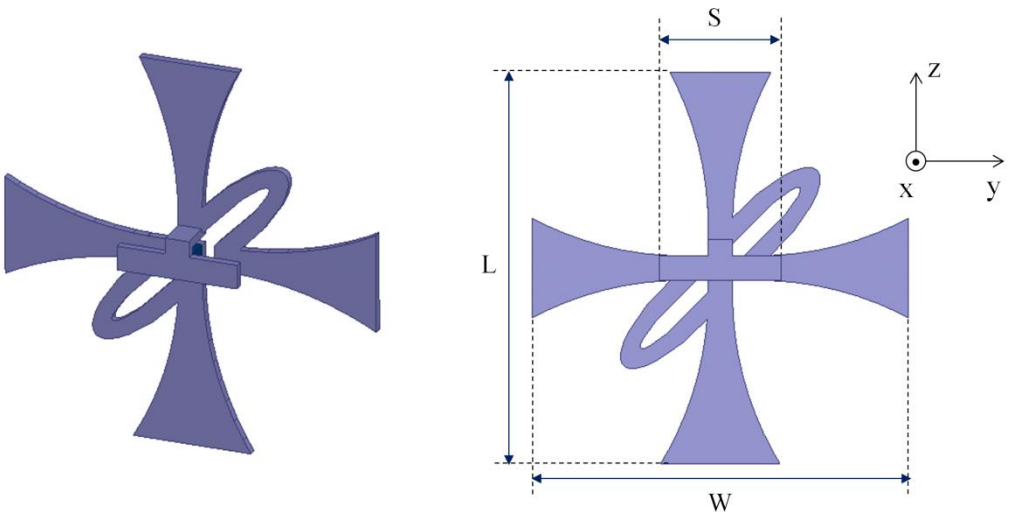

Figure 5.15: CP cross tapered bowtie antenna structure connected with open-ended transmission lines and its dimensions.

To cancel the high capacitance of the InGaAsSb at 180 THz, two shunt inductive transmission lines are implemented symmetrically, as shown in Fig. 5.15.

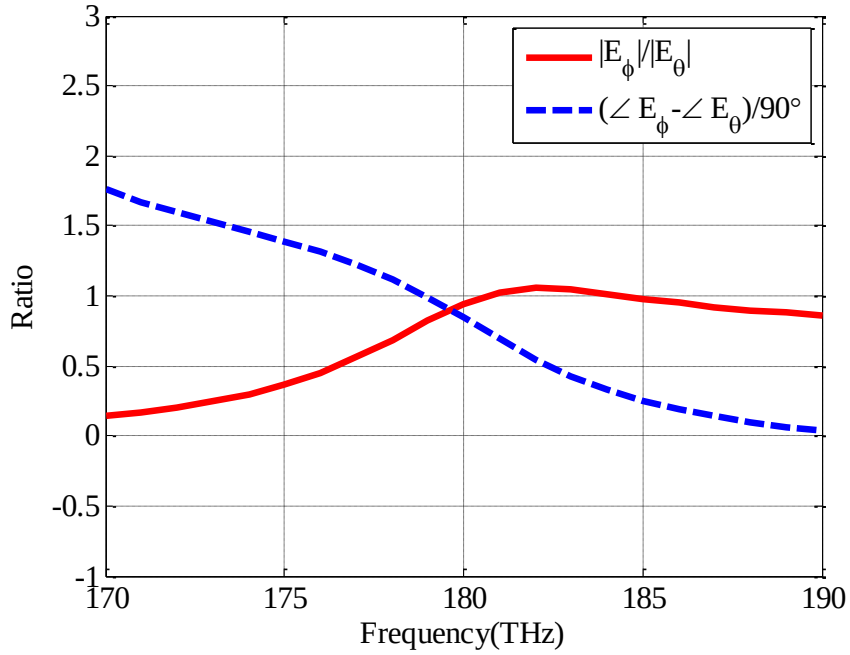

Figure 5.16: The magnitude ratio and the normalized phase difference between radiated electric field in ϕ and θ direction in the antenna's boresight.

The final optimization with a stub length (S = 150 nm) provides a CP operation with $|E_\phi|/|E_\theta| = 0.90$ and $\angle E_\phi - \angle E_\theta = 81^\circ$ at 180 THz from the cross bowtie antenna loaded with the InGaAsSb block. The inductive transmission line stubs cancel the capacitance of the InGaAsSb load at 180 THz, and the CP feature of the antenna itself at 180 THz is maintained. The lengths of the vertical (L) and horizontal (W) bowtie antenna are maintained as 480 nm and 465 nm.

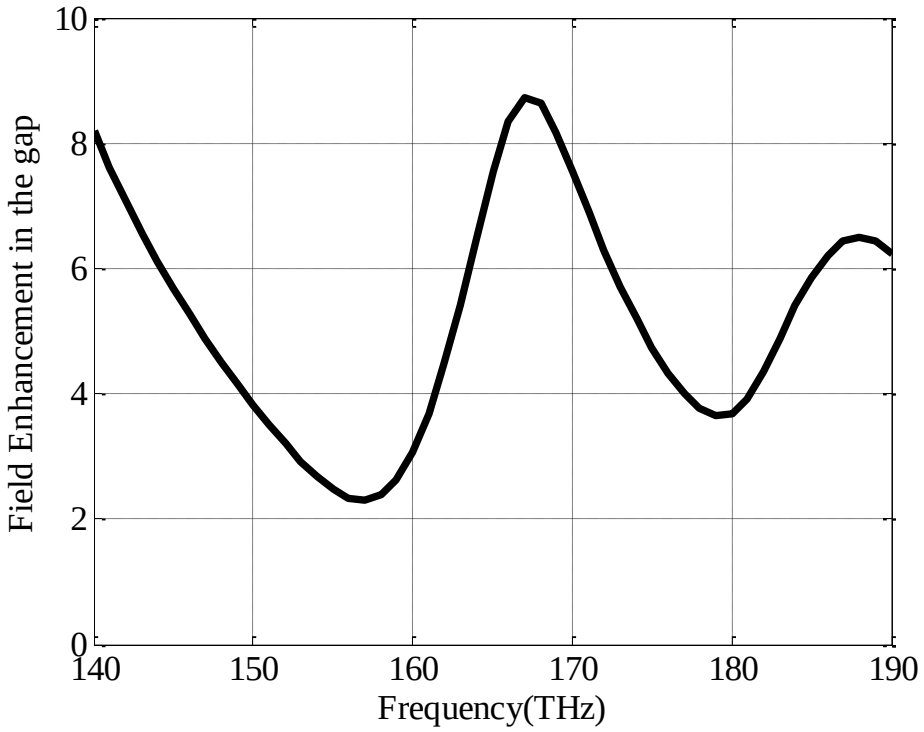

Figure 5.17: The field enhancement at the gap of the cross tapered-bowtie antenna.

Also the field enhancement at the terminals of the antenna is required for sensitive detection, thus the field enhancement should be studied. Similar to the previous linear polarization bowtie antenna design, the near field maximum occurs near at 170 THz in Fig. 5.17. This frequency is similar to the parallel resonance frequency of the intrinsic input impedance of the cross bowtie antenna shown in Fig. 5.14. This same frequency for

the maximum field enhancement and the parallel resonance of the intrinsic antenna impedance also indicates that the capacitance of the InGaAsSb is compensated by the inductance from the open-ended transmission lines. However, a relatively low field enhancement, approximately 4 at 180 THz is observed. This can be attributed to the fact that CP radiation occurs at the series resonance of antenna as mentioned earlier but the maximum field enhancement occurs at the parallel resonance. Even though this resonant frequency for CP is not compatible to the parallel resonance, a successful realization of an IR antenna which shows the perfect CP operation at the desirable frequency is worthwhile. Also, the proposed cross tapered-bowtie antenna can be integrated into a focal-plane array by connecting the antenna units using the metallic traces and this antenna array is also optimum for the realization of an efficient and high-resolution IR polarimetry.

5.2.2.1 Antenna-loaded IR Polarimetry System

Finally, with this cross bowtie antenna for the perfect CP detection and also with the bowtie antenna which is linear polarization, an efficient IR full Stoke's vector polarimetry is suggested. The favorable features from the efficient antenna and its applicability to the focal-plane array are the best fit to a sensitive IR polarimetry system. Optimized and simple thin metallic trace can connect antenna elements and the output can be measured by the probing the output metallic pad. The function of the detector to sense CP is realized by arrays of the optimized cross bowtie antennas for RHCP, and arrays of the vertical, horizontal, and 45°-titled bowtie antennas can measure S_0, S_1, and S_2 components of the Stoke's matrix..

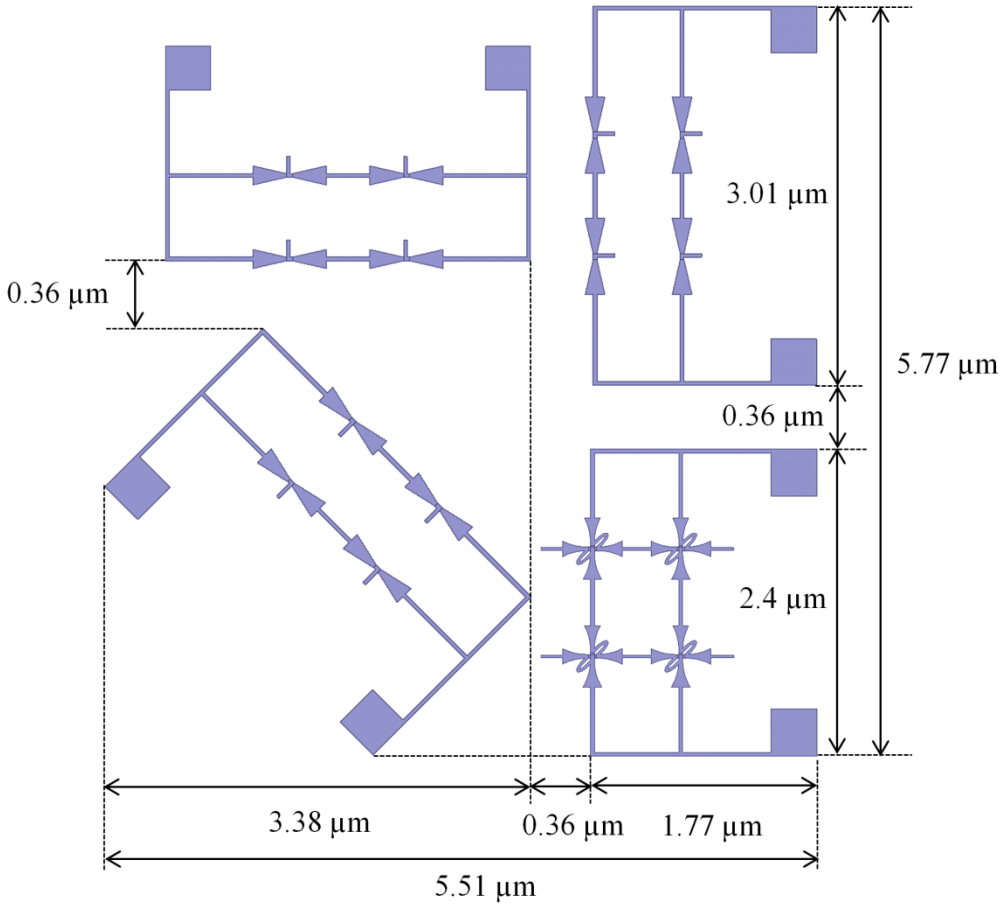

Figure 5.18: The proposed IR polarimetry for the full Stoke's vector using arrays of the vertical, horizontal, 45°-titled, and RHCP antennas.

The proposed IR polarimetry for characterizing the full Stoke's vector is introduced and a separate focal-plane array for each polarization component for arbitrary incident wave is shown in Fig. 5.18. As shown in (5.1) and (5.2), S_0, S_1 and S_2 components of the Stoke's vector can be measured from the arrays of the vertical, horizontal, and 45°-titled antennas. Measured DC power from the arrays of the RHCP antennas which are located on the system in Fig. 5.18 can determine S_3. The pixel size specified by 5.77 µm × 5.51 µm can provide approximately 31,500 pixels in one mm^2-area device. Also, the improvement of sensitivity from the antenna-coupled detector due

to the field enhancement can be also expected for arrays of the antennas. Finally, the proposed arrays with optimum antennas which fully characterize Stoke's vector of the incoming IR signal can be utilized for a high-resolution and high sensitivity IR polarimetric detector.

5.3 Conclusion

A cross dipole antenna on a single planar layer using elliptical-shaped phase shifter lines in the microwave range is designed first. The cross dipole antenna where the two perpendicular polarized dipole antennas and the phase lines are patterned together gives rise to the perfect CP at boresight and the distinct polarization at different propagating directions except for the plane that contains the cross dipole. This antenna's polarization characteristic can realize a DF system using units of the cross dipole antennas for the transmitter and a pair of perpendicular polarized dipoles for the receiver (target). To demonstrate the validity of the design, a unidirectional antenna structure over a ground plane is fabricated and measured at 2.58 GHz. The isotropic radiation pattern at the x-y and the x-z plane and perfect CP waves at the antenna boresight are shown.

The validated cross dipole antenna for CP in the GHz range is applied to designing a compact cross tapered-bowtie antenna for CP detection at the IR band. During the antenna design, the effect of InGaAsSb block which lowers down the resonance frequency of the antenna is compensated by the extra open stub connected to the terminals of the antenna. The antenna design loaded with the InGaAsSb block shows CP with $|E_\phi|/|E_\theta| = 0.90$ and $\angle E_\phi - \angle E_\theta = 81^\circ$ at ~ 180 THz where the maximum quantum efficiency of InGaAsSb material is shown. Also the field enhancement in InGaAsSb block at 180 THz is shown as ~ 4. Finally, as an antenna-loaded polarimetric

IR imager, arrays of vertical, horizontal, 45°-tilted, and RHCP bowtie antennas all within a single imager pixel with a high resolution of ~ 31,500 in a mm^2 area are proposed to detect the Stoke's vector of incoming IR signals.

Chapter 6

Conclusions and Future Work

6.1 Summary of Achievements

In this thesis, an efficient antenna in terms of the radiation characteristic at terahertz (THz) frequency regime was developed to maximize the received power to the THz receiver system. The antenna can be used to overcome the limitations of THz communication such as the high path loss and the lack of high performance components. For this purpose, a highly conductive nanomaterial instead of metals was suggested for the efficient antenna fabrication material at THz frequency regime. Also the unique characteristics of metallic antennas at THz and optical frequencies such as the near field enhancement and confinement were exploited to enhance the performance of the infrared (IR) devices such as thermophotovoltaics (TPVs) and IR detectors. A topological optimization on the metallic antenna was performed to maximize the performance of IR devices. In addition, a topology of the metallic antenna for circular polarization (CP) at the IR band was investigated and its usage for an IR polarimetry was introduced.

A highly conductive nanomaterial, Bundled Carbon Nanotube (BCNT) was numerically analyzed for an antenna fabrication material at THz frequency. The low efficiency of the metallic antenna causes from the lower conductivity of metal at THz

frequency. Also the high surface impedance and surface roughness of a small scale metallic structure degrade the radiation efficiency of the metallic antenna at THz frequency. Thus as a substitute for metals, a highly conductive BCNT material where CNTs are densely aligned in parallel was utilized to overcome the low radiation problem of metals. For the numerical analysis, BCNT is modeled with an anisotropic material and gold is modeled with the Drude formula. The analysis shows that BCNT dipole antennas radiates more efficiently than gold antennas at 2 THz only if the density of CNTs in a BCNT structure is increased to 10^4 CNTs/μm. This analysis predicts that the currently realizable BCNT is not viable for an efficient antenna material at THz frequency and the current density of BCNT should be improved 10^3 times so that the BCNT antenna outperforms the metallic antenna in terms of radiation efficiency.

For an efficient TPV system for power conversion from IR waves to DC power, a gold antenna loaded with a low bandgap semiconductor, Indium Gallium Arsenide Antimonide (InGaAsSb), was presented. The optimization for the topology of the antenna and a novel matching technique yielded the maximum power transfer between the gold antenna and its InGaAsSb load. The novel matching technique uses the open transmission line stub to cancel out the high reactance of the InGaAsSb load. Finally, the topology of the antenna using its high impedance mode at the desired frequency, 180 THz, was determined as a bowtie shape and the size of the InGaAsSb load was set to a 30 nm cubic volume. The bowtie antenna showed the maximum power transfer at 180 THz and the field enhancement at the terminals as high as 23.5. A focal-plane array of the bowtie antennas for the TPV application showed 95% power absorption efficiency which is 50% higher than the efficiency of the traditional TPV. Also, for IR detector application, the

sensitivity improvement of the detector array using bowtie antennas was evaluated against the traditional bulky detector. The result showed that sensitivity is improved by the field enhancement factor, which is approximately 23. Based on this significant sensitivity improvement for the antenna-mounted IR detector, we concluded that the plasmonic metallic antenna has a more beneficial effect on IR detectors than TPV devices. As a realistic IR device, focal-plane arrays of the bowtie antennas with parallel and series connection and 45°-tilted connection using metallic traces were introduced.

For a realization of an IR polarimetry, a more complex antenna design problem for the circular polarization (CP) antenna in the IR range was investigated. A cross dipole antenna topology where two perpendicular dipole antennas in conjunction with two in-plane ellipse-shaped loops connecting the adjacent branches of the two dipoles to achieve a single layer and a single feed CP antenna. To verify the CP radiation from the antenna topology, the cross dipole antenna operating in the GHz range was designed and fabricated. The perfect CP wave was measured at 2.58 GHz. In addition, the CP antenna in the GHz range showed polarization states at different propagation directions with only ambiguities along for the plane that contains the cross dipole so that the usage of these antennas for a compact direction finding (DF) systems was suggested. For the IR CP antenna, a cross tapered-bowtie antenna was designed for the perfect CP at 180 THz along its boresight. In the CP antenna design procedure in the IR range, it was also found that a condition for CP of IR antenna does not correspond to the maximum power transfer condition. The final optimized cross bowtie antenna loaded with the InGaAsSb of a 30 nm cubic volume showed the perfect CP at 180 THz and the field enhancement, ~ 4. Finally, a focal-plane array which consists of the right-handed CP antennas in

conjunction with the arrays of vertical, horizontal, and 45°-tilted bowtie antennas were presented as a full Stoke's vector IR polarimetry imager which can provide a high resolution of ~ 31,500 pixels in a mm^2 area.

6.2 Future work

Throughout this thesis, for the most part, the numerical studies regarding the material and topology for the efficient antenna at THz and optical frequency were presented. Thus, the real application of the material and the structure using the current fabrication technique can be considered in future work. Chapter 2 provides a specific fabrication criteria, 10^4 CNTs/μm for the density of BCNT (i.e., the number of CNTs in a micron width of a BCNT sheet) to outperform the metal in terms of radiation efficiency at THz frequencies. This criteria is much more than a currently realizable density of BCNT and research for improving density of BCNT has not been growing fast enough to reach to the density in a near future. Thus, instead of using BCNTs, another kind of carbon-based nanomaterials such as graphene can be used as good antenna material in THz and optical frequency range. Graphene is a 2D planar structure with one or two layers of the carbon atoms [53]. Currently, the size of fabricated graphene has increased to a wavelength scale at THz and even millimeter-waves, so the focus of graphene research for the passive devices also has been increasing recently [107]. Graphene shows a higher DC conductivity than metals. However, the utilization of graphene as an antenna material in the microwave frequency range has been doubtful due to its high surface impedance at that frequency range [107]. Nevertheless, graphene at THz and IR band shows plasmonic effect which can be used for sensing and detecting devices. In addition, a 2D structure of graphene provides 2D conductivity that is tunable from the electric or

magnetic bias. This viable material property and fast-growing fabrication technique of graphene encourages its utilization for an antenna material at THz and optical frequency.

Also, optimum metallic antenna topology and its array for TPVs, IR detectors, and IR polarimetries utilizing InGaAsSb p-n junction, presented from Chapter 3 to Chapter 5 could have the next step in the real fabrication for those devices. Before the fabrication process, the modifications of the antenna and the load structure for a more fabrication-friendly design should be followed up on. It is important that the antenna design principle such as the maximum power transfer condition for designing the linear polarized bowtie antenna and the perfect CP condition for designing the cross tapered-bowtie antenna along its boresight should be maintained. In the fabrication procedure, the growth of 30 nm × 30 nm × 30 nm volume of InGaAsSb is quite challenging from current MBE technique, and a good contact between the InGaAsSb and metallic traces with a small scale is also an issue, thus a two dimensional layer of InGaAsSb can be suggested as shown in Fig. 6.1.

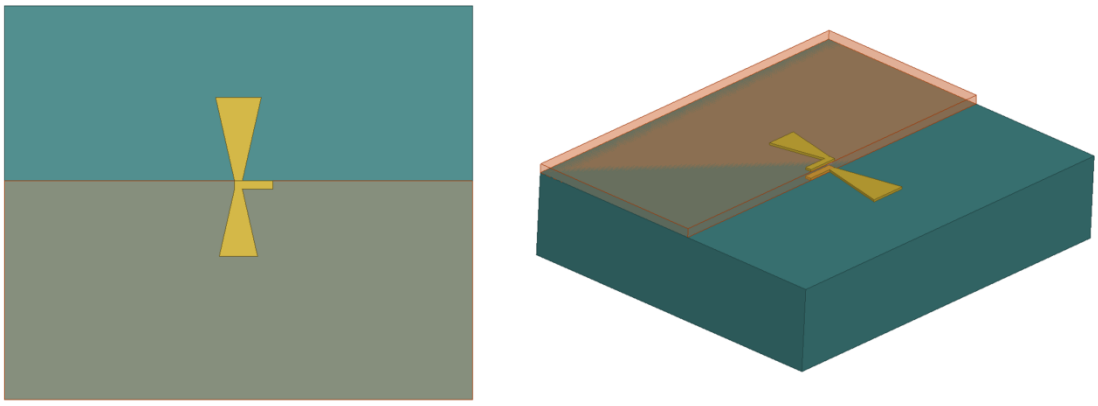

Figure 6.1: Antenna pattern on a substrate and InGaAsSb layer for fabrication.

Instead of maintaining the small size of the InGaAsSb p-n junction, the InGaAsSb can be deposited on a substrate and still can be positioned between the bowtie antenna terminals. Still there is an issue about the contact between the antenna and the InGaAsSb, but printing gold trace on the surface of the InGaAsSb layer could be a possible method. Regarding the antenna design, the antenna optimization method for the maximum power transfer can still be applied to this structure because the field enhancement can be still excited between the terminals of the antenna.

Another future work can be a theoretical and numerical study on the conditions for CP wave generation and the maximum power transfer for IR antennas. The CP wave is generated at the antenna's series resonance and this mode can support the similar current level on each vertical and horizontal bowtie of the cross bowtie antenna in the IR range. However, this mode does not correspond to the parallel resonance mode for the maximum power transfer. Thus, the optimized antenna for the perfect CP along its boresight does not have a high field enhancement at its terminals. This phenomenon also can be seen in a cross dipole antenna operating at optical frequencies [96]. Investigating on a novel method to design an IR CP antenna that also satisfies the maximum power transfer condition would be another interesting future work.

6.3 List of Publications

Journals

S. Choi and K. Sarabandi, “3D Direction Finding using Circular Polarized Cross Dipole Antenna,” *IEEE Transactions Antennas Propagation*, in preparation.

S. Choi and K. Sarabandi, "Bowtie Nanoantenna Integrated with InGaAsSb for Uncooled Infrared Detector with Enhanced Sensitivity," *Applied Optics*, vol. 52, no. 35, pp. 8432 – 8438, Dec. 2013.

K. Sarabandi and S. Choi, "Design Optimization of Bowtie Nanoantenna for High-Efficiency Thermophotovoltaics," *Journal of Applied Physics*, vol. 114, no. 21, pp. 214303, Dec. 2013.

F. M. Ozkeskin, S. Choi, K. Sarabandi, Y. B. Gianchandani, "Batch Fabricated High Power RF Micro-relays with Direct On-PCB Packages," *Journal of Micro-electromechanical Systems*, vol. 12, no. 4, pp. 990 – 1001, Aug. 2012.

F. M. Ozkeskin, S. Choi, K. Sarabandi, Y. B. Gianchandani, "An All-Metal Micro-Relay with Bulk Pt-Rh contact for High Power RF applications," *IEEE Transactions Microwave Theory and Techniques*, vol. 60, no. 6, pp. 1595 – 1604, Jun. 2012.

S. Choi and K. Sarabandi, "Performance assessment of bundled carbon nanotube for antenna applications at terahertz frequencies and higher," *IEEE Transactions Antennas Propagation*, vol. 59, no. 3, pp. 802 – 809, Mar. 2011.

Conference Proceedings

S. Choi and K. Sarabandi, "Efficient Nanoantenna Simulation for IR Energy Harvesting and Detection Devices," invited to *31th URSI General Assembly and Scientific Symposium*, Beijing, China, Aug. 2014.

S. Choi and K. Sarabandi, "IR Polarimetry using Compact Circular Polarized IR Antennas Integrated with InGaAsSb Nano-load," accepted to *2014 IEEE Int. Symp. On Antennas and Propag. And USNC/URSI Nat. Radio Science Meeting*, Memphis, TN, Jul. 2014.

S. Choi and K. Sarabandi, "3-D Direction Finding Using A Single Antenna," accepted to *2014 IEEE Int. Symp. On Antennas and Propag. And USNC/URSI Nat. Radio Science Meeting*, Memphis, TN, Jul. 2014.

S. Choi and K. Sarabandi, "Novel Bowtie Nanoantenna Design for High-Efficiency Thermophotovoltaics," *2013 Antenna Measurement Techniques Association 35th Annual Meeting and Symposium*, Columbus, OH, Oct. 2013.

S. Choi and K. Sarabandi, "High Efficient Bowtie Nanoantenna For Thermophotovoltaic Cells," *2013 IEEE Int. Symp. On Antennas and Propag. And USNC/URSI Nat. Radio Science Meeting*, Orlando, FL, Jul. 2013.

S. Choi and K. Sarabandi, "Sensitive Near-IR Detector Using Plasmonic Bowtie Nanoantenna Integrated with InGaAsSb Nano-load," *2013 IEEE Int. Symp. On Antennas and Propag. And USNC/URSI Nat. Radio Science Meeting*, Orlando, FL, Jul. 2013.

S. Choi and K. Sarabandi, "Design Optimization of Bowtie Nanoantenna for High-Efficiency Thermophotovoltaics," *2013 IEEE USNC/URSI Nat. Radio Science Meeting*, Boulder, CO, Jan. 2013.

S. Choi and K. Sarabandi, "Design Optimization of Nanobowtie Antenna for High-Efficiency Low Bandgap Photovoltaic Cells," *2012 IEEE Int. Symp. On Antennas and Propag. And USNC/URSI Nat. Radio Science Meeting*, Chicago, IL, Jul. 2012.

K. Sarabandi and S. Choi, "Radiation Efficiency Assessment of Bundled Carbon Nanotube," *2011 URSI General Assembly and Scientific Symposium of International Union of Radio Science*, Istanbul, Turkey, Aug. 2011.

S. Choi and K. Sarabandi, "Performance Characterization of Carbon Nanotube Coplanar Waveguide Line," *2011 IEEE Int. Symp. On Antennas and Propag. And USNC/URSI Nat. Radio Science Meeting*, Spokane, WA, Jul. 2011.

F. M. Ozkeskin, S. Choi, K. Sarabandi, Y. B. Gianchandani, "Metal foil RF micro-relay with integrated heat sink for high power applications," *2011 IEEE 24th International Conference on Micro Electro Mechanical Systems (MEMS)*, Cancun, Mexico, pp.776 – 779, Jan. 2011.

S. Choi and K. Sarabandi, "Design of Efficient Terahertz Antenna: Carbon Nanotube vesus Gold," *2010 IEEE Int. Symp. On Antennas and Propag. And USNC/URSI Nat. Radio Science Meeting*, Toronto, ON, Canada, Jul. 2010.

BIBLIOGRAPHY

[1] I. F. Akyildiz, J. M. Jornet, and C. Han, "Terahertz band: Next frontier for wireless communications," *Physical Communication,* vol. 12, pp. 16-32, 2014.
[2] P. H. Siegel, "Terahertz technology," *IEEE Transactions on Microwave Theory and Techniques,* vol. 50, pp. 910-928, Mar 2002.
[3] H. J. Song and T. Nagatsuma, "Present and Future of Terahertz Communications," *IEEE Transactions on Terahertz Science and Technology,* vol. 1, pp. 256-263, Sep 2011.
[4] R. Al Hadi, H. Sherry, J. Grzyb, Y. Zhao, W. Forster, H. M. Keller, *et al.*, "A 1 k-Pixel Video Camera for 0.7-1.1 Terahertz Imaging Applications in 65-nm CMOS," *IEEE Journal of Solid-State Circuits,* vol. 47, pp. 2999-3012, Dec 2012.
[5] M. Walther, D. Cooke, C. Sherstan, M. Hajar, M. Freeman, and F. Hegmann, "Terahertz conductivity of thin gold films at the metal-insulator percolation transition," *Physical Review B,* vol. 76, p. 125408, 2007.
[6] G. Hanson, "Radiation efficiency of nano-radius dipole antennas in the microwave and far-infrared regimes," *Antennas and Propagation Magazine, IEEE,* vol. 50, pp. 66-77, 2008.
[7] N. Laman and D. Grischkowsky, "Terahertz conductivity of thin metal films," *Applied Physics Letters,* vol. 93, p. 051105, 2008.
[8] T. Kuan, C. Inoki, G. Oehrlein, K. Rose, Y. P. Zhao, G. C. Wang, *et al.*, "Fabrication and Performance limits of sub-0.1 μm Cu Interconnects," in *MRS Proceedings*, 2000.
[9] P. L. McEuen, M. S. Fuhrer, and H. K. Park, "Single-walled carbon nanotube electronics," *IEEE Transactions on Nanotechnology,* vol. 1, pp. 78-85, Mar 2002.
[10] S. D. Li, Z. Yu, C. Rutherglen, and P. J. Burke, "Electrical properties of 0.4 cm long single-walled carbon nanotubes," *Nano Letters,* vol. 4, pp. 2003-2007, Oct 2004.
[11] R. Saito, G. Dresselhaus, and M. S. Dresselhaus, *Physical properties of carbon nanotubes* vol. 4: World Scientific, 1998.
[12] C. Rutherglen and P. Burke, "Nanoelectromagnetics: Circuit and Electromagnetic Properties of Carbon Nanotubes," *Small,* vol. 5, pp. 884-906, Apr 2009.
[13] B. Q. Wei, R. Vajtai, and P. M. Ajayan, "Reliability and current carrying capacity of carbon nanotubes," *Applied Physics Letters,* vol. 79, pp. 1172-1174, Aug 2001.
[14] L. Novotny and N. van Hulst, "Antennas for light," *Nature Photonics,* vol. 5, pp. 83-90, Feb 2011.
[15] L. Novotny and B. Hecht, *Principles of nano-optics*. Cambridge ; New York: Cambridge University Press, 2006.
[16] W. L. Barnes, A. Dereux, and T. W. Ebbesen, "Surface plasmon subwavelength optics," *Nature,* vol. 424, pp. 824-830, 2003.
[17] L. Novotny and B. Hecht, *Principles of nano-optics*, 2nd ed. Cambridge: Cambridge University Press, 2012.
[18] R. Bakhtiar, "Surface Plasmon Resonance Spectroscopy: A Versatile Technique in a Biochemist's Toolbox," *Journal of Chemical Education,* vol. 90, pp. 203-209, Feb 2013.
[19] J. Kong, *Electromagnetic Wave Theory*: EMW publishing, 2008.

[20] N. Felidj, J. Aubard, G. Levi, J. R. Krenn, A. Hohenau, G. Schider, *et al.*, "Optimized surface-enhanced Raman scattering on gold nanoparticle arrays," *Applied Physics Letters,* vol. 82, pp. 3095-3097, May 2003.

[21] W. Rechberger, A. Hohenau, A. Leitner, J. R. Krenn, B. Lamprecht, and F. R. Aussenegg, "Optical properties of two interacting gold nanoparticles," *Optics Communications,* vol. 220, pp. 137-141, May 2003.

[22] S. Gresillon, L. Aigouy, A. C. Boccara, J. C. Rivoal, X. Quelin, C. Desmarest, *et al.*, "Experimental observation of localized optical excitations in random metal-dielectric films," *Physical Review Letters,* vol. 82, pp. 4520-4523, May 1999.

[23] F. P. G. de Arquer, V. Volski, N. Verellen, G. A. E. Vandenbosch, and V. V. Moshchalkov, "Engineering the Input Impedance of Optical Nano Dipole Antennas: Materials, Geometry and Excitation Effect," *IEEE Transactions on Antennas and Propagation,* vol. 59, pp. 3144-3153, Sep 2011.

[24] K. D. Ko, A. Kumar, K. H. Fung, R. Ambekar, G. L. Liu, N. X. Fang, *et al.*, "Nonlinear Optical Response from Arrays of Au Bowtie Nanoantennas," *Nano Letters,* vol. 11, pp. 61-65, Jan 2011.

[25] E. Briones, J. Briones, A. Cuadrado, S. M. Murtry, M. Hehn, F. Montaigne, *et al.*, "Computational Analysis of a Spiral Thermoelectric Nanoantenna for Solar Energy Harvesting Applications," *arXiv preprint arXiv:1401.4971,* 2014.

[26] D. Dregely, R. Taubert, J. Dorfmuller, R. Vogelgesang, K. Kern, and H. Giessen, "3D optical Yagi-Uda nanoantenna array," *Nature Communications,* vol. 2, Apr 2011.

[27] P. Muhlschlegel, H. J. Eisler, O. J. F. Martin, B. Hecht, and D. W. Pohl, "Resonant optical antennas," *Science,* vol. 308, pp. 1607-1609, Jun 2005.

[28] P. Biagioni, J. S. Huang, L. Duo, M. Finazzi, and B. Hecht, "Cross Resonant Optical Antenna," *Physical Review Letters,* vol. 102, Jun 2009.

[29] A. Alu and N. Engheta, "Tuning the scattering response of optical nanoantennas with nanocircuit loads," *Nature Photonics,* vol. 2, pp. 307-310, May 2008.

[30] T. J. Seok, A. Jamshidi, M. Kim, S. Dhuey, A. Lakhani, H. Choo, *et al.*, "Radiation Engineering of Optical Antennas for Maximum Field Enhancement," *Nano Letters,* vol. 11, pp. 2606-2610, Jul 2011.

[31] A. Alu and N. Engheta, "Input impedance, nanocircuit loading, and radiation tuning of optical nanoantennas," *Physical Review Letters,* vol. 101, Jul 2008.

[32] D. P. Fromm, A. Sundaramurthy, P. J. Schuck, G. Kino, and W. E. Moerner, "Gap-dependent optical coupling of single "Bowtie" nanoantennas resonant in the visible," *Nano Letters,* vol. 4, pp. 957-961, May 2004.

[33] M. W. Knight, H. Sobhani, P. Nordlander, and N. J. Halas, "Photodetection with Active Optical Antennas," *Science,* vol. 332, pp. 702-704, May 2011.

[34] L. Tang, S. E. Kocabas, S. Latif, A. K. Okyay, D. S. Ly-Gagnon, K. C. Saraswat, *et al.*, "Nanometre-scale germanium photodetector enhanced by a near-infrared dipole antenna," *Nature Photonics,* vol. 2, pp. 226-229, Apr 2008.

[35] K. A. Willets and R. P. Van Duyne, "Localized surface plasmon resonance spectroscopy and sensing," *Annu. Rev. Phys. Chem.*, vol. 58, pp. 267-297, 2007.

[36] P. Bharadwaj, B. Deutsch, and L. Novotny, "Optical Antennas," *Advances in Optics and Photonics,* vol. 1, pp. 438-483, Nov 2009.

[37] M. L. Brongersma, "Plasmonics - Engineering optical nanoantennas," *Nature Photonics,* vol. 2, pp. 270-272, May 2008.
[38] "Beyond the diffraction limit," *Nature Photonics,* vol. 3, pp. 361-361, Jul 2009.
[39] P. J. Schuck, D. P. Fromm, A. Sundaramurthy, G. S. Kino, and W. E. Moerner, "Improving the mismatch between light and nanoscale objects with gold bowtie nanoantennas," *Physical Review Letters,* vol. 94, Jan 2005.
[40] V. R. Manfrinato, L. H. Zhang, D. Su, H. G. Duan, R. G. Hobbs, E. A. Stach, *et al.*, "Resolution Limits of Electron-Beam Lithography toward the Atomic Scale," *Nano Letters,* vol. 13, pp. 1555-1558, Apr 2013.
[41] P. M. Krenz, B. Tiwari, G. P. Szakmany, A. O. Orlov, F. J. Gonzalez, G. D. Boreman, *et al.*, "Response Increase of IR Antenna-Coupled Thermocouple Using Impedance Matching," *IEEE Journal of Quantum Electronics,* vol. 48, pp. 659-664, May 2012.
[42] H. A. Atwater and A. Polman, "Plasmonics for improved photovoltaic devices (vol 9, pg 205, 2010)," *Nature Materials,* vol. 9, pp. 865-865, Oct 2010.
[43] J. J. Greffet, M. Laroche, and F. Marquier, "Impedance of a Nanoantenna and a Single Quantum Emitter," *Physical Review Letters,* vol. 105, Sep 2010.
[44] A. Alu and N. Engheta, "Theory, Modeling and Features of Optical Nanoantennas," *IEEE Transactions on Antennas and Propagation,* vol. 61, pp. 1508-1517, Apr 2013.
[45] C. A. Wang, "Antimony-based III-v thermophotovoltaic materials and devices," *Thermophotovoltaic Generation of Electricity,* vol. 738, pp. 255-266, 2004.
[46] D. Long, "Photovoltaic and photoconductive infrared detectors," in *Optical and infrared detectors*, ed: Springer, 1980, pp. 101-147.
[47] S. Salahuddin, M. Lundstrom, and S. Datta, "Transport effects on signal propagation in quantum wires," *IEEE Transactions on Electron Devices,* vol. 52, pp. 1734-1742, Aug 2005.
[48] J. J. Plombon, K. P. O'Brien, F. Gstrein, V. M. Dubin, and Y. Jiao, "High-frequency electrical properties of individual and bundled carbon nanotubes," *Applied Physics Letters,* vol. 90, Feb 2007.
[49] C. Rutherglen, D. Jain, and P. Burke, "rf resistance and inductance of massively parallel single walled carbon nanotubes: Direct, broadband measurements and near perfect 50 Omega impedance matching," *Applied Physics Letters,* vol. 93, Aug 2008.
[50] G. W. Hanson, "Fundamental transmitting properties of carbon nanotube antennas," *IEEE Transactions on Antennas and Propagation,* vol. 53, pp. 3426-3435, Nov 2005.
[51] P. J. Burke, "An RF circuit model for carbon nanotubes," *IEEE Transactions on Nanotechnology,* vol. 3, pp. 331-331, Jun 2004.
[52] J. C. Charlier, X. Blase, and S. Roche, "Electronic and transport properties of nanotubes," *Reviews of Modern Physics,* vol. 79, pp. 677-732, Apr-Jun 2007.
[53] A. K. Geim and K. S. Novoselov, "The rise of graphene," *Nature Materials,* vol. 6, pp. 183-191, Mar 2007.
[54] E. L. Wolf, "Nanophysics and Nanotechnology Applied to Sensors, Part 1," *IEEE Instrumentation & Measurement Magazine,* vol. 13, pp. 26-32, Jun 2010.

[55] S. W. Hong, T. Banks, and J. A. Rogers, "Improved Density in Aligned Arrays of Single-Walled Carbon Nanotubes by Sequential Chemical Vapor Deposition on Quartz," *Advanced Materials,* vol. 22, pp. Cp30-Cp30, Dec 1 2010.

[56] W. W. Zhou, C. Rutherglen, and P. J. Burke, "Wafer Scale Synthesis of Dense Aligned Arrays of Single-Walled Carbon Nanotubes," *Nano Research,* vol. 1, pp. 158-165, Aug 2008.

[57] T. B. Senior and J. L. Volakis, *Approximate boundary conditions in electromagnetics*: Iet, 1995.

[58] T. B. A. Senior, K. Sarabandi, and F. T. Ulaby, "Measuring and Modeling the Backscattering Cross-Section of a Leaf," *Radio Science,* vol. 22, pp. 1109-1116, Nov 1987.

[59] M. Moallem, J. East, and K. Sarabandi, "Optimally Designed Membrane-Supported Grounded CPW Structure for Submillimeter-Wave Applications," *2009 IEEE Antennas and Propagation Society International Symposium and Usnc/Ursi National Radio Science Meeting, Vols 1-6*, pp. 3267-3270, 2009.

[60] D. Liao, "Physics-based near-earth radiowave propagation modeling and simulation," Ph. D Dissertation, University of Michigan, 2009.

[61] M. W. Dashiell, J. E. Beausang, H. Ehsani, G. J. Nichols, D. M. Depoy, L. R. Danielson, *et al.,* "Quaternary InGaAsSb thermophotovoltaic diodes," *IEEE Transactions on Electron Devices,* vol. 53, pp. 2879-2891, Dec 2006.

[62] W. Chan, P. Bermel, R. Pilawa-Podgurski, C. Marton, K. Jensen, M. Soljacic, *et al.*, "A high-efficiency millimeter-scale thermophotovoltaic generator," in *TPV-9 World Conference at the 25th European Photovoltiac Solar Energy Conference and Exhibition*, 2010.

[63] M. N. Abedin, T. F. Refaat, R. P. Joshi, O. V. Sulima, M. Mauk, and U. N. Singh, "Characterization and analysis of InGaAsSb detectors," *Infrared Technololgy and Applications Xxix,* vol. 5074, pp. 332-342, 2003.

[64] R. T. Kristensen, J. F. Beausang, and D. M. DePoy, "Frequency selective surfaces as near-infrared electromagnetic filters for thermophotovoltaic spectral control," *Journal of Applied Physics,* vol. 95, pp. 4845-4851, 2004.

[65] P. Nagpal, S. E. Han, A. Stein, and D. J. Norris, "Efficient low-temperature thermophotovoltaic emitters from metallic photonic crystals," *Nano Letters,* vol. 8, pp. 3238-3243, 2008.

[66] Y. X. Yeng, M. Ghebrebrhan, P. Bermel, W. R. Chan, J. D. Joannopoulos, M. Soljacic, *et al.*, "Enabling high-temperature nanophotonics for energy applications," *Proceedings of the National Academy of Sciences of the United States of America,* vol. 109, pp. 2280-2285, Feb 14 2012.

[67] W. Chan, R. Huang, C. Wang, J. Kassakian, J. Joannopoulos, and I. Celanovic, "Modeling low-bandgap thermophotovoltaic diodes for high-efficiency portable power generators," *Solar Energy Materials and Solar Cells,* vol. 94, pp. 509-514, Mar 2010.

[68] C. J. Vineis, "Characterization of OMVPE-grown GaSb-based epilayers using in situ reflectance and ex situ TEM," Massachusetts Institute of Technology, 2001.

[69] M. Schnell, P. Alonso-Gonzalez, L. Arzubiaga, F. Casanova, L. E. Hueso, A. Chuvilin, *et al.*, "Nanofocusing of mid-infrared energy with tapered transmission lines," *Nature Photonics,* vol. 5, pp. 283-287, May 2011.

[70] D. W. Peters, C. M. Reinke, P. S. Davids, J. F. Klem, D. Leonhardt, J. R. Wendt, *et al.*, "Nanoantenna-Enabled Midwave Infrared Focal Plane Arrays," *Infrared Technology and Applications Xxxviii, Pts 1 and 2*, vol. 8353, 2012.
[71] J. A. Schuller, E. S. Barnard, W. S. Cai, Y. C. Jun, J. S. White, and M. L. Brongersma, "Plasmonics for extreme light concentration and manipulation," *Nature Materials*, vol. 9, Apr 2010.
[72] J. A. Bean, B. Tiwari, G. H. Bernstein, P. Fay, and W. Porod, "Thermal infrared detection using dipole antenna-coupled metal-oxide-metal diodes," *Journal of Vacuum Science & Technology B*, vol. 27, pp. 11-14, Feb 2009.
[73] J. A. Bean, A. Weeks, and G. D. Boreman, "Performance Optimization of Antenna-Coupled Al/AlOx/Pt Tunnel Diode Infrared Detectors," *IEEE Journal of Quantum Electronics*, vol. 47, pp. 126-135, Jan 2011.
[74] J. Alda, J. M. Rico-Garcia, J. M. Lopez-Alonso, and G. Boreman, "Optical antennas for nano-photonic applications," *Nanotechnology*, vol. 16, pp. S230-S234, May 2005.
[75] K. Sarabandi, "Derivation of phase statistics from the Mueller matrix," *Radio Science*, vol. 27, pp. 553-560, 1992.
[76] J. Oh and K. Sarabandi, "A Topology-Based Miniaturization of Circularly Polarized Patch Antennas," *IEEE Transactions on Antennas and Propagation*, vol. 61, pp. 1422-1426, Mar 2013.
[77] S. X. Ta, H. Choo, I. Park, and R. W. Ziolkowski, "Multi-Band, Wide-Beam, Circularly Polarized, Crossed, Asymmetrically Barbed Dipole Antennas for GPS Applications," *IEEE Transactions on Antennas and Propagation*, vol. 61, pp. 5771-5775, Nov 2013.
[78] J. W. Baik, T. H. Lee, S. Pyo, S. M. Han, J. Jeong, and Y. S. Kim, "Broadband Circularly Polarized Crossed Dipole With Parasitic Loop Resonators and Its Arrays," *IEEE Transactions on Antennas and Propagation*, vol. 59, pp. 80-88, Jan 2011.
[79] S. W. Qu, C. H. Chan, and Q. A. Xue, "Wideband and High-Gain Composite Cavity-Backed Crossed Triangular Bowtie Dipoles for Circularly Polarized Radiation," *IEEE Transactions on Antennas and Propagation*, vol. 58, pp. 3157-3164, Oct 2010.
[80] W. S. Yoon, S. M. Han, J. W. Baik, S. Pyo, J. Lee, and Y. S. Kim, "Crossed dipole antenna with switchable circular polarisation sense," *Electronics Letters*, vol. 45, pp. 717-718, Jul 2009.
[81] H. De-xiu, L. Dong-hai, and C. Hao, "A new approach of high resolution direction finding using single channel receiver," in *Image Analysis and Signal Processing (IASP), 2010 International Conference on*, 2010, pp. 513-517.
[82] D. N. Aloi and M. S. Sharawi, "Comparative analysis of single-channel direction finding algorithms for automotive applications at 2400 MHz in a complex reflecting environment," *Physical Communication*, vol. 3, pp. 19-27, 2010.
[83] R. O. Schmidt, "Multiple Emitter Location and Signal Parameter-Estimation," *IEEE Transactions on Antennas and Propagation*, vol. 34, pp. 276-280, Mar 1986.
[84] R. Roy and T. Kailath, "Esprit - Estimation of Signal Parameters Via Rotational Invariance Techniques," *IEEE Transactions on Acoustics Speech and Signal Processing*, vol. 37, pp. 984-995, Jul 1989.

[85] R. Hammerle, "Factors limiting the accuracy of Doppler and Adcock direction finding systems," in *Passive Direction Finding, IEE Colloquium on*, 1989, pp. 311-313.
[86] R. products, *A Comparison of the Watson Watt and Pseudo-Doppler DF Techniques*, 1999.
[87] J. S. Tyo, D. L. Goldstein, D. B. Chenault, and J. A. Shaw, "Review of passive imaging polarimetry for remote sensing applications," *Applied Optics*, vol. 45, pp. 5453-5469, Aug 1 2006.
[88] V. Gruev, J. Van der Spiegel, and N. Engheta, "Dual-tier thin film polymer polarization imaging sensor," *Optics express*, vol. 18, pp. 19292-19303, Aug 30 2010.
[89] V. Gruev, R. Perkins, and T. York, "CCD polarization imaging sensor with aluminum nanowire optical filters," *Optics express*, vol. 18, pp. 19087-19094, 2010.
[90] J. S. Tyo, B. M. Ratliff, J. K. Boger, W. T. Black, D. L. Bowers, and M. P. Fetrow, "The effects of thermal equilibrium and contrast in LWIR polarimetric images," *Optics express*, vol. 15, pp. 15161-15167, Nov 2007.
[91] K. Bachman, J. Peltzer, P. Flammer, T. Furtak, R. Collins, and R. Hollingsworth, "Spiral plasmonic nanoantennas as circular polarization transmission filters," *Optics express*, vol. 20, pp. 1308-1319, 2012.
[92] B. Paivanranta, N. Passilly, J. Pietarinen, P. Laakkonen, M. Kuittinen, and J. Tervo, "Low-cost fabrication of form-birefringent quarter-wave plates," *Optics express*, vol. 16, pp. 16334-16342, Oct 2008.
[93] Y. Pang and R. Gordon, "Metal nano-grid reflective wave plate," *Optics express*, vol. 17, pp. 2871-2879, Feb 2009.
[94] S. Y. Hsu, K. L. Lee, E. H. Lin, M. C. Lee, and P. K. Wei, "Giant birefringence induced by plasmonic nanoslit arrays," *Applied Physics Letters*, vol. 95, Jul 2009.
[95] M. R. Shcherbakov, M. I. Dobynde, T. V. Dolgova, D. P. Tsai, and A. A. Fedyanin, "Full Poincare sphere coverage with plasmonic nanoslit metamaterials at Fano resonance," *Physical Review B*, vol. 82, Nov 2010.
[96] P. Biagioni, M. Savoini, J. S. Huang, L. Duo, M. Finazzi, and B. Hecht, "Near-field polarization shaping by a near-resonant plasmonic cross antenna," *Physical Review B*, vol. 80, Oct 2009.
[97] B. Abasahl, S. Dutta-Gupta, C. Santschi, and O. J. F. Martin, "Coupling Strength Can Control the Polarization Twist of a Plasmonic Antenna," *Nano Letters*, vol. 13, pp. 4575-4579, Sep 2013.
[98] N. F. Yu, F. Aieta, P. Genevet, M. A. Kats, Z. Gaburro, and F. Capasso, "A Broadband, Background-Free Quarter-Wave Plate Based on Plasmonic Metasurfaces," *Nano Letters*, vol. 12, pp. 6328-6333, Dec 2012.
[99] J. J. Peltzer, K. A. Bachman, J. W. Rose, P. D. Flammer, T. E. Furtak, R. T. Collins, *et al.*, "Plasmonic micropolarizers for full Stokes vector imaging," *Polarization: Measurement, Analysis, and Remote Sensing X*, vol. 8364, 2012.
[100] A. Drezet, C. Genet, and T. W. Ebbesen, "Miniature plasmonic wave plates," *Physical Review Letters*, vol. 101, p. 043902, 2008.
[101] Y. Gorodetski, E. Lombard, A. Drezet, C. Genet, and T. W. Ebbesen, "A perfect plasmonic quarter-wave plate," *Applied Physics Letters*, vol. 101, Nov 2012.

[102] A. Roberts and L. Lin, "Plasmonic quarter-wave plate," *Optics Letters,* vol. 37, pp. 1820-1822, Jun 2012.
[103] H. Zhao, Y. Q. Yang, Q. Li, and M. Qiu, "Sub-wavelength quarter-wave plate based on plasmonic patch antennas," *Applied Physics Letters,* vol. 103, Dec 2013.
[104] B. A. Yang, W. M. Ye, X. D. Yuan, Z. H. Zhu, and C. Zeng, "Design of ultrathin plasmonic quarter-wave plate based on period coupling," *Optics Letters,* vol. 38, pp. 679-681, Mar 2013.
[105] F. J. Gonzalez and G. D. Boreman, "Comparison of dipole, bowtie, spiral and log-periodic IR antennas," *Infrared Physics & Technology,* vol. 46, pp. 418-428, Jun 2005.
[106] F. J. Gonzalez, B. Ilic, J. Alda, and G. D. Boreman, "Antenna-coupled infrared detectors for imaging applications," *IEEE Journal of Selected Topics in Quantum Electronics,* vol. 11, pp. 117-120, Feb 2005.
[107] J. Perruisseau-Carrier, "Graphene for Antenna Applications: Opportunities and Challenges from Microwaves to THz," *2012 Loughborough Antennas & Propagation Conference (Lapc),* 2012.